Boston University

OpenBU **http://open.bu.edu**

Theses & Dissertations Boston University Theses & Dissertations

2015

Nanomechanical measurements of fluctuations in biological, turbulent, and confined flows

https://hdl.handle.net/2144/15719

Boston University

BOSTON UNIVERSITY

COLLEGE OF ENGINEERING

Dissertation

NANOMECHANICAL MEASUREMENTS OF FLUCTUATIONS IN BIOLOGICAL, TURBULENT, AND CONFINED FLOWS

by

CHARLES A. LISSANDRELLO

B.S., Boston University, 2009
M.S., Boston University, 2012

Submitted in partial fulfillment of the
requirements for the degree of
Doctor of Philosophy

2015

© 2015 by
Charles A. Lissandrello
All rights reserved

Approved by

First Reader

Kamil L. Ekinci, Ph.D.
Professor of Mechanical Engineering

Second Reader

Victor Yakhot, Ph.D.
Professor of Mechanical Engineering

Third Reader

R. Glynn Holt, Ph.D.
Associate Professor of Mechanical Engineering

Fourth Reader

Chuanhua Duan, Ph.D.
Assistant Professor of Mechanical Engineering

Acknowledgments

I would first like to thank Prof. Kamil Ekinci for giving me the opportunity to work with him over the years. I have had the privilege of being his academic advisee and his student in the classroom and in the laboratory. He has patiently taught me how to approach scientific problems, from the broadest questions to the smallest experimental details. His mentorship has helped to shape my academic journey and his support has been critical to my success thus far. His approach to science is imaginative, thoughtful, and precise and I am grateful to have him as a mentor. I would also like to acknowledge Prof. Victor Yakhot for being a patient and encouraging mentor. He has played a significant role in my development as a researcher and his immense knowledge has been an inspiration to me. I appreciate all of the time he has devoted to our work together.

I would like to thank Prof. Glynn Holt and Prof. Chuanhua Duan for being a part of my dissertation committee. I am also grateful to Prof. Taejoon Kouh who was a member of my prospectus committee, and Prof. Paul Barbone and Prof. Allan Pierce who served on my qualifying exam committee. I am also grateful to have had the opportunity to work with excellent collaborators, including Prof. Ismet Kaya who helped with graphene resonator studies, and Prof. Utkan Demirci and Dr. Fatih Inci who brought their expertise to our bacteria work. I am also thankful for the unbiased and invaluable guidance I received from Prof. Tyrone Porter, Prof. Robin Cleveland, and Prof. Mario Cabodi when I was applying to graduate school.

I am also grateful for the work of the staff in the Mechanical Engineering office, particularly Megan, Magda, Saana, Jasmine, Natasha, Emily, and Seth. I would also like to thank Dr. Helen Fawcett and Paul Mak in the Photonics Center and the clean room, Joe, Dave, and Bob in the machine shop, and the custodial staff who work hard day and night to keep the buildings running.

I am lucky to have shared my time in the lab with some of the smartest, kindest, and hardest-working people I know (they also possess excellent fine motor skills). First, I would like to acknowledge the past lab members who I learned so much from. Sometimes this knowledge came indirectly, through their papers and theses, and other times in person. Utku, I think I learned more in my one day visit to NIST than I could have figured out on my own in months. When I was an undergraduate in the lab Onur, Devrez, and Utku patiently answered my questions and encouraged me to pursue graduate studies. Second, I would like to acknowledge the lab members who I have had the privilege of sharing the lab with. Suraj, Ozgur, Vural, Le, Seth, and Olivia. You made the lab a fun environment to be in and were always available for intellectual, technical, philosophical, and sometimes personal discussions. I am grateful that we were able to extend our professional relationships into friendships outside of the lab.

I couldn't have made it through the last 5 and 1/2 years without good friends nearby. Matt and Casey, you two have made my time here much more enjoyable by always lending an ear during hard times and by always finding a way to see things in a positive, and usually sarcastic, light. Lauren, Peter, Andy, Allen, Alex, J.D., Joe, Vural, and Ozgur, your friendships have meant a lot to me and I will always have good memories of our time spent together at BU.

Most importantly, I'd like to thank my family. Megan, your unwavering support and your encouragement have helped me through so many tough times. You are my best friend and I am lucky to have you in my life. To my sisters, Rachel and Annie, I'm so grateful that you are also my friends and I am lucky to have had you in Boston over the years. To my parents, your strength is an inspiration to me every day and you've helped me more than you can know. Thank you for making everything possible.

NANOMECHANICAL MEASUREMENTS OF FLUCTUATIONS IN BIOLOGICAL, TURBULENT, AND CONFINED FLOWS

CHARLES A. LISSANDRELLO

Boston University, College of Engineering, 2015

Major Professor: Kamil L. Ekinci, Ph.D.,
Professor of Mechanical Engineering

ABSTRACT

The microcantilever has become a ubiquitous tool for surface science, chemical sensing, biosensing, imaging, and energy harvesting, among many others. It is a device of relatively simple geometry with a static and dynamic response that is well understood. Further, because of it's small size, it is extremely sensitive to small external perturbations. These characteristics make the microcantilever an ideal candidate for a multitude of sensing applications. In this thesis dissertation we use the microcantilever to conduct numerous physical measurements and to study fundamental phenomena in the areas of fluid dynamics, turbulence, and biology. In each area we use the cantilever as a sensitive transducer in order to probe fluctuating forces.

In micro and nanometer scale flows the characteristic length scale of the flow approaches and is even exceeded by the fluid mean free path. This limit is beyond the applicability of the Navier-Stokes equations, requiring a rigorous treatment using kinetic theory. In our first study, we conduct a series of experiments in which we use a microcantilever to measure gas dissipation in a nanoscopically confined system.

Here, the distance between the gas molecules is of the same order as the separation between the cantilever and the walls of its container. As the cantilever is brought towards the wall, the flow becomes confined in the gap between the cantilever and the wall, affecting the resonant frequency and dissipation of the cantilever. By carefully tuning the separation distance, the gas pressure, and the cantilever oscillation frequency, we study the flow over a broad range of dimensionless parameters. Using these measurements, we provide an in-depth characterization of confinement effects in oscillating nanoflows. In addition, we propose a scaling function which describes the flow in the entire parameter space and which unifies previous theories based on the slip boundary condition and effective viscosity.

In our next study, we seek to gain a better understanding of the transition to turbulence in a channel flow. We use a cantilever embedded in the channel wall to perform two sets of experiments: first, we study transition to turbulence triggered by the natural imperfections of the channel walls and second, we study transition under artificially added inlet noise. Our results point to two very different paths to turbulence. In the first case, wall effects lead to an extremely intermittent transitional flow and in the second case, broadband fluctuations originating at the inlet lead to less intermittent flow that is more reminiscent of homogeneous turbulence. The two experiments result in random flows in which high-order moments of near-wall fluctuations differ by orders of magnitude. Surprisingly however, the lowest order statistics in both cases appear qualitatively similar and can be described by a proposed noisy Landau equation. The noise, regardless of its origin, regularizes the Landau singularity of the relaxation time and makes transitions driven by different noise sources appear similar. Our results provide evidence of the existence of a finite turbulent relaxation time in transitional flows due to the persistent nature of noise in the system.

In our last study, we turn to biologically-driven fluctuations from bacterial motion. Recent studies suggest that the motion of living bacteria could serve as a good indicator of bacteria species and resistance to antibiotics. To gain a better understanding of these fluctuations, we measure the nanomechanical motion of bacteria adhered to a chemically functionalized silicon microcantilever. A non-specific binding agent is used to attach *E. coli* to the surface of the device. The motion of the bacteria couples efficiently to the cantilever well below its resonance frequency, causing a measurable increase in its mechanical fluctuations. We vary the bacterial concentration over two orders of magnitude and are able to observe a corresponding change in the amplitude of fluctuations. Additionally, we administer antibiotics (Streptomycin) to kill the bacteria and observe a decrease in the fluctuations. A basic physical model is used to explain the observed spectral distribution of the mechanical fluctuations. These results lay the groundwork for understanding the motion of microorganisms adhered to surfaces and for developing micromechanical sensors for rapid bacterial identification and antibiotic resistance testing.

Contents

1 Introduction 1

1.1 Organization 2

1.2 The Microcantilever as a Physical Probe 4

1.2.1 Damped Harmonic Oscillator Model 4

1.2.2 Thermomechanical Fluctuations 7

2 Nanoscale Displacement Measurements 11

2.1 Optical Beam Deflection 11

2.1.1 Knife-Edge Detection 15

2.2 Michelson Interferometry 16

2.2.1 Homodyne Interferometry 16

2.2.2 Heterodyne Interferometry 20

2.3 Optical Shot Noise 23

2.4 Optical Spot Size 26

3 Estimation of Modal Parameters from Resonance Measurements 28

3.1 Background 28

3.2 Thermomechanical Fluctuations 30

3.2.1 Measurements 33

3.3 Gas Damping 33

3.3.1 Gas Damping in the Kinetic Regime 37

3.3.2 Measurements 41

3.4 Results and Discussion 43

4 **Crossover from Hydrodynamics to the Kinetic Regime in Confined Nanoflows** **47**

4.1 Background 48

4.2 Experimental Setup 49

4.3 Results and Discussion 52

4.3.1 Scaling Theory 56

4.3.2 Collapse of Data 59

5 **Nanomechanical Motion of *Escherichia coli* Adhered to a Surface** **61**

5.1 Background and Motivation 62

5.2 Experimental Setup 65

5.2.1 Sample Preparation 67

5.3 Results and Discussion 69

5.3.1 Time-Domain Measurements 69

5.3.2 Frequency-Domain Measurements 72

5.3.3 Physical Model 73

5.4 Conclusions and Outlook 76

6 **Noisy Transition to Turbulence in Microchannels** **78**

6.1 Introduction 78

6.2 Theory 81

6.2.1 Landau's Stability Analysis 81

6.2.2 Landau's Stability Analysis with Noise 86

6.3 Experiment 87

6.3.1 Pressure Drop 91

6.4 Results 93

6.5 Discussion 100

7 **Conclusion** **103**

References **106**

Curriculum Vitae **115**

List of Tables

3.1 Parameters of measured devices 30
3.2 Results of measurements of ρh determined by multiple methods . . . 45

4.1 Parameters of measured devices 51

5.1 Variance of displacement fluctuations 71

6.1 Moments 99
6.2 Noisy Landau Fit Parameters 102

List of Figures

1·1 Transfer function of a damped harmonic oscillator 6

1·2 PSD of the thermomechanical motion of a cantilever 8

1·3 Time trace of the thermomechanical motion of a cantilever 9

2·1 Optical beam deflection 12

2·2 Knife edge optical detection 15

2·3 Schematic of a homodyne interferometer 19

2·4 Schematic of a heterodyne interferometer 22

2·5 Optical shot noise 25

2·6 Measurement of optical spot size 26

3·1 Common geometries of microscale and nanoscale resonators 29

3·2 Thermal spectra and modeshapes of a cantilever 32

3·3 Fluidic dissipation versus pressure for a microscale cantilever 36

3·4 Rectangular plate moving in a gas 38

3·5 Fluidic dissipation versus pressure for three modes of a microscale cantilever 42

3·6 Mode frequencies of a membrane resonator 43

3·7 Fluidic dissipation versus pressure for five modes of a microscale membrane 44

4·1 Silica sphere adhered to a silicon microcantilever 50

4·2 Measured and simulated mechanical modes of the sphere-cantilever device 51
4·3 Dimensionless dissipation obtained from the driven frequency response and thermal oscillations of the device 52
4·4 Dimensionless fluidic dissipation as a function of gap at fixed pressures and as a function of pressure at fixed gaps 53
4·5 Dimensionless fluidic dissipation as a function of gap at fixed pressures for three cantilever modes 55
4·6 Collapse of all experimental data with scaling function 59

5·1 Illustration of a motile *E. coli* bacterium 63
5·2 Locomotion by running and tumbling 64
5·3 Schematic of the experimental setup 66
5·4 Bacteria adhered to a silicon microcantilever 68
5·5 Surface density of bacteria adhered to a silicon surface 69
5·6 Time-domain measurements of the microcantilever fluctuations 70
5·7 PSD of the microcantilever fluctuations 74

6·1 Time evolution of the disturbance amplitude 82
6·2 Time evolution of the disturbance amplitude considering up to fourth-order terms in A with $\alpha > 0$ 83
6·3 Time evolution of the disturbance amplitude considering up to fourth-order terms in A with $\alpha < 0$ 84
6·4 Long-time limit of disturbance amplitude versus Reynolds number . . 85
6·5 Schematic of the experimental setup 88
6·6 White light interferometer image and optical image of microchannel . 89
6·7 Square root of the PSD of the noise in the system 90
6·8 Saturation of the optical read-out 91

6·9 Pressure drop as a function of Reynolds number in the channel 92

6·10 Power spectral density of cantilever displacements for different Reynolds numbers 94

6·11 Power spectral density of cantilever displacements for cases (i) and (ii) 95

6·12 PDFs of cantilever displacements for cases (i) and (ii) 97

6·13 RMS cantilever displacement versus Reynolds number 100

List of Abbreviations

AFM	....	Atomic Force Microscopy
AMR	....	Antimicrobial Resistance
AOM	....	Acousto-Optic Modulator
APTES	....	(3-Aminopropyl)triethoxysilane
BS	....	Beam Splitter
CFU	....	Colony Forming Unit
FEM	....	Finite Element Method
FFT	....	Fast Fourier Transform
LB	....	Lysogeny Broth
LO	....	Local Oscillator
MEMS	....	Micro-Electro-Mechanical Systems
NEMS	....	Nano-Electro-Mechanical Systems
PBS	....	Phosphate Buffered Saline
PBS	....	Polarizing Beam Splitter
PD	....	Photodetector
PDF	....	Probability Density Function
PID	....	Proportional-Integral-Derivative
PSD	....	Power Spectral Density
RBW	....	Resolution Bandwidth
RMS	....	Root Mean Square
SEM	....	Scanning Electron Microscope
SiN	....	Silicon Nitride
SNR	....	Signal-to-Noise Ratio
UHV	....	Ultra-High Vacuum
VCO	....	Voltage Controlled Oscillator

Chapter 1

Introduction

Many physical phenomena appear to be unpredictable or random, yet when studied closely, can reveal important information about the fundamental physics which govern their behavior. Noisy systems are ubiquitous in nature and a careful study of their fluctuations can be conducted if appropriate experimental systems can be devised. It is often difficult, however, to measure these fluctuations since many of these phenomena occur on length and time scales that are beyond reach of traditional measurement systems. Advances in fabrication technology over the last three decades have led to a multitude of developments in the complexity and variety of microelectromechanical systems (MEMS). These new devices have enabled a new paradigm of sensing in the areas of mass detection (Yang et al., 2006), rheology (Ahmed et al., 2001), charge measurements (Cleland and Roukes, 1998), biosensing (Longo and Kasas, 2014), chemical sensing (Lavrik et al., 2004), and temperature sensing (Zhang et al., 2013) among many others (Waggoner and Craighead, 2007). The microcantilever, in particular, has been one of the mainstays for probing minuscule forces. The first mainstream use of the microcantilever as a sensor was in atomic force microscopy (AFM) (Meyer and Amer, 1988). More recently, researchers have developed more complex structures including cantilevers that incorporate fluid microchannels to enable single molecule mass measurements (Burg et al., 2007) and self-sensing piezoresistive cantilevers (Wee et al., 2005). These experiments made use of both the static deflection and the dynamic motion of the cantilever in order to conduct sensitive measurements.

In this thesis work we are interested in exploiting the exquisite sensitivity and relative simplicity of the microcantilever in order to conduct measurements of fundamental physical phenomena. In almost all of the studies presented here, we use commercial silicon cantilevers to probe fluctuating forces that arise in a diverse range of systems. We employ sensitive optical measurement techniques to monitor the fluctuations of the cantilever which correspond to perturbations in the cantilever's environment. We present studies of physical phenomena in the areas of fluid dynamics, turbulence, and biology. Through rigorous experimentation and theoretical analysis we attempt to advance the boundaries of our understanding of fluctuations in confined, turbulent, and biological flows.

1.1 Organization

We begin in Chapter 2 with an overview of the different optical techniques used to measure nanomechanical fluctuations. In the studies presented here we employ a combination of techniques including homodyne and heterodyne Michelson interferometry and optical beam deflection. We describe these techniques and discuss shot noise limited optical detection. In Chapter 3 we present experimental measurements of the driven and thermomechanical motion of microscale cantilever and membrane resonators in a spatially unbounded Newtonian fluid. We discuss how these measurements can be used to determine the modal device parameters, and we compare the results of many measurements. We also discuss the limits of classical hydrodynamics and the transition to the kinetic regime that occurs in a certain parameter space.

In Chapter 4 we study fluctuations in a nanoscopically confined oscillatory flow by introducing an additional length scale to the system, the gap between the resonator and the walls of its container. Here, this length scale approaches and is even exceeded by the fluid mean free path λ. This parameter space is beyond the applicability of the Navier-Stokes equations and we must use kinetic theory to describe the flow. We conduct a series of experiments in which we use a microcantilever to measure the gas dissipation as we vary the gap, the gas pressure, and the oscillation frequency. The cantilever's oscillations drive an oscillatory flow which, when confined in the gap between the cantilever and the wall, affects the frequency and dissipation of the cantilever. We use our results and physical intuition to construct a scaling function which can describe the dissipation in the entire parameter space studied. Our scaling function accurately captures the transition from the hydrodynamic to the kinetic fluid regime and reconciles previous models which depend on modified boundary conditions and effective viscosity.

In Chapter 5 we study fluctuations driven by the activity of motile bacteria. Recent concerns regarding microbial resistance to antibiotics have sounded the alarm over the need for new antibiotics and bacteria diagnostics. Studies have shown that important information, including species identification and bacterial resistance, can be extracted by measuring the motion of bacteria and their response to various stimuli. In this study, we adhere a motile strand of *E. coli* bacteria to the surface of a silicon cantilever. The cantilever is held in a liquid medium and its fluctuations are monitored using the optical beam deflection technique. The collective motion of the bacteria cause a measurable change in the cantilever's fluctuations. We vary the bacterial surface concentration over an order of magnitude and observe corresponding changes in the amplitude of fluctuations. Additionally, we administer antibiotics to kill the bacteria and observe cessation of their motion. We develop a basic physical model to describe the observed spectral content of the fluctuations.

In Chapter 6 we study fluctuations in a channel flow near the transition to turbulence. We embed a microcantilever in the wall of a rectangular channel and once again, we employ optical beam deflection to monitor the cantilever's mechanical fluctuations. We conduct two sets of experiments. In the first set, we study the transition to turbulence triggered by the natural imperfections of the channel walls. In the second set, we insert a flexible wire mesh at the channel inlet to create perturbations in the flow. The resultant turbulent states are quite different yet are qualitatively similar and each can be described by a proposed noisy Landau equation. Our results provide evidence of the existence of a finite turbulent relaxation time in transitional flows due to the persistent nature of noise in the system.

Finally, in Chapter 7 we conclude with some final thoughts on the results of these studies. We also suggest opportunities for future studies in the field.

1.2 The Microcantilever as a Physical Probe

As we will see in the following chapters, the microcantilever, and other micromechanical systems, are versatile tools which can be used for a wide range of studies. Here, we first discuss specific details regarding the dynamics of these microscale systems. Additionally, we consider the thermomechanical fluctuations of a cantilever and provide a brief discussion of the fluctuation dissipation theorem.

1.2.1 Damped Harmonic Oscillator Model

A microcantilever resonator oscillating in one of its resonant modes behaves like a damped harmonic oscillator to a very good approximation. Coupling this oscillatory motion to external physical phenomena allows for very sensitive measurements of the phenomena. In a resonant mechanical system with light damping and sufficient spacing between modes, the displacement functions of each mode $y_j\left(t\right)$ are oscillatory and each mode can be well described using a damped harmonic oscillator model. We consider a lumped model in which the parameters of the system are approximated as scalar values, independent of the position coordinate $\mathbf{r}$, the dissipation is *constant* and *spatially uniform*, and the displacement is measured at a single point (usually the location of maximum displacement). We write the equation of motion for the j^{th} natural mode as

$$m\frac{d^2y\left(t\right)}{dt^2}+\frac{m\omega_0}{Q}\frac{dy\left(t\right)}{dt}+m{\omega_0}^2y\left(t\right)=f\left(t\right) \tag{1.1}$$

where we omit the j notation for brevity. Here, $f\left(t\right)$ is the driving force, m is the effective modal mass, ω_0 is the resonance frequency, and Q is the quality factor of the resonance. The parameters ω_0 and Q (the undamped frequency and the quality factor) of each mode are highly sensitive to environmental perturbations and can be measured readily through experimentation. The dimensionless dissipation term, $1/Q$, represents dissipation from all sources (both intrinsic and extrinsic) in the system.

We expand the driving force and the displacement into their Fourier components as $f\left(t\right)=\sum_k F_k\cos\left(\omega_k t+\phi_k\right)$ and $y\left(t\right)=\sum_k Y_k\cos\left(\omega_k t+\phi_k'\right)$, respectively. We then find the transfer function $G\left(\omega\right)$ of the mechanical system using the equation of motion Eq. (1.1) as

$$G(\omega)=\frac{1}{m\left({\omega_0}^2-\omega^2+i\frac{\omega\omega_0}{Q}\right)}. \tag{1.2}$$

The spectral density of the mechanical fluctuations $S_y\left(\omega\right)$ is related to the transfer function as $S_y\left(\omega\right)=S_F\left(\omega\right)\left|G\left(\omega\right)\right|^2$ where $S_F\left(\omega\right)$ is the spectral density of the force (Ekinci and Roukes, 2005). We see that if we know the transfer function for a system and if we can measure the spectral density of its fluctuations, then we can make a measurement of the forces acting on that system.

For a damped harmonic oscillator, the square of the transfer function is

$$\left|G(\omega)\right|^2=\frac{1}{m^2}\frac{1}{\left({\omega_0}^2-\omega^2\right)^2+\left(\frac{\omega\omega_0}{Q}\right)^2}. \tag{1.3}$$

It is instructive to have a close look at this system because it is used in every study presented here. We plot Eq. (1.3) in Figure 1·1 for a system with parameters $m=1$ kg, $\omega_0=1\ \text{s}^{-1}$, and $Q=100$. We see from the figure and from the equation that in the

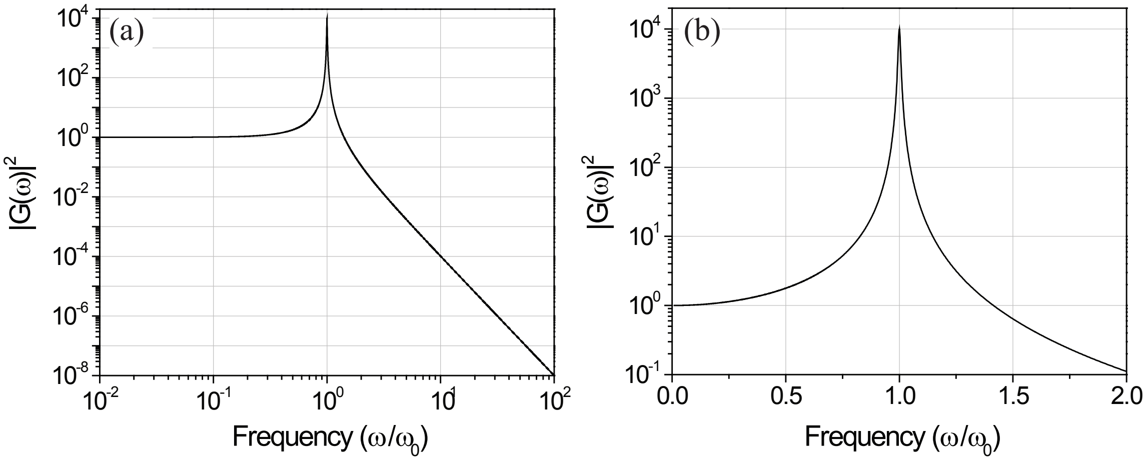

Figure 1·1: Square of the transfer function of a damped harmonic oscillator (Eq. (1.3)) with $m = 1$ kg, $\omega_0 = 1$ s^{-1}, and $Q = 100$ on (a) log-log and (b) log-linear axes.

limit $\omega \rightarrow 0$, the transfer function approaches a constant value $|G(0)|^2 = 1/\kappa^2$ where $\kappa = m{\omega_0}^2$ is the spring constant of the mode. In this sub-resonant frequency range, where the spectral response of the damped harmonic oscillator is nearly flat, we can use our device as a sensitive broadband transducer. We exploit this frequency range in our measurements of bacterial fluctuations, presented in Chapter 5 and in our measurements of transitional turbulence, presented in Chapter 6. In these studies, the signals of interest have a broad spectrum which are relatively low frequency ($\omega \leq \omega_0$) and the sub-resonant device motion is linearly proportional to the force acting on the system. At frequencies near the resonance $\omega \approx \omega_0$, we find $|G(\omega_0)|^2 = Q/\kappa^2$. Here, any force acting on the system is amplified by a factor of Q in the device's response. We exploit this regime in our modal mass measurements (Chapter 3) and in our gas confinement studies (Chapter 4) where we are interested in determining the mode frequency and the quality factor with high sensitivity. At high frequencies, where $\omega > \omega_0$, the transfer function decays as $|G(\omega)|^2 \propto 1/\omega^4$ and the system responds very weakly to perturbations. We do not exploit this region in any of our measurements.

1.2.2 Thermomechanical Fluctuations

In some of the experiments presented in this thesis we measure the spectral density of the deterministically driven system response in order to obtain a measurement of the dissipation and resonance frequency of the system. In other measurements, we are interested in studying the stochastic thermomechanical fluctuations of the device under test. Here, we present an example of the thermomechanical fluctuations of a silicon cantilever and provide a brief review of the theory of Brownian fluctuations in damped harmonic oscillator systems.

The fluctuation-dissipation theorem in its general form was first presented by Callen and Welton in 1951 (Callen and Welton, 1951) as a method to relate the power spectrum of the fluctuations of any system in thermodynamic equilibrium with the energy dissipation of the system. It states that the fluctuations are so well-linked to the dissipation because they are actually a result of the dissipation in the first place. Returning to the equation of motion for a one-dimensional damped harmonic oscillator system, Eq. (1.1), we consider a randomly fluctuating thermal force of the form $f\left(t\right) = \sum_k F_k \cos\left(\omega_k t + \phi_k\right)$, where F_k is a Gaussian random variable with zero average and ϕ_k is a uniformly random phase (Kouh et al., 2014). We further assume that the power spectral density of the thermal force $S_F\left(\omega\right)$ has a white spectrum given as

$$S_F\left(\omega\right) = \frac{4mk_{\mathrm{B}}T\omega_0}{Q}. \tag{1.4}$$

We also expand the displacement into its Fourier components: $y\left(t\right) = \sum_k Y_k \cos\left(\omega_k t + \phi'_k\right)$, where Y_k is also a Gaussian random variable but it is a function of the frequency ω_k. We can write the spectral density of the thermal fluctuations as

$$S_y\left(\omega\right) = \frac{4k_{\mathrm{B}}T\omega_0}{mQ\left[\left({\omega_0}^2 - \omega^2\right)^2 + \left(\frac{\omega\omega_0}{Q}\right)^2\right]}. \tag{1.5}$$

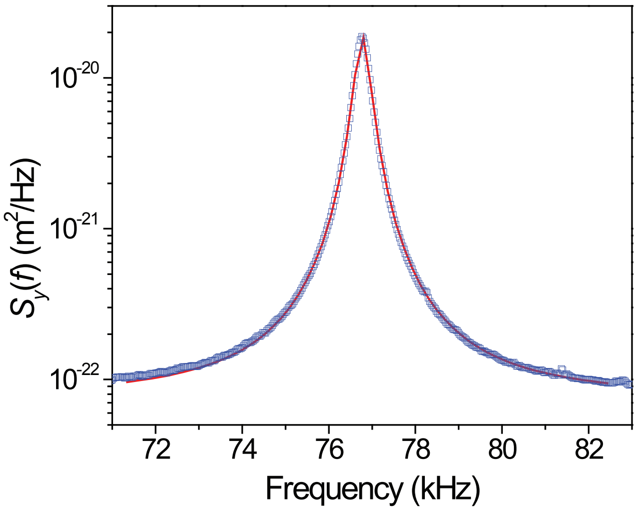

Figure 1·2: Power spectral density of the thermomechanical motion of a silicon cantilever. This particular measurement was conducted at atmospheric pressure and the resonance has a quality factor of 200.

Further, the mean-square displacement at the end of the cantilever due to thermal excitation can be calculated by integrating the spectral density of the fluctuations over all frequencies (Albrecht et al., 1991). We find:

$$\langle y_{\mathrm{th}}^2 \rangle = \frac{1}{2\pi} \int_0^\infty S_y(\omega)\, d\omega, \tag{1.6}$$

and upon substitution,

$$\langle y_{\mathrm{th}}^2 \rangle = \frac{1}{2\pi} \int_0^\infty \frac{4 k_{\mathrm{B}} T \omega_0}{mQ \left[\left(\omega_0^2 - \omega^2\right)^2 + \left(\frac{\omega_0 \omega}{Q}\right)^2 \right]} d\omega. \tag{1.7}$$

We see immediately from this relation that the fluctuations are intimately linked to the dissipation in the system. In a typical experimental measurement, such as the one depicted in Figure 1·2, we can measure the spectral density of the fluctuations directly using a spectrum analyzer. In the case of a damped harmonic oscillator with light damping, we can fit the spectrum to a Lorentzian line shape to find the quality

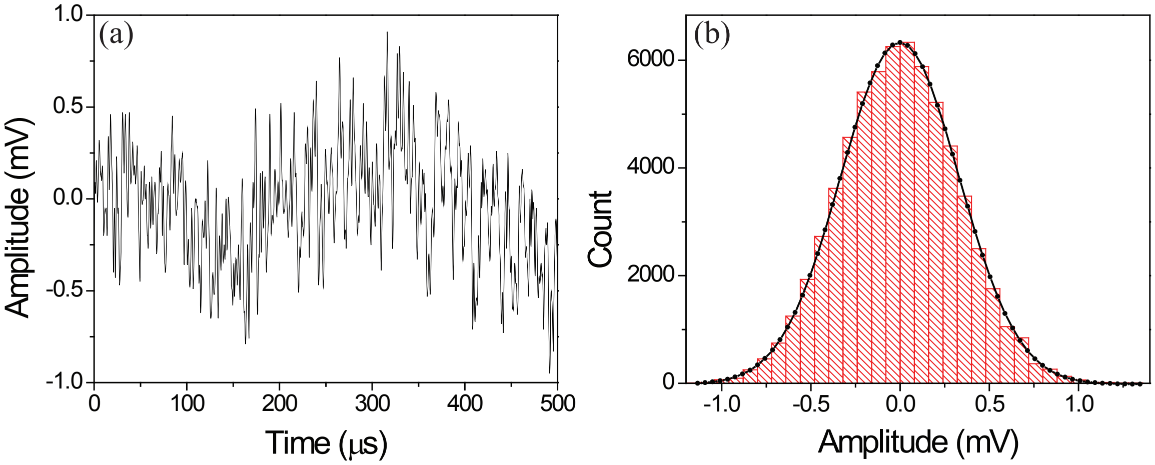

Figure 1·3: (a) A time trace of the signal measured from the fluctuations of a microscale cantilever. (b) A histogram of the time trace data shown in (a). The distribution is fit to a Gaussian line shape. This measurement includes 65,000 data points acquired over 13 milliseconds. The device used is the same as that shown in Figure 1·2

factor of the mechanical mode. Additionally, we can integrate over the spectrum to compute the mean-square displacement $\langle y_{\text{th}}^2 \rangle$ as in Eq. (1.7).

We present a measurement of the thermal fluctuations of a silicon cantilever in Figures 1·2 and 1·3. Here, the cantilever is held at atmospheric pressure and room temperature and it is stochastically actuated by its own thermomechanical energy. We measure its fluctuations using a heterodyne Michelson interferometer which uses the interference between a probe beam striking the resonator, and a reference beam to convert small displacements into detectable signals (as described in detail in Chapter 2). The measured electrical signal (in Volts) is proportional to the displacement of the resonator. The signal can be viewed in the time domain using an oscilloscope or frequency domain measurements can be conducted using a spectrum analyzer. Figure 1·2 is a plot of the power spectral density of the cantilever's fluctuations measured with a fast Fourier transform spectrum analyzer. By fitting this spectrum to a Lorentzian lineshape (red, solid line in the figure) we find $Q \sim 200$. Figure 1·3(a) depicts a 500 μs time trace of the signal from the photodetector measured with an oscilloscope. A histogram of this signal is plotted in Figure 1·3(b). The histogram is fit to a Gaussian with a coefficient of determination of $R^2 = 0.999$. This distribution is exactly as we would expect from our discussion above.

Chapter 2

Nanoscale Displacement Measurements

In order to conduct sensitive measurements with MEMS and NEMS devices it is first necessary to be able to measure these devices with great precision. In this chapter we discuss the different optical measurement techniques used to conduct the measurements presented in this dissertation. We begin with the most seemingly straightforward method, optical beam deflection, in which the optical beam reflecting from the tip of the microcantilever falls upon a split photodetector, which provides a voltage signal proportional to the tip displacement. This type of optical measurement was used to conduct most of the studies presented in Chapters 4, 5, and 6. We then discuss homodyne and heterodyne Michelson interferometry, the latter of which was used to conduct the measurements presented in Chapter 3. In interferometric measurements two optical beams, one reference beam and one object beam reflected from the tip of the microcantilever, are superimposed to create an interference signal. The motion of the microcantilever modulates the optical path length of the object beam which results in a change in the interference signal which is proportional to the tip displacement. We review these optical detection methods below. In addition, we discuss optical shot noise and how to experimentally determine the focused spot size.

2.1 Optical Beam Deflection

Optical beam deflection has become a ubiquitous method for conducting sensitive optical measurements due to its simplicity and reliability. The method was first

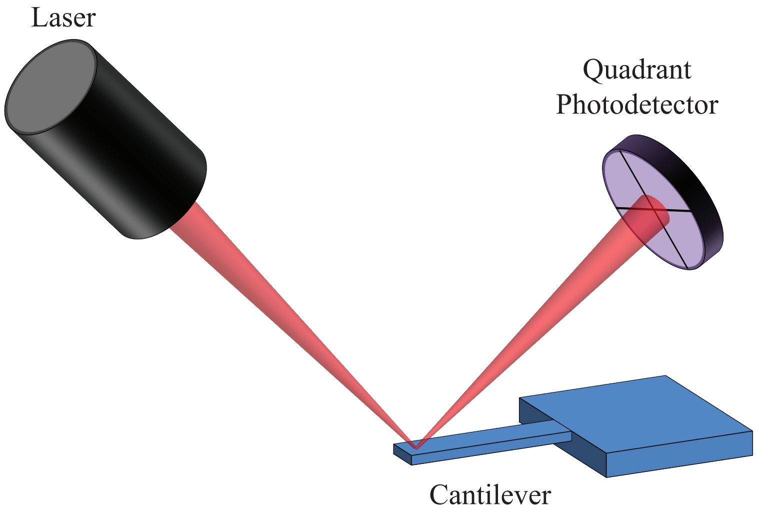

Figure 2·1: Optical beam deflection setup.

introduced by Meyer and Amer (Meyer and Amer, 1988) as a simpler alternative to interferometric detection, to monitor cantilever deflections in the atomic force microscope. This brought the method into wide use and it was soon implemented in commercial AFM systems and laboratory settings.

A basic schematic of an optical beam deflection measurement is depicted in Figure 2·1. In the figure, laser light is focused down to the tip of the backside of a microcantilever. The reflected light is directed onto a split photodetector where the incident light is converted into an electrical signal. The signal at each quadrant is independently amplified and the normal motion of the cantilever can be read out by taking the difference signal between the top and bottom quadrants. A four-quadrant photodetector enables measurement of both the normal and lateral motion of the cantilever (Meyer and Amer, 1990). This is achieved by taking the difference signal between either the top and bottom quadrants (normal motion) or the left and right quadrants (lateral motion).

Optical beam deflection is most attractive as a measurement method because of its relative simplicity and versatility. In Chapter 4 we use the technique to measure the fluctuations of a microcantilever held inside a vacuum chamber. In Chapter 5 we use it to monitor the motion of a cantilever which is inside of a fluid cell. In Chapter 6 we measure the motion of a cantilever which is held inside of a microchannel. The use of optical beam deflection in all of these studies led to experimental setups that were much easier to manipulate and more compact than interferometry based systems, yet gave excellent detection sensitivity (~ 500 fm/Hz$^{1/2}$).

Though the optical beam deflection method appears to be simple, it can be used to conduct measurements with atomic resolution (Alexander et al., 1989). In practice, the sensitivity of the technique can meet or even exceed that of interferometric methods (Putman et al., 1992). Here, we briefly review the sensitivity in an optical beam deflection measurement. We consider a Gaussian laser spot incident on a cantilever of length l with normal displacement Δz at its tip. If x is the distance between the cantilever and the photodetector, we see that the displacement of the spot at the detector Δs will be

$$\Delta s \approx 2 g_1 \frac{\Delta z}{l} x, \tag{2.1}$$

where g_1 is a dimensionless geometric parameter taking into account the position of the spot on the cantilever (Putman et al., 1992). If the laser spot has a focused diameter at the cantilever of D_0, the diameter at the photodetector will be

$$D_{\mathrm{pd}} \approx \frac{4\lambda}{\pi} \frac{x}{D_0}, \tag{2.2}$$

where λ is the wavelength of the laser light (Saleh and Teich, 2007). We then find the displacement of the spot at the detector to be

$$\Delta s = g_1 \frac{\pi}{2} \frac{\Delta z}{\lambda} \frac{D_0 D_{\mathrm{pd}}}{l}. \tag{2.3}$$

We see that the displacement of the spot on the detector (and therefore, the differential signal between the top and bottom quadrants) is linearly proportional to the cantilever tip displacement Δz. If the optical beam has a Gaussian intensity profile, the differential optical power ΔP at the detector is

$$\Delta P = 4\sqrt{\frac{2}{\pi}}\frac{\Delta s}{D_{\text{pd}}}P_{\text{tot}}, \tag{2.4}$$

where P_{tot} is the total optical power. For a shot-noise limited system, the shot noise power (square of the current) is given as $(\Delta i)^2 = 2e\Delta f \langle i \rangle$, where Δf is the bandwidth of the detection system and $\langle i \rangle$ is the average photocurrent on the detector. Considering these equations, we find the signal-to-noise ratio (SNR) of the measurement to be

$$\text{SNR} = \left(\frac{\lambda \eta P}{hc\Delta f}\right)^{1/2} 2\sqrt{\pi} g_1 \frac{\Delta z}{l}\frac{D_0}{\lambda}. \tag{2.5}$$

We see from this equation that the sensitivity of the measurement is independent of the distance between the cantilever and the detector. Although the displacement of the spot is proportional to this distance, so is the size of the spot. The SNR can be increased by increasing the optical power, decreasing the measurement bandwidth, and by ensuring that the focused spot is incident at the tip of the cantilever. More details regarding the sensitivity of optical beam deflection measurements can be found in the literature (Lee et al., 2010; Putman et al., 1992).

Because optical beam deflection is a non-interferometric transduction technique, it is not easy, in practice, to obtain the transduction gain (the conversion factor for the displacement into Volts) directly, although some clever schemes have been devised (Shusteff et al., 2006). Instead, the gain is typically determined by calibrating against a measurement of a known quantity (such as scanning the cantilever over a step of known height). In the experiments presented in Chapters 4, 5, and 6, we measure the thermal noise amplitude of the cantilever oscillations and calibrate it against the equipartition theorem result ${z_{\text{rms}}}^2 = k_{\text{B}}T/\kappa$ (Butt and Jaschke, 1995), with the cantilever stiffness κ calculated from elasticity considerations to be (Cleland, 2003)

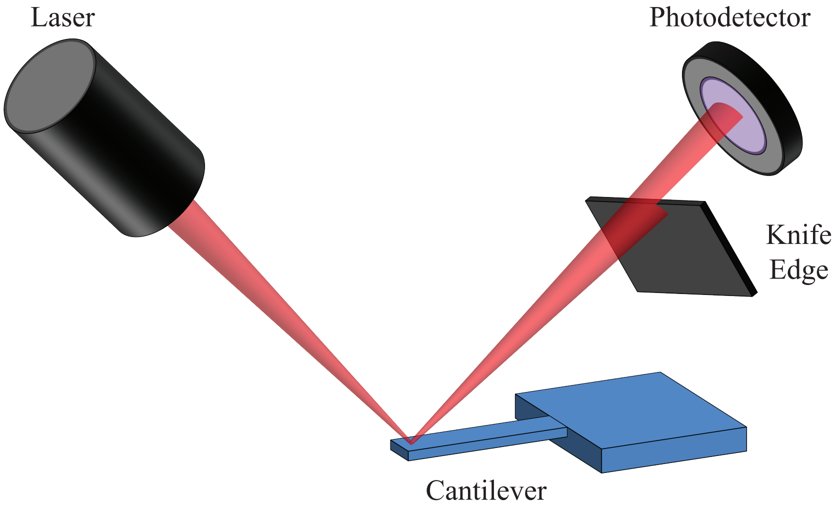

Figure 2·2: Knife-edge optical detection scheme.

$\kappa = Ewh^3/(4l^3)$, where E is the Young's modulus and l, w, and h are the length, width, and thickness of the cantilever, respectively. Interferometric techniques, however, are inherently calibrated against the wavelength of laser light used (as we will see below) and can provide a direct displacement calibration.

2.1.1 Knife-Edge Detection

Knife-edge optical detection is an alternative beam deflection technique that doesn't require a split or quadrant photodetector. Here, an opaque flat plate with a sharp edge is placed in front of the photodetector to block half of the light reflecting from the device under test, as illustrated in Figure 2·2. Because of the knife edge, as the cantilever moves the optical power on the photodetector varies proportionally with the displacement of the cantilever tip (Karabacak et al., 2006); this allows for monitoring the oscillations of the cantilever with good displacement sensitivity. The first microcantilever-based bacteria studies presented in Chapter 5 were conducted using the knife-edge method. Knife-edge systems are often used to measure the size of optical spots (Khosrofian and Garetz, 1983), as we will demonstrate in Section 2.4.

2.2 Michelson Interferometry

Michelson interferometry is a widely used optical measurement technique that can provide ultrasensitive measurements of sub-nanoscale fluctuations. Ultimately, the accuracy of these measurements are limited only by the accuracy with which the optical wavelength is known (Lawall et al., 2001). Heterodyne interferometers, for example, can achieve accuracy as small as 10 pm (Lawall and Kessler, 2000). In an interferometer, two optical beams, one reference beam and one object beam, are superimposed to interfere with one another. The degree of constructive or destructive interference between the beams provides information about their relative phases which can be related to the change in the path length of one of the beams. In our experiments, The motion of the microcantilever modulates the optical path length of the object beam which results in a change in the interference signal which is proportional to the tip displacement. Here, we review the theory of operation of homodyne and heterodyne Michelson interferometry, the latter of which was used to conduct the measurements presented in Chapter 3.

2.2.1 Homodyne Interferometry

In homodyne interferometry, the two optical beams are of the same wavelength and a change in the path length of one of the beams creates a change in the interference between the beams which results in a change in the intensity of light at the photodetector. To see this, let us consider two optical beams of monochromatic light of wavelength λ. If the reference and object beams traverse a total path of length z_R and $z_O - 2\delta$, respectively, they can be represented at the detector as

$$A_R = a_R e^{i(\omega t - k z_R)}$$

$$A_O = a_O e^{i(\omega t - k(z_O - 2\delta))} \tag{2.6}$$

where $\omega = 2\pi c/\lambda$, $k = 2\pi/\lambda$, and 2δ is the variation in the object path length due to the motion of the device under test (Wagner, 1990). The total optical intensity at the detector will then be

$$\begin{aligned} I_D &= |A_O + A_R|^2 = (A_O + A_R)(A_O^* + A_R^*) \\ &= a_O^2 + a_R^2 + 2a_O a_R \cos\left[k(z_R - z_O) + 2k\delta\right]. \end{aligned} \tag{2.7}$$

If the displacement is much smaller than the wavelength of light ($\delta \ll \lambda$) this reduces to

$$\begin{aligned} I_D &= \left(a_O^2 + a_R^2\right)\left\{1 + 2\frac{a_R a_O}{a_O^2 + a_R^2}\left[\cos k(z_R - z_O)\cos 2k\delta - \sin k(z_R - z_O)\sin 2k\delta\right]\right\} \\ &\sim \left(a_O^2 + a_R^2\right)\left\{1 + 2\frac{a_R a_O}{a_O^2 + a_R^2}\left[\cos k(z_R - z_O) - 2k\delta \sin k(z_R - z_O)\right]\right\}. \end{aligned} \tag{2.8}$$

We see from this expression that the optical intensity on the detector can be separated into a constant background illumination (first two terms in brackets) and an illumination that is proportional to the device displacement δ (third therm in brackets). Further, we see that in the case $z_R - z_O = n\lambda$ where n is any integer, the total intensity is maximized and we have $I_{max} = (a_O^2 + a_R^2) + 2a_R a_O$. The minimum case occurs when $z_R - z_O = n\lambda/2$ where n is an odd integer, and we have $I_{min} = (a_O^2 + a_R^2) - 2a_R a_O$. Finally, we see that in the case $z_R - z_O = n\lambda/4$ where n is an odd integer, the background will be minimized, the term proportional to the displacement will be maximimized, and we will have

$$I_D = \frac{1}{2}\left(I_{max} + I_{min}\right) - \frac{2\pi\delta}{\lambda}\left(I_{max} - I_{min}\right). \tag{2.9}$$

In our experiments, we use active path-length stabilization to fix the interferometer in the condition described in Eq. (2.9) to achieve the best possible sensitivity. This stabilization also serves to compensate for any drifts that may occur in the setup due to temperature fluctuations, room vibrations, and other low frequency environmental perturbations. This optical signal is read out at the photodetector. For fluctuating displacements δ, the DC detector output will be proportional to the background signal (first term in Eq. (2.9)) and the AC detector output will be proportional to the fluctuating optical power (second term in Eq. (2.9)). The detector voltage outputs will be $V_{DC} = P_{DC}R_{DC}\mathcal{R}$ and $V_{AC} = P_{AC}R_{AC}\mathcal{R}$ where $\mathcal{R}$ is the detector responsivity, R_{AC} and R_{DC} are the AC and DC detector gains, and P_{DC} and P_{AC} are the background and fluctuating components of the optical signal. Considering these we see that the fluctuating voltage will be

$$V_{AC} = \delta \frac{2\pi}{\lambda} R_{AC}\mathcal{R}\left(V_{max} - V_{min}\right), \tag{2.10}$$

which becomes

$$V_{AC} = \delta \frac{2\pi}{\lambda} \frac{R_{AC}}{R_{DC}} V_{p-p}, \tag{2.11}$$

where $V_{p-p} = V_{max} - V_{min}$ is the peak-to-peak difference between the maximum and minimum DC output. We see that the fluctuating voltage is linearly proportional to the displacement of the device. The minimum detectable displacement can be improved by maximizing V_{p-p} (by improving the alignment and balancing the optical power in each beam path).

The basic layout of the path-stabilized, polarizing, homodyne Michelson interferometer used in this work is shown in Figure 2·3. Light from a helium-neon laser is directed through an optical isolator and collimating optics (not shown), through a half-wave plate, and to a polarizing beam splitter (PBS). The wave plate allows for direct control of the polarization of the linearly polarized laser light, thereby controlling the proportion of light that will be transmitted or reflected at the PBS. The transmitted beam (the object beam) passes through a quarter-wave plate, is focused through the objective to the device under test, and is reflected all the way back to

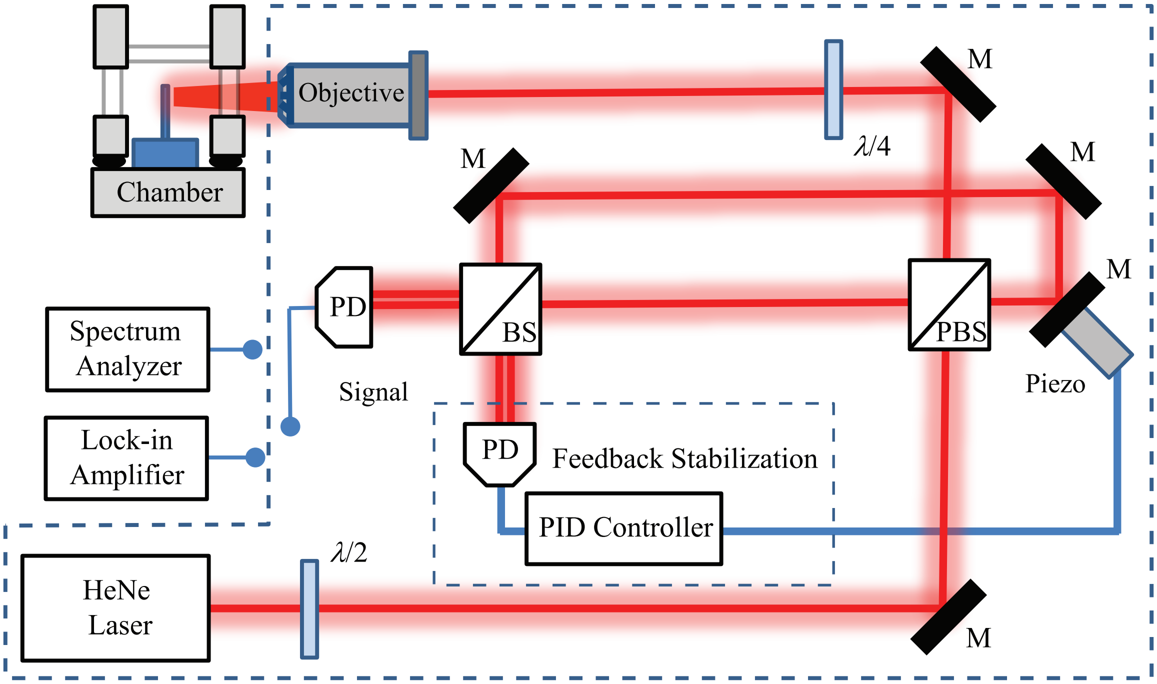
Chamber
Objective
M
λ/4
M
M
M
PD
BS
PBS
Piezo
Spectrum Analyzer
Lock-in Amplifier
Signal
PD
Feedback Stabilization
PID Controller
HeNe Laser
λ/2
M

Figure 2·3: Schematic of a path-stabilized, polarizing, homodyne interferometer. PD: photodetector, BS: beam splitter, PBS: polarizing beam splitter, M: mirror.

the PBS. The double pass through the quarter-wave plate shifts the polarization of the light so that it reflects upon its return at the PBS (Saleh and Teich, 2007) and is directed onto the non-polarizing beam splitter (BS). The reference beam is initially transmitted through the PBS, reflected off a series of mirrors, and directed to the BS. One of the mirrors is mounted on a linear piezo actuator so that the path length of the reference beam can be controlled to compensate for slow mechanical drifts in the system and to keep the system at the point of optimal sensitivity, as described above. The object and reference beam are carefully aligned so that they interfere at the BS. The beams are then split 50/50 and directed to two photodetectors; one is used for feedback stabilization of the system and the other is used to make measurements of the fluctuating signal. The feedback stabilization signal is sent to a proportional-integral-derivative (PID) controller which drives the piezo actuator to achieve stable closed-loop control.

2.2.2 Heterodyne Interferometry

In heterodyne interferometry, beams of two different optical frequencies are used and the signal of interest is recovered after electronically demodulating the signal on the photodetector (Wu et al., 1999). The technique is used to shift a measurement signal to a different frequency range. In our experiments, we employ a heterodyne interferometer to shift our signal up by 40 MHz to avoid interference in our signal from low frequency noise in our helium-neon laser. The laser is shot noise limited and has a much cleaner spectrum at 40 MHz so this is a desirable range to use for a sensitive measurement.

Let us consider two optical beams of initially monochromatic light of optical frequency ω (wavelength $\lambda = 2\pi c/\omega$). If the reference and object beams traverse a total path of length z_R and $z_O - 2\delta$, respectively, and if the reference beam is modulated at frequency ω_m, they can be represented at the detector as (Wagner, 1990)

$$A_R = a_R e^{i[(\omega+\omega_m)t - kz_R]}$$

$$A_O = a_O e^{i[\omega t - k(z_O - 2\delta)]}. \tag{2.12}$$

The total optical intensity at the detector will then be

$$I_D = |A_O + A_R|^2 = (A_O + A_R)(A_O^* + A_R^*), \tag{2.13}$$

and we find

$$I_D = \left(a_O^2 + a_R^2\right)\left\{1 + 2\frac{a_R a_O}{a_O^2 + a_R^2}\cos\left[\omega_m t + k(z_R - z_O) + 2k\delta\right]\right\}. \tag{2.14}$$

We see that the signal on the photodetector varies sinusoidally in time at the modulation frequency ω_m and has a phase-shift which is proportional to the device displacement δ. In order to demodulate the heterodyne signal, we must mix it down with a signal from a local oscillator (LO) of the form $a_{LO}\cos(\omega_m t + \phi_{LO})$ where a_{LO} and ϕ_{LO} are the amplitude and phase of the LO. The output from the mixer will be

$$\frac{a_D a_{LO}}{2}\left\{\cos\left[k(z_R - z_O) - \phi_{LO} + 2k\delta\right] + \cos\left[2\omega_m t + k(z_R - z_O) + \phi_{LO} + 2k\delta\right]\right\}, \tag{2.15}$$

where a_D is the amplitude of the oscillating signal on the detector. We note that the first term in Eq. (2.15) has no dependence on the carrier frequency and the second term oscillates at $2\omega_m$. We filter out this second term using a low pass filter and use the first term as our measurement signal. In our setup we use active feedback control to compensate for drifts in the system by setting ϕ_{LO} such that $k(z_R - z_O) - \phi_{LO} = 0$ and the first term in Eq. (2.15) varies only with the device motion δ. For small displacements, we end up with an output voltage signal that is directly proportional to δ.

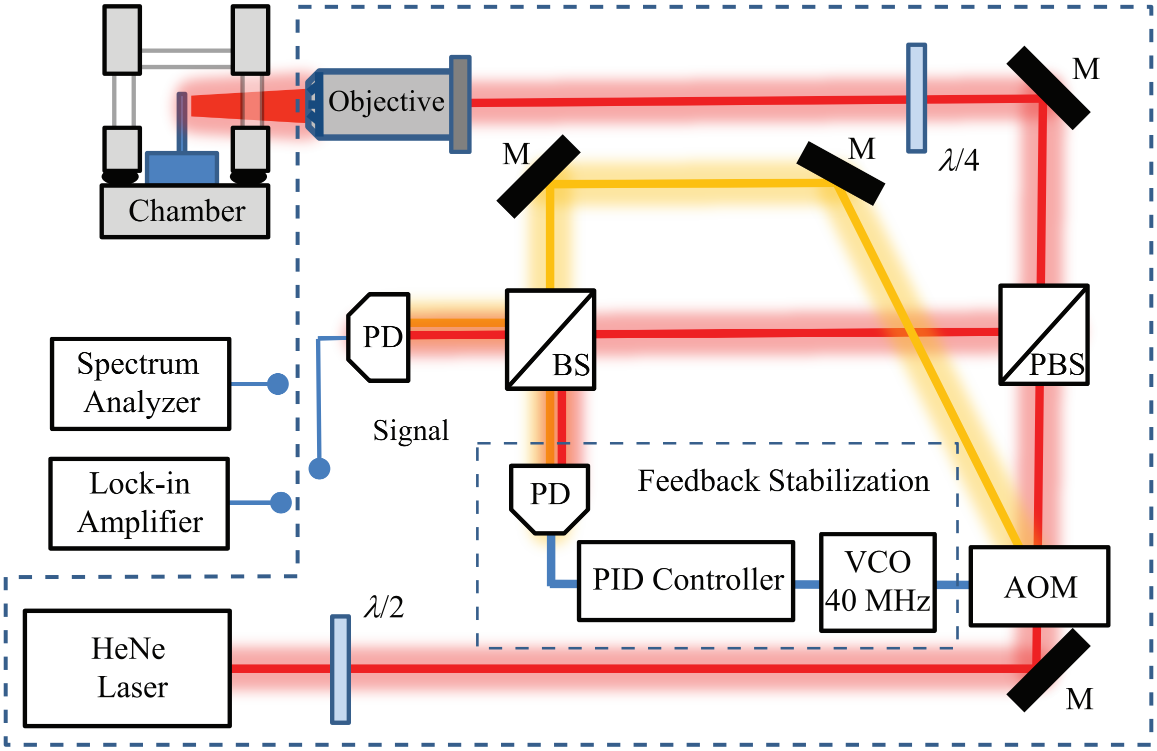
Chamber
Objective
M
λ/4
M
M
PD
BS
PBS
Spectrum Analyzer
Lock-in Amplifier
Signal
Feedback Stabilization
PD
PID Controller
VCO 40 MHz
AOM
HeNe Laser
λ/2
M

Figure 2·4: Schematic of a frequency-stabilized, polarizing, heterodyne interferometer. PD: photodetector, BS: beam splitter, PBS: polarizing beam splitter, M: mirror.

The basic layout of a heterodyne Michelson interferometer is shown in Figure 2·4. The key benefit of a heterodyne interferometer over a homodyne interferometer is its ability to carry the measurement signal to a much higher frequency by modulating the optical frequency of the reference beam. This can be achieved in many ways, but here we use an acousto-optic modulator (AOM) which is driven by a 40 MHz sinusoidal drive. In the figure, the unmodulated light is shown in red and the frequency-shifted light is shown in orange. Light from a helium-neon laser is directed through an optical isolator and collimating optics (not shown), through a half-wave plate, and through the AOM. Half of the light passes directly through the AOM unchanged and is transmitted through the polarizing beam splitter (PBS). This beam (the object beam) passes through a quarter-wave plate, is focused through the objective to the device under test, and is reflected all the way back to the PBS. It is then reflected and is directed onto the non-polarizing beam splitter (BS). The reference beam (shown in orange) is frequency modulated at the AOM and is directed to the BS where it interferes with the object beam. The beams are then split 50/50 and directed to two photodetectors, as in the case of the homodyne interferometer. We achieve feedback stabilization in this setup by modulating the drive frequency of the AOM. Briefly, we feed the detector signal to a PID controller which sends a DC control voltage to the voltage controlled oscillator (VCO) which drives the AOM. The PID parameters are chosen such that a stable feedback loop tracks the low frequency phase shifts in the detector signal and compensates by modulating the AOM frequency.

2.3 Optical Shot Noise

Optical shot noise is the noise in an optical measurement caused by the quantized nature of the arrival of photons at the photodetector. In other words, the fluctuations in the number of photons arriving at the detector cause fluctuations in the photocurrent that place an intrinsic limit on the sensitivity of any optical measurement. When constructing an optical measurement system it is often desirable to reduce all sources of noise in the system so that the unavoidable optical shot noise provides the greatest noise contribution. Such a system is said to be shot noise limited. In order to test whether a system meets this criteria one can measure the spectral content of the optical signal as a function of the average optical power. For light which has Poissonian photon statistics we expect the time-independent average current $\langle i \rangle$ and the time-varying fluctuating current Δi to follow $(\Delta i)^2 \propto \langle i \rangle$ (Fox, 2006), where we have separated the photocurrent as $i(t) = \langle i \rangle + \Delta i$. The noise power in the signal is related to the fluctuations in the photocurrent as

$$P_{noise}(t) = \Delta i(t)^2 R_{Load} \tag{2.16}$$

where R_{Load} is the load resistance of the photodetector. Upon taking the Fourier transform of $i(t)$ and measuring the variance of the current fluctuations within a frequency band Δf, we find (Fox, 2006)

$$(\Delta i)^2 = 2e\Delta f \langle i \rangle , \tag{2.17}$$

where e is the elementary charge. We write the noise power as

$$P_{noise}(f) = 2e\Delta f R_{Load} \langle i \rangle . \tag{2.18}$$

The average voltage and fluctuating voltage at the photodetector output are related to the average photocurrent and fluctuating photocurrrent by $\langle V \rangle = \langle i \rangle R_L^{DC}$ and $\Delta V = \Delta i R_L^{AC}$ where R_L^{DC} and R_L^{AC} are the DC and AC photodetector gains, respectively. Combining the above equations we can write the spectral density of the

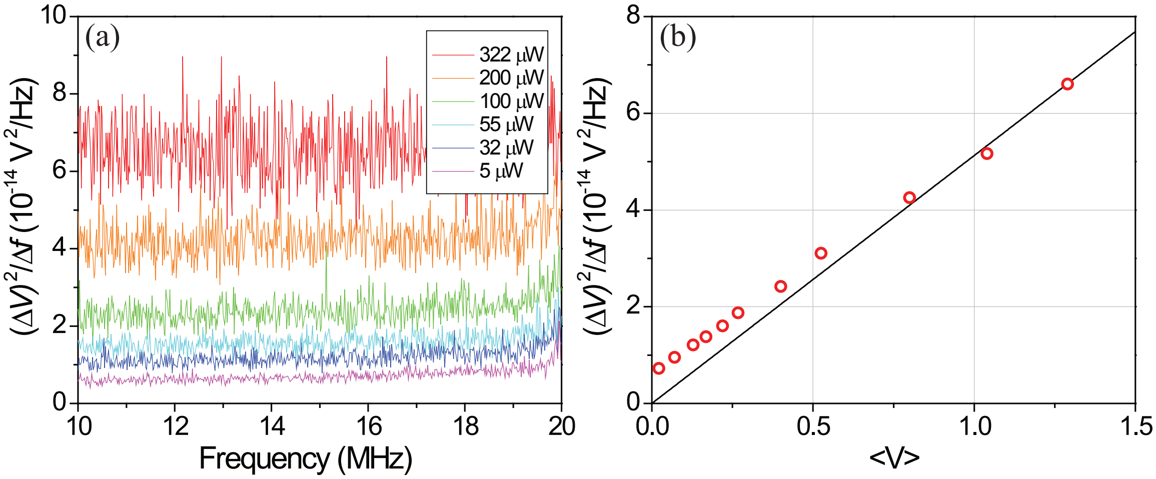

Figure 2·5: Optical shot noise of a 0.8 mW helium-neon laser with $\lambda = 632.8$ nm.

voltage fluctuations as

$$\frac{(\Delta V)^2}{\Delta f} = \frac{2e\left(R_L^{AC}\right)^2}{R_L^{DC}} \langle V \rangle \,. \tag{2.19}$$

We see that the spectral density of the fluctuations is linearly proportional to the average voltage from the detector.

In Figure 2·5 we present a measurement of the shot noise of a 0.8 mW helium-neon laser ($\lambda = 632.8$ nm) incident on an amplified photodetector (New Focus Model 1801-FS). Here, the light is directed through a continuously variable neutral density filter wheel and onto the detector. A spectrum analyzer is used to measure the spectral density of the voltage fluctuations $(\Delta V)^2/\Delta f$ at high frequency (between 10 and 20 MHz) and a multimeter is used to measure the average voltage $\langle V \rangle$. The spectrum of the voltage fluctuations on the photodetector are shown in Figure 2·5(a) for various values of average optical power. We plot the average of the spectral density of the voltage fluctuations (averaged in the range 10 - 20 MHz) versus the mean voltage in Figure 2·5(b). The theory, Equation (2.19), is also plotted as a solid line. We see from the agreement between experiment and theory at larger optical power levels that this system is shot noise limited. We do note, however, that that there is disagreement

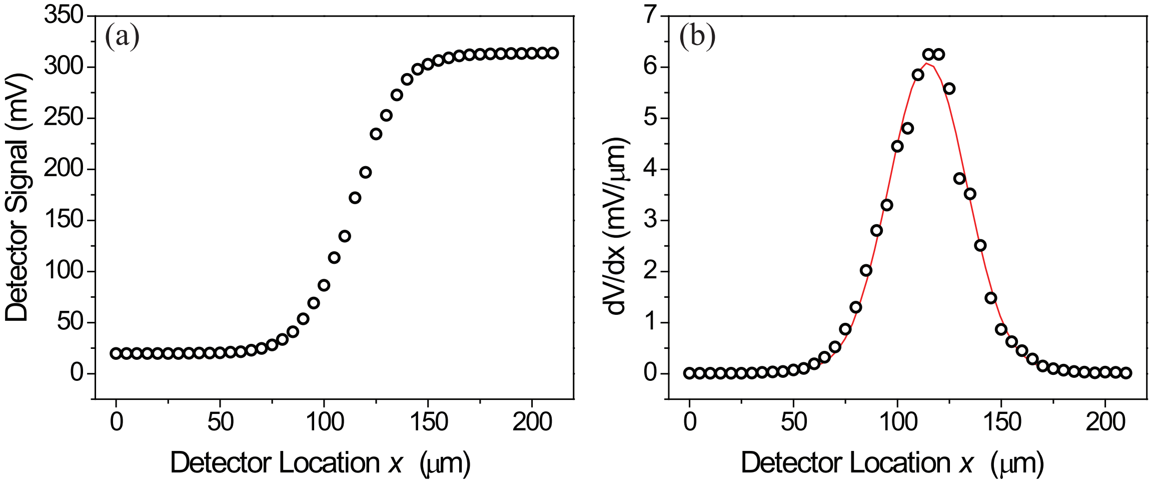

Figure 2·6: Measurement of optical spot size.

between data and theory for the lowest optical power levels. In this range, our measurement is limited by the electrical noise in the detector circuit. More details regarding shot noise limited detection can be found in the literature (Fox, 2006; Saleh and Teich, 2007) and in other thesis work (Ozsun, 2014).

2.4 Optical Spot Size

When making optical measurements, it is often necessary to determine the focused spot size of a laser beam. A focused beam should have an intensity profile defined as

$$I\left(r,z\right)=I_0\left(\frac{W_0}{W(z)}\right)^2 e^{-\frac{2r^2}{W(z)^2}} \tag{2.20}$$

where $W(z)$ is the beam width and $r=\sqrt{x^2+y^2}$ and z are the radial and axial positions, respectively. At any axial location z, the intensity is a Gaussian function of the radial position r with its peak at $r=0$.

We can measure the spot size of a focused spot by positioning a photodetector at the beam focus, mounting a knife edge in front of the detector, and by moving the detector-knife-edge setup past the beam. If the detector is translated in the x

direction, the total optical power measured on the detector will be (Khosrofian and Garetz, 1983)

$$P\left(x_b\right)=\int\limits_{-\infty}^{\infty}\int\limits_{-\infty}^{x_b} I\left(x,y\right)dxdy, \tag{2.21}$$

where x_b is the x coordinate of the knife-edge. We can then measure the intensity profile of the beam by taking the derivative of the signal on the detector with respect to the detector position. A measurement of this type is shown in Figure 2·6. In Figure 2·6(a) we show the mean photodetector signal versus the location of the photodetector x. The signal reaches a saturation on each side of the curve because we have moved the detector from a position where the light is completely blocked ($x \approx 0$ μm) to a position where all of the light reaches the detector ($x \approx 200$ μm). In Figure 2·6(b) we show the derivative of the signal with respect to the detector position. By fitting the data to a Gaussian lineshape (red line) we extract the full width at half maximum of the curve which is the same as the focused spot size (37.5 μm in this case).

Chapter 3

Estimation of Modal Parameters from Resonance Measurements

3.1 Background

To a very good approximation, a mechanical resonator oscillating in one of its resonant modes behaves like a damped harmonic oscillator. Coupling this oscillatory motion to external physical phenomena allows for very sensitive measurements of the phenomena. This resonant measurement paradigm works well over length scales that span many orders of magnitudes — from macroscopic gravitational wave detectors all the way down to nanomechanical resonators. Mechanical resonators with typical dimensions in the micron and sub-micron range (also known as micro- and nano-electro-mechanical systems (MEMS and NEMS)) have enabled sensitive measurement applications, including mass detection (Yang et al., 2006), rheology (Ahmed et al., 2001), charge measurements (Cleland and Roukes, 1998), and temperature sensing (Zhang et al., 2013) among many others. Apart from sensing, small mechanical resonators have facilitated studies of fundamental physical phenomena, e.g., those rooted in quantum mechanics.

Typically, MEMS and NEMS resonators are fabricated using standard photolithographic techniques in a clean-room environment. Some common geometries are depicted in Figure 3·1. The devices used in this study all have dimensions on the order of tens or hundreds of microns, however, their mechanical displacements are sometimes only fractions of a nanometer. They usually possess high intrinsic quality factors (small internal damping), high natural frequencies, and minuscule active masses.

The measured quantity in a resonant measurement is typically determined in terms of the modal parameters of the mechanical resonator. In mass sensing, for instance, the added mass is expressed in terms of the modal mass M_j and the resonance frequency $\omega_j = 2\pi f_j$ of (the j^{th} mode of) the resonator, and other parameters of the measurement. For an accurate resonant measurement, it is therefore essential that all the modal parameters be accurately established, requiring a careful determination of the linear dimensions. While microscopy techniques can provide high resolution images for this purpose, it is important to obtain an independent mass (and subsequent spring constant) measurement. This is because in commonplace MEMS and NEMS — e.g., cantilevers, doubly-clamped beams, or membranes — there typically is a small thickness dimension, the uncertainties in which strongly affect the modal parameters, and which is hard to determine accurately. Furthermore, in multi-layer structures fabricated through etching and deposition steps, there are always thickness uncertainties. For example, for a microcantilever of linear dimensions $l \times w \times h$, the uncertainty in the modal mass can be quantified as $\delta M_j = M_j \left(\frac{\delta l}{l} + \frac{\delta w}{w} + \frac{\delta h}{h}\right)$, where

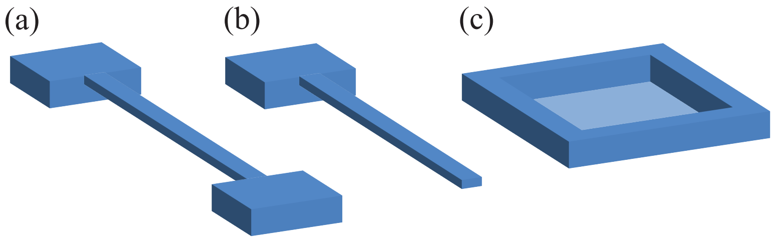

Figure 3·1: Illustrations of some common geometries of microscale and nanoscale resonators. The devices depicted are (a) a doubly-clamped beam, (b) a cantilevered beam, and (c) a rectangular membrane.

the effective modal mass is

$$M_j = \rho l w h \int_0^l \Psi_j(x)^2 dx, \tag{3.1}$$

with $\int_0^l \Psi_j(x)^2 dx = \alpha$ being the eigenfunction normalization. Assuming $h \ll w, l$ and a given standard deviation in the measurement of the linear dimensions, the uncertainty δh has a more significant effect on the error. Furthermore, if ρh can be determined, this directly leads to the modal mass.

In this chapter we show how to determine ρh, and consequently the modal mass, from thermal fluctuations and gas damping measurements. The parameters of the devices used in this study, which include cantilever and membrane resonators, are listed in Table 3.1. The materials, densities, and dimensions in the table are from manufacturer specifications except in the case of device $M1$ which was measured by optical microscopy (width and length) and by ellipsometry (thickness). We begin with a discussion of thermal noise measurements.

3.2 Thermomechanical Fluctuations

An accurate calibration of the mass of a resonator comes from its thermal fluctuations. Let us illustrate this for a microcantilever in its j^{th} mode under thermal equilibrium

Device	Material	Density ρ (kg/m^3)	Dimensions $l \times w \times h$ (μm^3)	Total Mass m_{total} (kg)
$C1$	Silicon	2330	$110 \times 35 \times 2$	1.79×10^{-11}
$C2$	Silicon	2330	$110 \times 32.5 \times 1$	0.83×10^{-11}
$C3$	Silicon	2330	$90 \times 32.5 \times 1$	0.68×10^{-11}
$C4$	Silicon	2330	$130 \times 32.5 \times 1$	0.98×10^{-11}
$M1$	Silicon Ni	3440	$1260 \times 1260 \times 0.563$	3.07×10^{-9}

Table 3.1: Parameters of devices measured in this study.

at temperature T. We write the time-dependent thermal displacement of any point on the microcantilever as

$$y\left(x,t\right)=\sum_{j=1}^{\infty}\Psi_j\left(x\right)a_j\left(t\right), \tag{3.2}$$

where $\Psi_j\left(x\right)$ and $a_j\left(t\right)$ are the position-dependent mode shape functions and time-dependent displacement functions, respectively, for the j^{th} natural mode of the system. Assuming the modes are well-separated in the frequency domain due to small dissipation and the thermal amplitudes remain extremely small, we can express both the kinetic energy $\mathcal{T}$ and the elastic potential energy $\mathcal{U}$ of the cantilever in terms of the modal amplitude:

$$\langle\mathcal{T}\rangle=\langle\mathcal{U}\rangle\approx\frac{1}{2}\rho wh{\omega_j}^2\left\langle {a_j}^2\right\rangle\int\limits_0^l\Psi_j(x)^2dx. \tag{3.3}$$

Here, the brackets indicate ensemble averaging. We note that each degree of freedom that contributes a quadratic term to the energy of the system has an average energy of $\frac{k_\mathrm{B}T}{2}$, according to the equipartition theorem (Hauer et al., 2013). We assume that we measure the displacement of the mode at point x' along the cantilever such that the measured signal is proportional to $y(x',t)$, as is common in optical detection. Since $y(x',t)\approx\Psi_j(x')a_j(t)$, and considering the equipartion theorem, the thermal energy becomes

$$\frac{1}{2}k_\mathrm{B}T\approx\frac{1}{2}\rho wh{\omega_j}^2\left\langle y(x',t)^2\right\rangle\int\limits_0^l\frac{\Psi_j(x)^2}{\Psi_j(x')^2}dx. \tag{3.4}$$

It is apparent from Eq. (3.4) that ρh and the modal mass M_j (Eq. (3.1)) can be found uniquely to calibrate a measurement if the mean-square displacement and resonance frequency can be determined with some accuracy.

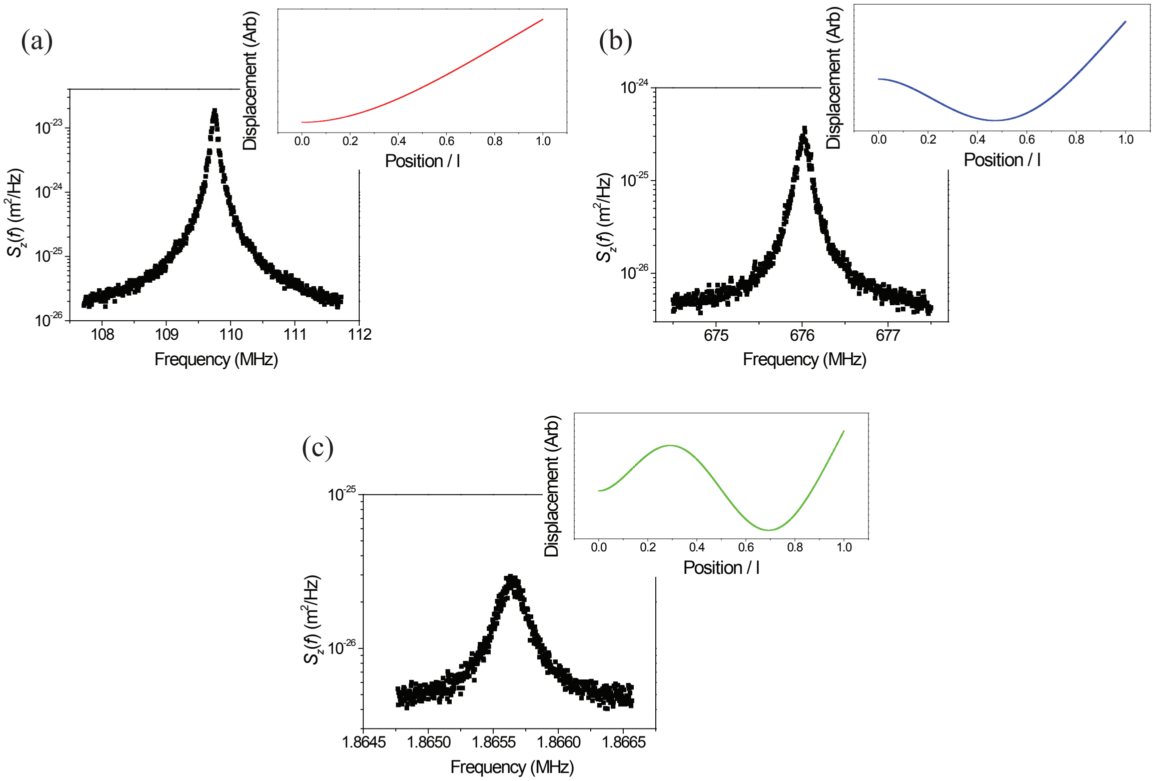

Figure 3·2: Thermal spectra and mechanical modeshapes of cantilever $C4$ for the (a) first, (b) second, and (c) third mechanical modes. The modeshapes are computed using simple beam theory.

3.2.1 Measurements

In order to test these ideas, we first perform experiments on microcantilevers. The microcantilevers are placed in a variable pressure chamber with optical viewports. A heterodyne optical interferometer with a noise floor of 10 fm/Hz$^{1/2}$ at 1 mW optical power is used for measuring the microcantilever oscillations. Figure 3·2 shows the results of measurements on a cantilever (device $C4$) with $l \times w \times h = 130 \times 32.5 \times 1\ \mu\text{m}^3$. The thermal spectra and mechanical modeshapes are shown for the first (a), second (b), and third (c) harmonic modes of the cantilever. An estimate of the mean-square displacement of each mode of the device $\langle y(x', t)^2 \rangle$ can be found by integrating the total power under each of these curves. The modal frequencies ω_j can be determined by fitting a Lorentzian lineshape to each curve. Additionally, it is important to carefully determine the location of the measurement x' so that $\Psi_j(x')$ can be found. From these data and using Eq. (3.4), we find ρh to be 3.28×10^{-3}, 3.05×10^{-3}, and 3.16×10^{-3} kg/m^2 for the first, second, and third mechanical modes, respectively. This compares favorably to the value we would expect using the manufacturer stated thickness and density (2.33×10^{-3} kg/m^2).

Estimates of ρh obtained using this method and from gas dissipation measurements are presented in Section 3.4 below for all devices listed in Table 3.1. While the method based on thermal fluctuations is accurate, a thermal noise measurement is more difficult in practice than a driven measurement. Below, we explain how ρh can be measured accurately from gas dissipation measurements.

3.3 Gas Damping

In this section we explore how measurements of gas dissipation in the rarefied gas regime can be used to provide an alternative calibration of ρh and the modal mass. We begin with a discussion of gas damping in the hydrodynamic and the kinetic regimes and present experimental measurements of the dissipation on cantilever and membrane resonators.

When a resonant mechanical device is held in a high-vacuum environment the most significant source of dissipation is typically from internal losses in the material (Hosaka et al., 1995). If the pressure in the environment is increased from vacuum, gas damping will provide an increasingly large contribution to the overall measured dissipation and the quality factor of the device's resonance will decrease. To describe the dissipation of energy in a fluidic environment it is first necessary to determine what parameter space the fluid is in and what physical laws are appropriate. Significant attention has been given to the transition from the hydrodynamic to the kinetic gas regime in the literature by our group (Ekinci et al., 2010; Ekinci et al., 2008; Karabacak et al., 2007; Yakhot and Colosqui, 2007) and others (Svitelskiy et al., 2012; Svitelskiy et al., 2009) and in other thesis work (Karabacak, 2008). In particular, Yakhot et al. (Yakhot and Colosqui, 2007) developed a scaling relation to describe the crossover. Ekinci et al. (Ekinci et al., 2008) later showed, using experimental data, that this relation was in fact a universality, useful in most nanoflows regardless of geometry. It was proven that the relative time scales in the system (the Weissenberg number) were the most important in determining when the transition from hydrodynamics to kinetics occurs.

In general, the classical continuum description of flow can be used if the fluid mean-free path λ is much smaller than the characteristic length scale $\mathcal{L}$ of the flow, $\lambda \ll \mathcal{L}$, or equivalently, when the dimensionless Knudsen number Kn is small $\left(\mathrm{Kn} = \frac{\lambda}{\mathcal{L}} \ll 1\right)$. Gas flows in this parameter space are typically well described by Newtonian fluid dynamics. In this regime, viscous air damping is the dominant dissipation mechanism. At lower pressures, where the mean-free path between molecules is larger, the assumptions of classical fluid dynamics begin to break down (Bhiladvala and Wang, 2004). In particular, this transition will typically occur when the mean-free path is close to the characteristic length scale of the flow (Kn $\approx$ 1). In the low pressure regime (where $\lambda \geq \mathcal{L}$) the fluid must be treated as a rarefied gas.

In addition to this length scale dependence, the interaction between the fluid and the mechanical oscillator is also strongly dependent on the relative time scales in the system. The relaxation time of the fluid τ_f scales inversely with the pressure $\left(\tau_f \propto \frac{1}{p}\right)$ (Yakhot and Colosqui, 2007) and the mechanical oscillator time scale is generally taken as the period of oscillation $\tau_m = T = \frac{2\pi}{\omega}$. Classical fluid dynamics is valid when the relaxation time scale is shorter than the time scale of any perturbation to the flow ($\tau_f \ll \tau_m$), or when the dimensionless Weissenberg number Wi is small $\left(\mathrm{Wi} \approx \frac{\tau_f}{\tau_m} \ll 1\right)$. However, an oscillator-driven nanoscale flow may reach very high frequencies or very small time scales. In these cases classical assumptions do not hold. Here, it is possible that the relaxation time scale of the fluid is actually larger than the time scale of the mechanical oscillator. In this regime, where $\tau_m \leq \tau_f$, the fluid again must be treated as a rarefied gas.

To illustrate the transition from the hydrodynamic regime to the kinetic gas regime we present a measurement of the dissipation on a cantilever beam in Figure 3·3. Here, we measure the fluctuations of a silicon microcantilever oscillating in an unbounded nitrogen gas environment. By fitting the power spectral density of the cantilever's oscillations to a Lorentzian line shape we can extract the quality factor Q of the resonance. This quality factor is inversely proportional to the total dissipation in the system which may arise from many possible intrinsic and extrinsic sources. By measuring the dissipation in a vacuum environment we can identify the intrinsic damping ($1/Q_i$) and subtract this from the total measured damping ($1/Q_m$) to find the fluidic damping ($1/Q_f$). Figure 3·3 shows the fluidic dissipation $1/Q_f$ measured as a function of pressure using the fundamental flexural mode of the cantilever with

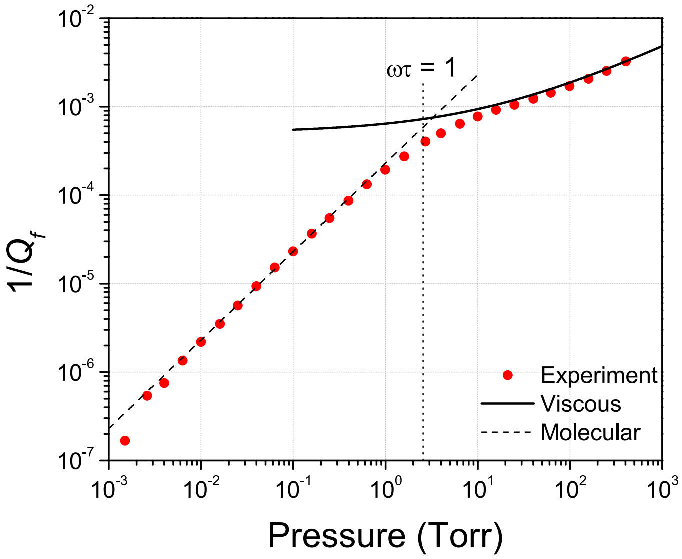

Figure 3·3: $1/Q_f$ measured as a function of pressure p using the fundamental flexural resonance (221 kHz) of a rectangular microlever. Solid line is from viscous theory, as presented in Chapter 4, Eq. (4.2), and the dotted line is from molecular theory, Eq. (3.14). The crossover from the hydrodynamic to the kinetic regime occurs when Wi $\approx$ 1 ($p = 2.6$ Torr).

an oscillation frequency of 221 kHz. It is apparent from the data that there is a physical transition near $p \approx 2.6$ Torr (or at Wi $= 2\pi f \tau_f \approx 1$). At this point the flow transitions from the hydrodynamic to the kinetic regime. At pressures above the transition the dissipation is described using viscous theory. The solid line is a fit to Eq. (4.2) where we have approximated the cantilever as an oscillating sphere, although its cross-section is rectangular (as discussed in Chapter 4). The equation is only fit at larger pressures where the system is in the hydrodynamic regime. At pressures below the transition the dissipation is proportional to the pressure $1/Q_f \propto p$ and we use kinetic theory to describe the flow (dotted line, Eq. (3.14)). One formulation for dissipation in the kinetic regime is described below.

3.3.1 Gas Damping in the Kinetic Regime

In a rarefied gas below the transition to viscous flow, the most significant energy dissipation mechanism for an oscillating resonator is the momentum transfer between the gas molecules and the resonator in the direction of motion. The process is not spatially uniform as the gas collisions only occur on the surface. However, it can be assumed to be uniform on the surface normal to the motion, i.e., the same dissipation occurs per unit area of the resonator on the surfaces normal to the direction of motion. The kinetic model by Christian (Christian, 1966) provides a formula for the dissipative force per unit area acting on a plate moving with velocity u_x in a rarefied gas, Eq. (3.10). Here we review this model.

Transverse Motion of a Plate

We begin by considering an oscillating plate of area A which is held in a gas of volume V with pressure p, as illustrated in Figure 3·4. The plate is laying in the $y - z$ plane and at a given instant it is moving in the $+x$ direction with velocity u_x. We assume that the molecules have a Maxwell-Boltzmann velocity distribution given as

$$dn = n\left(\frac{m}{2\pi k_{\mathrm{B}}T}\right)^{\frac{3}{2}} e^{-\left(\frac{m}{2k_{\mathrm{B}}T}\right)\left(v_x^2+v_y^2+v_z^2\right)} dv_x dv_y dv_z \tag{3.5}$$

where n is the molecular density, m is the mass of one molecule, and v_x, v_y, and v_z are the molecular velocities in the x, y, and z directions. Molecules will strike the plate with velocity $(v_x + u_x)$ at the front surface and $(v_x - u_x)$ at the back surface. The number of molecules that strike the front and back surfaces of the plate per unit time per unit area are $(v_x + u_x)\, dn$ and $(v_x - u_x)\, dn$, respectively. By considering that the pressure exerted on the plate is twice the rate of change of momentum we write the

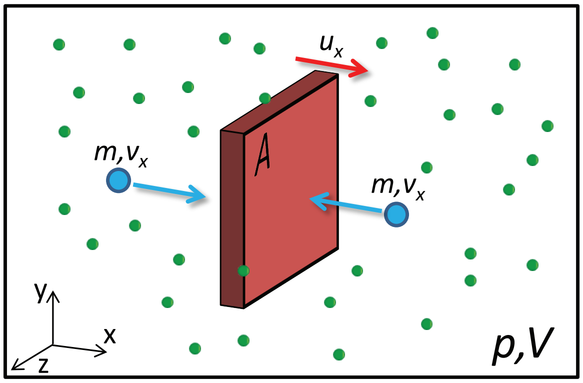

Figure 3·4: Illustration of a rectangular plate of area A moving with velocity u_x in a gas of pressure p and volume V.

differential pressure P_d as

$$P_d = 2m \int_0^\infty [(v_x + u_x)^2 - (v_x - u_x)^2] dn. \tag{3.6}$$

By inserting our definition of dn from Eq. (3.5) and noticing that only the cross-terms $v_x u_x$ survive after subtraction, the integral becomes

$$P_d = 4nu_x \left(\frac{2m^3}{\pi k_\mathrm{B} T}\right)^{\frac{3}{2}} \iiint v_x e^{-\left(\frac{m}{2k_\mathrm{B}T}\right)\left(v_x^2+v_y^2+v_z^2\right)} dv_x dv_y dv_z. \tag{3.7}$$

We must integrate over v_x in the interval from 0 to ∞. This is because the back of the plate will only be struck by molecules with $v_x > 0$ and the front will only be struck by molecules with $v_x < 0$. In the other directions, v_y and v_z, we integrate from $-\infty$ to $+\infty$ because the particles will strike the plate regardless of whether these velocity components are positive or negative.

$$P_d = 4nu_x \left(\frac{2m^3}{\pi k_\mathrm{B} T}\right)^{\frac{3}{2}} \int_{-\infty}^{\infty} e^{\frac{-mv_y^2}{2k_\mathrm{B}T}} dv_y \int_{-\infty}^{\infty} e^{\frac{-mv_z^2}{2k_\mathrm{B}T}} dv_z \int_0^\infty v_x e^{\frac{-mv_x^2}{2k_\mathrm{B}T}} dv_x. \tag{3.8}$$

We compute the integrals over v_y and v_z and find

$$P_d = 4nu_x \left(\frac{2m^3}{\pi k_{\mathrm{B}} T}\right)^{\frac{1}{2}} \int_0^\infty v_x e^{-\frac{mv_x^2}{2k_{\mathrm{B}}T}} dv_x. \tag{3.9}$$

Upon solving the integral over v_x and making the substitution $n = p/k_{\mathrm{B}}T$ we find the differential pressure to be

$$P_d = 4\sqrt{\frac{2}{\pi}}\sqrt{\frac{m}{k_{\mathrm{B}}T}} p u_x. \tag{3.10}$$

We can then multiply by the area of the plate A to compute the total dissipative force on the plate.

Cantilever Beam

In the case of a cantilever beam which has deflection $y\left(x,t\right)$ at position x and time t, we can approximate a small area $dxdz$ on the resonator surface as a plate. We find an expression for the dissipative force for each point on the surface as

$$P_d dxdz = 4\sqrt{\frac{2}{\pi}}\sqrt{\frac{m}{k_{\mathrm{B}}T}} p \frac{\partial y\left(x,t\right)}{\partial t} dxdz. \tag{3.11}$$

Recalling the beam equation for the elastic deflection for a dissipationless structure:

$$\rho wh \frac{\partial^2 y\left(x,t\right)}{\partial t^2} + EI \frac{\partial^4 y\left(x,t\right)}{\partial x^4} = f(x,t). \tag{3.12}$$

Here, ρ is the density and E is the Young's modulus of the beam; $I = wh^3/12$ is its moment of inertia; $f(x,t)$ is assumed to be a harmonic drive force close to the j^{th} resonance frequency ω_j. To introduce to the equation of motion a *constant* and *spatially uniform* dissipation term, one adds $\rho wh \frac{\omega_j}{Q_f}\frac{\partial y(x,t)}{\partial t}$ such that:

$$\rho h \frac{\omega_j}{Q_f} \frac{\partial y\left(x,t\right)}{\partial t} dxdz = 4\sqrt{\frac{2}{\pi}}\sqrt{\frac{m}{k_{\mathrm{B}}T}} p \frac{\partial y\left(x,t\right)}{\partial t} dxdz. \tag{3.13}$$

resulting in

$$\frac{1}{Q_f} = 4\sqrt{\frac{2}{\pi}}\sqrt{\frac{m}{k_{\mathrm{B}}T}}\frac{p}{\rho h \omega_j}, \tag{3.14}$$

and a modal mass

$$M_j = 4\sqrt{\frac{2}{\pi}}\sqrt{\frac{m}{k_{\mathrm{B}}T}}\frac{pQ_f}{\omega_j} lw \int\limits_0^l \Psi_j(x)^2 dx. \tag{3.15}$$

We see from these results that the dissipation in the kinetic regime is proportional to the pressure $1/Q_f \propto p$. Returning to Fig. 3·3 we see good agreement between the experimentally measured dissipation in the kinetic regime and the prediction from Christian's theory, Eq. (3.14). The theory is represented by a dotted line in the figure. The effective mass and ρh can be measured by fitting the equation to the measured data and allowing ρh to be the free parameter of the fit. It is apparent that an independent modal mass calibration can be found by measuring Q_f vs p and the resonator surface area. It should be noted that formulas for modal masses can be found for irregular resonator structures as long as the modal shapes and surface areas are available.

Shear Motion

Shear motion is another important case which should be considered when discussing damping in the kinetic regime. The most dominant movement of a quartz-crystal microbalance, for example, comes from a shearing mode rather than a flexural mode (which is most common in cantilevers, membranes, and beams). If the plate is oriented in the $x - z$ plane, at a given instant the velocity of its top surface may be u_x and the velocity on the bottom will be $-u_x$. Molecules will strike the plate with velocity $(v_x - u_x)$ at the top surface and $(v_x + u_x)$ at the bottom surface. The number of molecules that strike the top and bottom surfaces of the plate per unit time per unit area are $(v_y)\, dn$ for both surfaces, where v_y is the velocity of the molecules in the y direction. Once again, by considering that the pressure exerted on the plate is twice the rate of change of momentum we write the differential pressure P_d as

$$P_d = 2m \int_{0}^{\infty} [v_y\,(v_x + u_x) - v_y\,(v_x - u_x)] dn. \tag{3.16}$$

We must integrate over v_y in the interval from 0 to ∞: this is because the top of the plate will only be struck by molecules with $v_y > 0$ and the bottom will only be struck by molecules with $v_y < 0$. In the other directions, v_x and v_z, we integrate from $-\infty$ to $+\infty$ because the particles will strike the plate regardless of whether these velocity components are positive or negative.

$$P_d = 2nu_x \left(\frac{2m^3}{\pi k_\mathrm{B} T}\right)^{\frac{3}{2}} \int_{-\infty}^{\infty} e^{\frac{-mv_x^2}{2k_\mathrm{B}T}} dv_x \int_{-\infty}^{\infty} e^{\frac{-mv_z^2}{2k_\mathrm{B}T}} dv_z \int_{0}^{\infty} v_y e^{\frac{-mv_y^2}{2k_\mathrm{B}T}} dv_y. \tag{3.17}$$

Upon computing the integrals we find the differential pressure as

$$P_d = 2\sqrt{\frac{2}{\pi}}\sqrt{\frac{m}{k_\mathrm{B}T}} p u_x. \tag{3.18}$$

We see from this result that the dissipation on a plate with shear motion has the same functional dependence as that of a plate moving in the transverse direction (Eq. (3.10)). It is only reduced by a factor of 2.

3.3.2 Measurements

In order to test these ideas, we perform gas dissipation measurements on all of the microcantilevers and membranes listed in Table 3.1. As in the thermal noise measurements, the devices are placed in a variable pressure chamber and a heterodyne optical interferometer is used to measure the oscillations. In these measurements the devices are mounted on a piezo-electric shaker so that they can be driven deterministically. We use a network analyzer to sweep the drive frequency over the resonance of the device and to measure the response of the system.

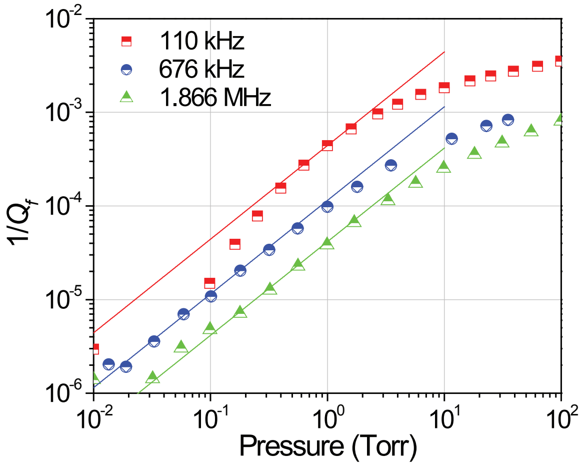

Figure 3·5: Measured fluidic dissipation $1/Q_f$ as a function of pressure p for three modes of device $C4$. Solid lines are fits to Eq. (3.14).

Figure 3·5 shows the dimensionless fluidic dissipation $1/Q_f$ versus the pressure p for the first three modes of device $C4$. Fitting a line through the data points, we extract ρh from Eq. (3.14) to be 4.26×10^{-3}, 3.08×10^{-3}, and 3.08×10^{-3} kg/m^2 for the first, second, and third modes, respectively. Indeed, the agreement is good between these values and those determined from the thermal noise measurements presented above. Further measurements on other cantilevers are listed in Table 3.2 for comparison.

The cantilever results give us confidence to move forward. We next turn to the calibration of a membrane resonator fabricated in a layer of silicon nitride (SiN) deposited onto a silicon substrate. First, we use optical microscopy to measure the length and width of the membrane. Then, we use an ellipsometer to estimate the thickness which we find to be $h = 563$ nm for device $M1$. Next, we characterize the modes of the membrane as shown in Figure 3·6. The mode frequencies $\frac{\omega_{mn}}{2\pi}$ depend linearly on $(n^2+m^2)^{1/2}$ as expected (Timoshenko et al., 1974) for a tension-dominated square membrane. Finally, we select modes and measure the dimensionless dissipation $1/Q_f$ as a function of pressure. We present our results for five modes of

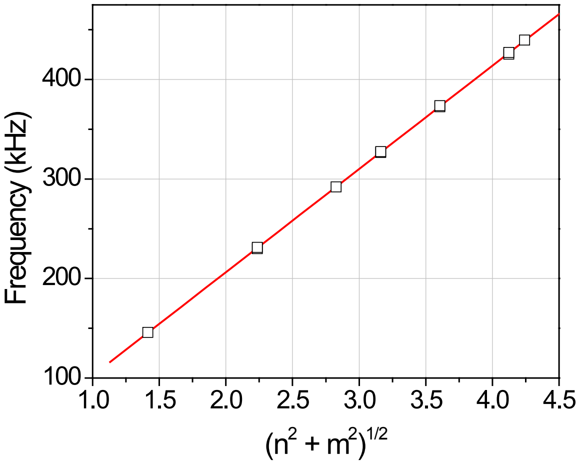

Figure 3·6: Measured mode frequencies of a membrane resonator (device $M1$) as a function of mode numbers n and m. The frequencies depend linearly on $(n^2 + m^2)^{1/2}$

device $M1$ in Figure 3·7. We are able to fit all measured modes of the device with the gas damping theory and we find ρh to be 1.83×10^{-3} kg/m^2 for the first mode and 1.64×10^{-3} kg/m^2 for the next four measured modes. These compare favorably (within 15%) to the value calculated using the thickness from the ellipsometer measurement and the material density ($\rho h = 1.94 \times 10^{-3}$ kg/m^2). We present all of our results in Table 3.2 below.

3.4 Results and Discussion

We have conducted thermal noise measurements and gas damping measurements on all of the devices listed in Table 3.1. We can compare the results of these two measurements to eachother and to manufacturer estimates. Our results are summarized in Table 3.2. The first and second columns in the table list the device and the frequency of the mechanical mode. The third column is an estimate of ρh obtained from manufacturer specifications of h (ellipsometry in the case of $M1$) and the density of the material. The fourth and fifth columns are estimates of ρh obtained from the gas dissipation and thermal noise measurements, respectively. These values are found by

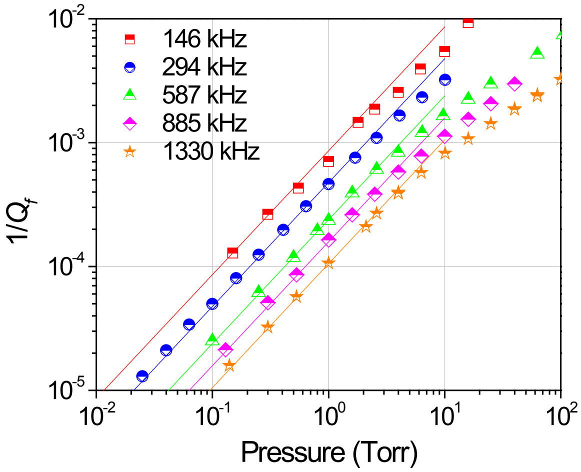

Figure 3·7: Measured fluidic dissipation $1/Q_f$ as a function of pressure p for five mechanical modes of device $M1$.

fitting our data using Eq. (3.14) and Eq. (3.4) for the two cases as described above.

In the case of the cantilever devices, the data show good agreement with an average error of 5.7% between results from the gas damping method and the thermal noise method. The results also correspond closely with the estimates from manufacturer specifications. In the case of the membrane ($M1$) the agreement is not satisfactory and we do not have a complete data set for the thermal noise measurements. In fact, thermal measurements could only be made on the 146.0 and 294.3 kHz modes because the thermal displacements of the higher modes were below the noise floor of the measurement system. There are some experimental difficulties that must be addressed to improve this measurement including reducing the spot size and increasing the stability of the optical measurement system. It is encouraging, however, that the membrane gas damping results give an estimate of ρh that is within 15% of the value calculated using the material properties of the membrane. Assuming the density of SiN to be $\rho_{\mathrm{SiN}} \approx 3440$ kg/m^3, we arrive at an estimate of the membrane thickness h between 480 and 530 nm, very close to the number determined from ellipsometry (563 nm).

Device	Frequency $\omega_0/2\pi$ (kHz)	Geometric ρh (kg/m^2)	Gas Damping ρh (kg/m^2)	Equipartition ρh (kg/m^2)
$C1$	221.4	4.66×10^{-3}	4.68×10^{-3}	4.6×10^{-3}
$C1$	1360.4	4.66×10^{-3}	4.68×10^{-3}	4.89×10^{-3}
$C2$	150	2.33×10^{-3}	3.22×10^{-3}	3.22×10^{-3}
$C2$	925	2.33×10^{-3}	3.22×10^{-3}	3.52×10^{-3}
$C3$	224	2.33×10^{-3}	3.42×10^{-3}	3.35×10^{-3}
$C3$	1358	2.33×10^{-3}	3.42×10^{-3}	3.68×10^{-3}
$C4$	110	2.33×10^{-3}	4.26×10^{-3}	3.28×10^{-3}
$C4$	676	2.33×10^{-3}	3.08×10^{-3}	3.05×10^{-3}
$C4$	1866	2.33×10^{-3}	3.08×10^{-3}	3.16×10^{-3}
$M1$	146.0	1.94×10^{-3}	1.83×10^{-3}	2.7×10^{-3}
$M1$	294.3	1.94×10^{-3}	1.64×10^{-3}	5.8×10^{-3}
$M1$	587.0	1.94×10^{-3}	1.64×10^{-3}	–
$M1$	884.6	1.94×10^{-3}	1.64×10^{-3}	–
$M1$	1330.1	1.94×10^{-3}	1.64×10^{-3}	–

Table 3.2: Results of measurements of ρh determined by multiple methods.

In this chapter we have presented multiple methods which can be used to estimate modal mass in mechanical systems and we have performed experiments to test these methods. In the gas damping method we measured the energy dissipated (quality factor) by a mechanical oscillator at various pressures in order to extract the mass. In the thermal noise method we measured the thermal fluctuations of an oscillator and related its modal energy to the modal mass. While this method is accurate, it requires the used of a well-calibrated and very sensitive measurement system that can reliably detect thermal fluctuations of the device under test. We have shown here that the gas dissipation method provides accurate results and that it can provide a suitable alternative to the thermal calibration method. Because it relies on the driven system response, rather than thermomechanical motion, the device fluctuations are orders of magnitude larger in the gas dissipation method and the measurements are easier to conduct. Additionally, the gas dissipation method does not require the determination of the absolute device deflection; only a reliable measurement of the quality factor is necessary.

Chapter 4

Crossover from Hydrodynamics to the Kinetic Regime in Confined Nanoflows

In this chapter, we present an experimental study of a spatially confined nanoflow, which is generated by a sphere attached to the end of a microcantilever, oscillating in the proximity of a flat solid wall. In this case, the symmetry of the problem is broken and the physical behavior of the flow is quite different than in the case of an unbounded oscillatory flow. As the cantilever is brought towards the wall, the flow becomes confined in the gap between the cantilever and the wall, affecting the resonant frequency and dissipation of the cantilever. By carefully tuning the separation distance, the gas pressure (the fluid mean free path), and the cantilever oscillation frequency, we study the flow over a broad range of dimensionless parameters. We observe deviations from continuum fluid dynamics at small gaps, low pressures, and high frequencies. Using these measurements, we provide an in-depth characterization of confinement effects in oscillating nanoflows. In addition, we construct a scaling function which describes the flow in the entire parameter space, including both the hydrodynamic and the kinetic regimes. Our scaling function unifies previous theories based on the slip boundary condition and the effective viscosity. This work was published in *Physical Review Letters* (Lissandrello et al., 2012).

4.1 Background

As we have seen in Chapter 3, in micron and nanometer scale flows (Karniadakis et al., 2005; Tabeling, 2005), the characteristic dynamic length scale $\mathcal{L}$ of the flow approaches and is even exceeded by the mean free path of the fluid λ. This limit is clearly beyond the applicability of the Navier-Stokes equations, requiring a rigorous treatment using kinetic theory. A less rigorous but widely used approach to describe these small scale flows is to extend the Newtonian description by imposing a slip boundary condition on solid walls. This approach is justified as follows. Derivation of the Navier-Stokes equations from kinetic theory results in the appearance of a Knudsen layer of thickness λ near the wall (Lifshitz and Pitaevskii, 1981). Because a fluid element of linear dimension $\sim \lambda$ is treated as a mathematical point in the hydrodynamic approximation, the velocity at the wall becomes $u_w \approx \lambda \frac{du}{dz}\big|_{z=0}$, with u being the hydrodynamic velocity (assumed parallel to the wall) and $\hat{\mathbf{z}}$ being the wall normal. Thus, the slip length b, where $b \sim \lambda$, is applied as a convenient empirical parameter to extend the Navier-Stokes equations into the kinetic regime. As required by macroscopic hydrodynamics, b becomes negligible when the Knudsen number, $\mathrm{Kn} \equiv \frac{\lambda}{\mathcal{L}}$, is small, i.e., $\mathrm{Kn} \ll 1$.

The above approach comes with some problems. To describe some gas flows, for instance, unphysical slip lengths, $b \gg \lambda$, may be required. To alleviate this problem, one can assume specular reflections of the gas molecules from the wall. However, experiments show that this assumption is not very accurate for heavier gases and untreated surfaces (Arkilic et al., 2001; Trott et al., 2011). Worse is the problem when the Navier-Stokes solution (with the slip boundary condition) fails to converge with the prediction of the kinetic theory. A good example of this is oscillating nanoflows (Karabacak et al., 2007; Ekinci et al., 2008; Ekinci et al., 2010; Svitelskiy et al., 2009; Lee et al., 2011). Efforts to describe oscillating nanoflows using the Navier-Stokes equations in conjunction with a slip length agree with experiments only in a limited range of relevant parameters (Bhiladvala and Wang, 2004). A proper kinetic treatment of the problem (Yakhot and Colosqui, 2007) illustrates why: the finite relaxation time τ of the fluid modifies the physics of the flow, resulting in the "telegrapher's equation," which is substantially different from the Navier-Stokes equations.

Until now our discussion has been primarily focused on unbounded oscillatory flows in both the hydrodynamic and the kinetic regime. In this section, we turn our attention to nanometer scale confined flows in the limit $h \lesssim \lambda$, where h is the confining length scale. To date, a group of researchers have extended Reynolds' hydrodynamic formulation (Reynolds, 1886; Vinogradova, 1995) to small scales by imposing the slip boundary condition (Honig et al., 2010; Bowles and Ducker, 2011; Maali and Bhushan, 2008; Laurent et al., 2011; Ramanathan et al., 2010; Veijola et al., 1998) — as described above. Others, coming from kinetic theory, have developed the concept of the effective viscosity, which typically depends upon a properly defined Knudsen number (Bao et al., 2002). There is no question that both approaches must agree for the same flow parameter space. Here, we present an experimental study of nanometer scale confined flows covering a broad range of parameters — including gap h, pressure p, and frequency $\frac{\omega}{2\pi}$ — along with a scaling theory. Our scaling function describes the physical behavior of the flow in the entire parameter space, accurately capturing the transition from hydrodynamics to the kinetic regime.

4.2 Experimental Setup

We study the oscillatory hydrodynamic response of a sphere in the proximity of a solid surface. Our experimental device is a micron-scale silica sphere with radius R glued to the end of a microcantilever of linear dimensions $l \times w \times t$. An image of

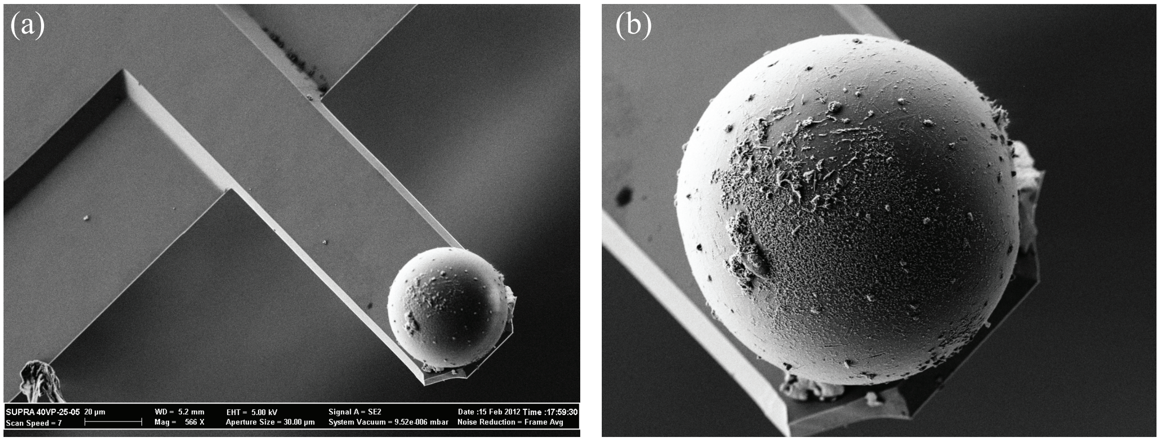
(a)
(b)
SUPRA 40VP-25-05 20 µm
Scan Speed = 7
WD = 5.2 mm
Mag = 566 X
EHT = 5.00 kV
Aperture Size = 30.00 µm
Signal A = SE2
System Vacuum = 9.52e-006 mbar
Date :15 Feb 2012 Time :17:59:30
Noise Reduction = Frame Avg

Figure 4·1: Silver-coated silica sphere adhered to a silicon microcantilever. (a) SEM image of the cantilever with sphere attached. Scale bar is 20 μm. (b) Close-up SEM image of the sphere with $R \approx 20$ μm.

one of the devices, taken with a scanning electron microscope (SEM), is shown in Figure 4·1. The sphere is connected to the cantilever by using a precise stage to dip the cantilever tip in epoxy and then to make contact with the sphere. The sphere-cantilever apparatus is then heated on a hot plate to cure the epoxy. The optical beam deflection technique, common in atomic force microscopy (AFM) (Meyer and Amer, 1988) and as described in Chapter 2, is used to measure the fluctuations of the microcantilever. In this study, we have employed both the fundamental and first harmonic flexural modes of a soft cantilever (C1), and the fundamental flexural mode of a shorter, stiffer cantilever (C2). Figure 4·2 depicts optical measurements and finite element method (FEM) simulations (run in COMSOL Multiphysics) of the mechanical modeshapes of C1. For each device and mode, we first extract the the intrinsic quality factor Q_i and resonance frequency $\frac{\omega_i}{2\pi}$ in ultra-high vacuum (UHV) away from any surfaces. The modal mass m_e is determined from the resonance frequency shifts before and after the sphere is attached to the cantilever. These parameters are listed in Table 4.1.

Once the mechanical mode is characterized, we change the flow parameters while

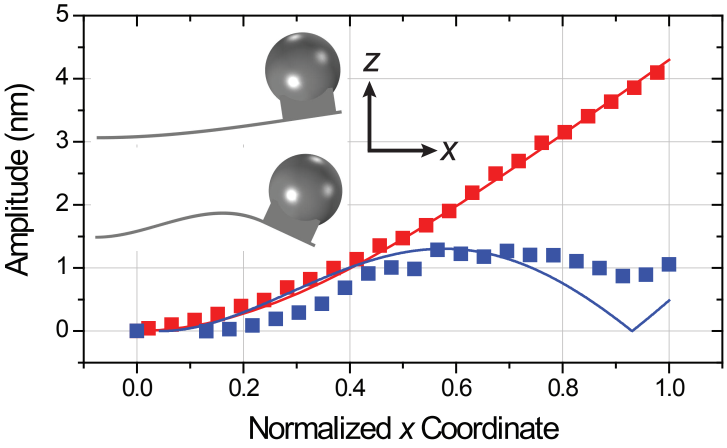

Figure 4·2: Measured (symbols) and simulated (inset and solid lines) mechanical modes of the sphere-cantilever device. In the first harmonic mode (blue), FEM simulations suggest that the node appears at the position where the sphere is attached to the cantilever and that the sphere undergoes small rotational oscillations about an axis (parallel to the y-axis) through the node.

optically monitoring the dissipation and the resonance frequency of the mode. In particular, we continuously vary two parameters for each mode as follows. i) We change the gap h (shortest distance) between the sphere and a flat solid (Silicon) surface. At small gaps ($h \leq 200$ nm), we drive the cantilever to achieve 'intermittent contact' between the sphere and the solid, and determine the gap from the amplitude. For large gaps, h is extracted from a calibrated linear motion stage. ii) We vary the surrounding pressure p by admitting dry N_2 into the chamber. These provide a two-dimensional parametric map of the dimensionless dissipation and the (angular)

Device	Mode	$l \times w \times t$ (μm^3)	R (μm)	$\frac{\omega_i}{2\pi}$ (kHz)	Q_i	m_e (kg)
C1	1	$230 \times 40 \times 3$	35	13.7	$12{\times}10^3$	$5{\times}10^{-10}$
C1	2	$230 \times 40 \times 3$	35	45.8	$3.4{\times}10^3$	$16{\times}10^{-10}$
C2	1	$125 \times 35 \times 4$	21.5	122.4	$6.8{\times}10^3$	$1{\times}10^{-10}$

Table 4.1: Parameters of devices measured in this study.

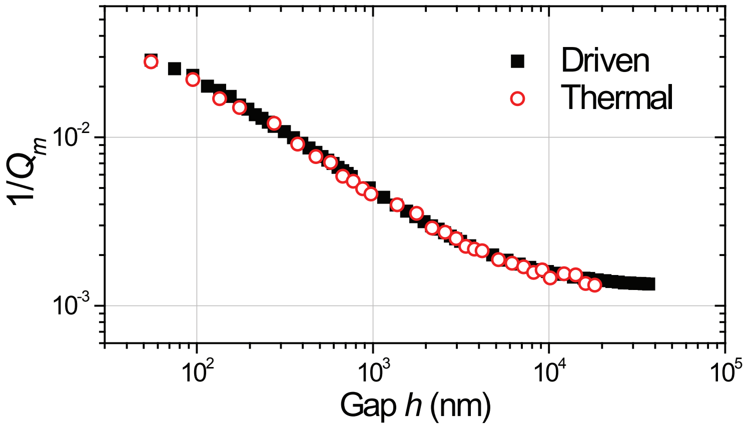

Figure 4·3: Measured dimensionless dissipation $1/Q_m$ as a function of gap h, obtained from the driven frequency response and thermal oscillations of the device.

resonance frequency: ${Q_m}^{-1} = {Q_m}^{-1}(h, p)$ and $\omega_m = \omega_m(h, p)$. Before presenting the data, we show in Fig. 4·3 that $1/Q_m$ measured by linearly driving the resonator and by monitoring its thermal fluctuations agree closely, with a typical discrepancy less than 1%. The maximum amplitudes in driven and thermal measurements remain ~ 1 nm and ~ 0.01 nm, respectively.

4.3 Results and Discussion

The dissipation of the resonator measured in an experiment, $1/Q_m$, is in fact a combination of the fluidic dissipation, intrinsic dissipation, and any other dissipative sources that may be present in the system. By properly subtracting the intrinsic dissipation from the measured dissipation, one can obtain the fluidic dissipation:

$$\frac{1}{Q_f} = \frac{1}{Q_m} - \frac{1}{Q_i}. \tag{4.1}$$

Figure 4·4(a) and (b) show the ${Q_f}^{-1} = {Q_f}^{-1}(h, p)$ data set for the 13.7 kHz mode in double-logarithmic plots against gap h and pressure p, respectively. In Fig. 4·4(a), the

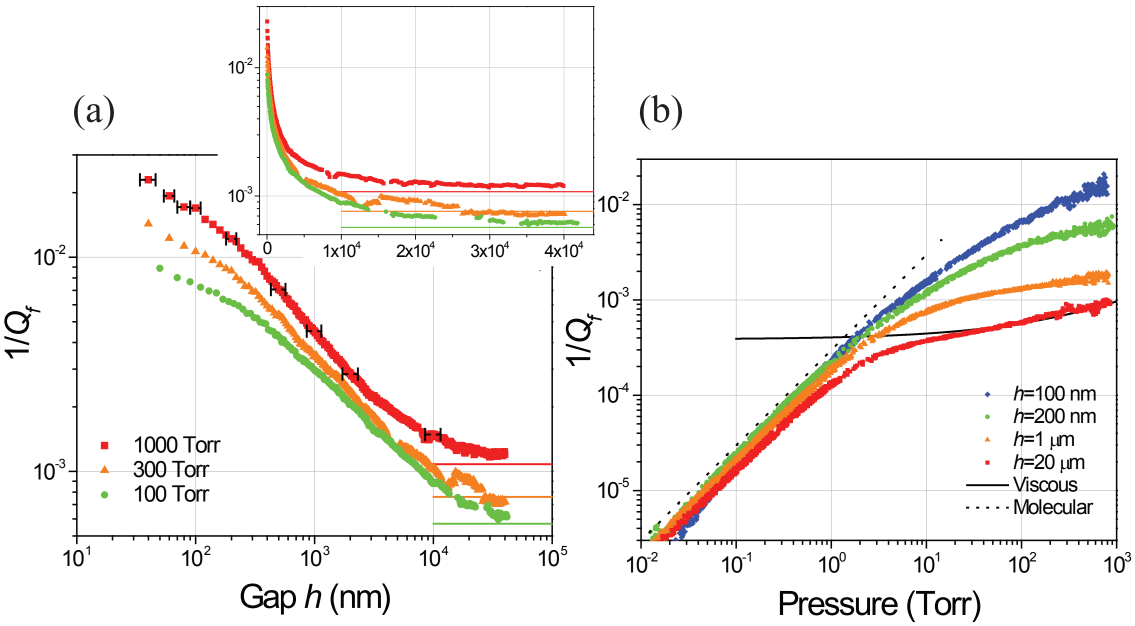

Figure 4·4: (a) Dimensionless fluidic dissipation $1/Q_f$ as a function of gap h at fixed pressures p. Solid line segments show asymptotic values $1/Q_{f\infty}$ from viscous theory. Inset is a semi-logarithmic plot of the same data. The h error bars for $h \leq 200$ nm are due to roughness and contact uncertainty. Otherwise, the error comes from the linear stage. The error bars in $1/Q_f$ are smaller than the symbol sizes. (b) $1/Q_f$ measured as a function of pressure p with the gap fixed. Solid line is from viscous theory and the dotted line is from molecular theory. All data in this figure are obtained from device C1.

gap is varied in the range 10^{-8} m $\leq h \leq 10^{-4}$ m with the pressure held at $p = 100, 300$ and 1000 Torr. Conversely, in Fig. 4·4(b), the pressure is swept continuously in the range 10^{-2} Torr $\leq p \leq 10^3$ Torr, while the gap is fixed at $h = 0.1, 0.2, 1$ and 20 μm. The inset in Fig. 4·4(a) is a semi-logarithmic plot, showing the characteristic saturation of ${Q_f}^{-1}$ vs. h (see discussion on $1/Q_{f\infty}$ below). The accompanying mode frequency, $\omega_m = \omega_m(h,p)$, show very little variation (less than 0.1%) in this parameter space.

Several important preliminary observations can be made from the data of Fig. 4·4. As we have seen in Chapter 3, for a sphere oscillating at frequency $\frac{\omega}{2\pi}$ in an unbounded fluid at the viscous limit $\omega\tau \ll 1$ (Yakhot and Colosqui, 2007; Karabacak et al., 2007; Ekinci et al., 2008; Ekinci et al., 2010), the dimensionless dissipation can be written as (Landau and Lifshitz, 1987)

$$\frac{1}{Q_{f\infty}} = \frac{6\pi\mu R}{m\omega}\left(1+\frac{R}{\delta}\right), \tag{4.2}$$

where R is the radius and m is the mass of the sphere, μ is the dynamic viscosity of the fluid, and $\delta = \sqrt{\frac{2\mu}{\rho\omega}}$ is the viscous boundary layer thickness. The fluidic dissipation from the rectangular cantilever can also be found, albeit numerically (Sader et al., 1999). The solid line segments in Fig. 4·4(a) and the solid curve in Fig. 4·4(b) show the $1/Q_{f\infty}$ predictions of viscous theory at large gaps, $h \to \infty$. In these calculations, the independent contributions to dissipation from the sphere and the cantilever are simply added. The velocity field of an oscillating sphere-cantilever system should be different from that obtained by adding the individual velocity fields of a sphere and a cantilever. Regardless, the agreement between experiment and calculations in Fig 4·4 is satisfactory. For the 13.7 kHz and 122 kHz modes, the ratio of the measured and calculated $1/Q_{f\infty}$ agree closely, with an error $\lesssim 15\%$. For the 45.8 kHz mode, the measured $1/Q_{f\infty}$ is a factor of 4 larger than the calculated value. This is possibly due to the more complex motion of the sphere. In Fig. 4·4 (b), the prediction of molecular theory (Bhiladvala and Wang, 2004) is also shown.

When a wall is placed in the proximity of an oscillating sphere, the entire velocity field (not just the field in the gap) will be modified substantially. Regardless, the dissipation caused by the squeezing of fluid in the gap can be conveniently studied by subtracting the dissipation in an infinite fluid, i.e., $1/Q_h = 1/Q_f - 1/Q_{f\infty}$. Subtracting the *experimental* h-independent $1/Q_{f\infty}$ asymptotes in Fig. 4·4(a) from the $1/Q_f$ data results in the dimensionless gap-dependent dissipation $1/Q_h$ in Fig. 4·5(a). Figure 4·5 depicts similarly-obtained $1/Q_h$ for three different modes at multiple pressures

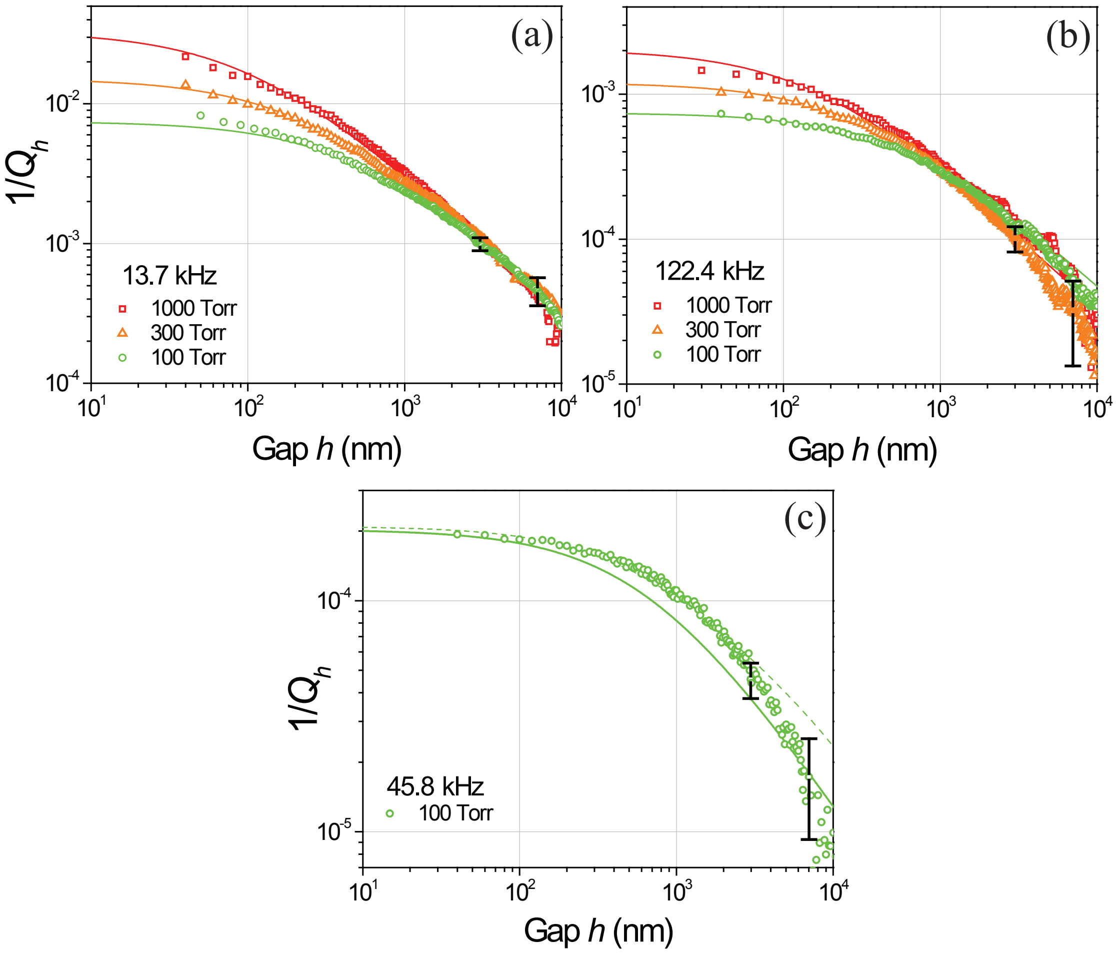

Figure 4·5: Gap dependent dimensionless dissipation $1/Q_h$ as a function of gap h at fixed pressure. (a), (b) Fundamental modes of devices C1 and C2, respectively. (c) First harmonic mode of device C1. Solid lines in (a)-(c) are fits to Eq. (4.8) with $\alpha = 0.5$ and $\beta = 1.6$, multiplied by a fitting factor of $\mathcal{C} \approx 0.23 \pm 0.11$. The deviation from the solid line in (c) is possibly due to the additional rotational motion of the sphere. The dashed line in (c) is the improved fit with the added rotational dissipation (Kim and Karrila, 1991). The noise in all the data in (a)-(c) increases for $h \geq 10^4$ nm due to the subtraction of $1/Q_{f\infty}$. The representative error bars are found by an analysis of the noise at the tails ($h \geq 10^4$ nm) and become smaller than symbols for $h \lesssim 10^3$ nm.

as the gap is varied. Solid lines are fits to theory (see below). A first pass analysis of the data can be provided based upon the dimensionless Knudsen number, $\mathrm{Kn}_h \equiv \frac{\lambda}{h}$. When $\mathrm{Kn}_h \ll 1$, $1/Q_h \propto 1/h$ and can be approximated as (Brenner, 1961; Kim and Karrila, 1991; Chadwick and Liao, 2008):

$$\frac{1}{Q_h} = \frac{6\pi\mu R}{m\omega} \times \frac{R}{h}. \tag{4.3}$$

At the opposite limit of $\mathrm{Kn}_h \gg 1$, the dimensionless dissipation saturates. Between these two limits, there is a well-defined transition from the hydrodynamic to the kinetic regime.

4.3.1 Scaling Theory

We now provide a theoretical background for the observed transition. Since $1/Q_h \to 0$ as $h \to \infty$, we can write a general relation

$$\frac{1}{Q_h} = \frac{6\pi\mu R}{m\omega} \times \frac{R}{h} \times f\left(\frac{\lambda}{h}, \frac{\lambda}{\delta}, \frac{\lambda}{R}, ..., \frac{R}{\delta}\right). \tag{4.4}$$

The scaling function $f(\{x_i\})$, which is analytic in the limit $\{x_i\} \to 0$, depends on various dimensionless variables pertaining to different dynamic regimes. It is clear that the first few $\{x_i\}$ are the familiar Knudsen numbers based on appropriate linear dimensions characterizing the system: $\mathrm{Kn}_h = \frac{\lambda}{h}$, $\mathrm{Kn}_\delta = \frac{\lambda}{\delta}$, $\mathrm{Kn}_R = \frac{\lambda}{R}$ and so on. The last dimensionless variable, $\frac{R}{\delta} = R\sqrt{\frac{\omega}{2\nu}} = \sqrt{\frac{UR}{\nu}} = \mathrm{Re}_\delta$, can be regarded as a Reynolds number based on the velocity $U = \omega R/2$. In the limit $\mathrm{Kn}_i \to 0$ and $\mathrm{Re}_\delta \to 0$, Taylor expansion gives

$$\frac{1}{Q_h} = \frac{6\pi\mu R}{m\omega} \times \frac{R}{h} \times \left(1 + f^{(1)} + f^{(2)} + ...\right), \tag{4.5}$$

where

$$f^{(1)} = a_h^{(1)}\mathrm{Kn}_h + a_\delta^{(1)}\mathrm{Kn}_\delta + ... + a_{\mathrm{Re}}^{(1)}\mathrm{Re}_\delta \tag{4.6}$$

$$\begin{aligned} f^{(2)} = & \, a_h^{(2)}\mathrm{Kn_h}^2 + a_\delta^{(2)}\mathrm{Kn}_\delta{}^2 + ... + a_{\mathrm{Re}}^{(2)}\mathrm{Re}_\delta{}^2 \\ & + a_{h,\delta}^{(2)}\mathrm{Kn}_h\mathrm{Kn}_\delta + a_{h,\mathrm{Re}}^{(2)}\mathrm{Kn}_h\mathrm{Re}_\delta + ... \end{aligned} \tag{4.7}$$

The relative magnitudes of the $a_i^{(n)}$ and the dimensionless parameters $\{x_i\}$ determine the physics of the flow. By varying $\{x_i\}$ over a broad range, one can extract the magnitudes of $a_i^{(n)}$ from experiment.

To gain more insight into the proposed expansion in Eq. (4.5), let us consider the limits. When $h \to \infty$ ($\mathrm{Kn}_h \to 0$), dimensionless dissipation due to squeezing disappears, $1/Q_h \to 0$. This suggests that the first order term in the Taylor expansion in Eq. (4.6) should not strongly depend on the other Knudsen numbers, Kn_δ, Kn_R and so on. In the limit of small h ($\mathrm{Kn}_h \gg 1$), momentum transfer is dominated by the ballistic impact of the molecules emitted from the stationary plate incident on the moving sphere. The contribution of intermolecular collisions can be neglected. If the thermal molecular velocity u_{th} is large, the dimension of the gap h must disappear from the expression for dissipation.

Keeping a finite number of terms in Eq. (4.5), one can only hope to find an approximation for the scaling function $f(\{x_i\})$ valid in the limit $x_i \to 0$. To obtain an expression valid in the entire range of $\{x_i\}$ variation, one has to keep infinitely many terms. This can be achieved by recasting the scaling function in Eq. (4.4) into a ratio of low-order polynomials with unknown coefficients to be determined experimentally. The resulting expression

$$\frac{1}{Q_h} = \frac{6\pi\mu R}{m\omega} \times \frac{R}{h} \times \frac{1}{1 + \alpha\frac{\lambda}{h}\left(1 + \beta\frac{R}{\delta}\right)} \tag{4.8}$$

can be perceived as the simplest Padé approximant, which should describe experiments in a broad parameter range. The constants α and β are related to $a_i^{(n)}$. It is interesting to note that, in this choice, the term of linear order $\mathcal{O}(\mathrm{Re}_\delta)$ disappears due to the subtraction, $1/Q_h = 1/Q_f - 1/Q_{f\infty}$. However, the higher order term $\mathcal{O}(\mathrm{Kn}_h \mathrm{Re}_\delta)$ survives. In the small-gap limit $\mathrm{Kn}_h = \frac{\lambda}{h} \gg 1$, one obtains as prescribed

$$\frac{1}{Q_h} \sim \frac{6\pi\rho u_{th} R^2}{m\omega\alpha\left(1+\beta\frac{R}{\delta}\right)}. \tag{4.9}$$

Returning to Fig. 4·5, we now describe how the fits to the experimental data are obtained based upon the above scaling form. The device parameters $m = m_e$, ω, and R are experimental constants. The fluid parameters are all assumed to be independent of h, but may depend on p: $\lambda \propto p^{-1}$, $\delta \propto p^{-1/2}$, and μ is independent of p. The very *same* constants α and β in the scaling function in Eq. (4.8) must uniquely fit *all* data sets — regardless of pressure, frequency, mode and so on. Indeed, we can fit *all* our data with $\alpha = 0.5$ and $\beta = 1.6$, found by iteration. Any small changes in α and β cause the curves in Fig. 4·5 to shift along the h-axis, making the fits unacceptable. The fits can be improved along the $1/Q_h$-axis by multiplying with fitting factors of $\mathcal{C} \approx 0.33,\ 0.20$ and 0.16 for the 13.7 kHz, 122.4 kHz and the 45.8 kHz modes, respectively, resulting in the solid curves in Fig. 4·5. To within our experimental accuracy, however, $\mathcal{C}$ remains a constant as $\mathcal{C} \approx 0.23 \pm 0.11$ for all our devices, and may be needed due to non-idealities in geometry (e.g., the cantilever and epoxy above the sphere), inaccuracies in determining m_e (especially for the first harmonic mode) and deviations from normal relative motion (see below). Deeper physical factors — such as the non-trivial effects of the subtraction of the $1/Q_{f\infty}$ tails and unsteady corrections to Eq. (4.3)— cannot be ruled out, and may give rise to the small deviations in $\mathcal{C}$ from device to device.

The fit in Fig. 4·5(c) (solid curve) deviates from the data for 10^2 nm $\lesssim h \lesssim 5 \times 10^4$ nm. FEM simulations for this mode suggest that the sphere undergoes rotational motion — with the displacement of its closest point to the wall being in the direction $0.98\hat{\mathbf{x}} + 0.2\hat{\mathbf{z}}$ (see Fig. 4·4(a)). Then, the dissipation comes from shearing the fluid

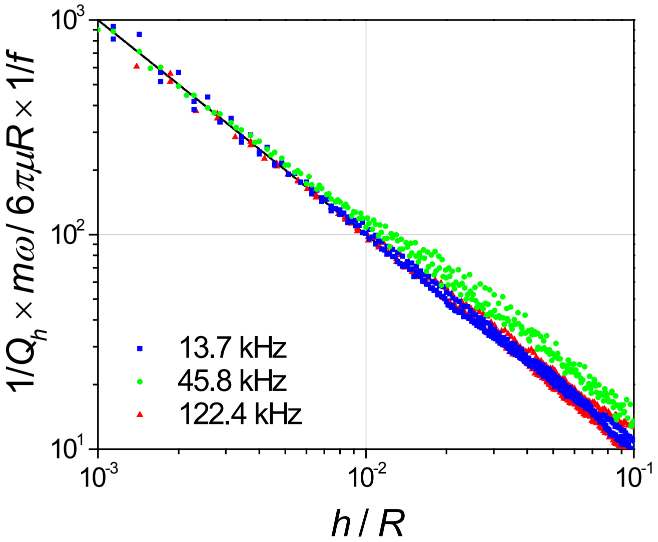

Figure 4·6: Collapse of all experimental data from this work. Here, f is the scaling function defined in Eq. (4.8) and the same $\mathcal{C}$s are used as above.

in the gap as well as from squeezing it. For shear, $\frac{1}{Q_h} = \frac{48\pi\mu R}{15m\omega} \times \ln\left(\frac{R}{h}\right)$ (Kim and Karrila, 1991) as opposed to the expression in Eq. (4.3) for squeezing. The dashed line in Fig. 4·5(c) is the fit found by naïvely adding these two forms in the ratio of the FEM motional amplitudes, and by keeping the scaling function exactly the same. Because the effect remains small, the $1/h$ dependence of the dissipation can be assumed prevalent for all devices considered here and in the literature.

4.3.2 Collapse of Data

Having fit individual data traces, we can collapse all our data as shown in Fig. 4·6. The collapse is obtained by removing the trivial effects of the device size and frequency from the data as well as the more profound effects of the scaling function $f(\{x_i\})$. The plotted dimensionless quantity, $\frac{1}{Q_h} \times \frac{m\omega}{6\pi\mu R} \times \frac{1}{f}$ can be regarded as the dimensionless size- and frequency-independent dissipation, in which the kinetic effects have been deconvoluted. It therefore shows the hydrodynamic R/h dependence at all length scales studied here.

Finally, our results can be interpreted as follows. In the hydrodynamic limit ($h \gg \lambda$), this problem is described by Eq. (4.3), where the viscosity μ is dominated by intermolecular collisions, $\mu \sim \rho u_{th} \lambda$, with a relaxation timescale $\sim \lambda / u_{th}$. To gain insight into the kinetic limit ($h \ll \lambda$), one can simply write the shear stress on the sphere as $\sigma \sim \rho u_{th} \left| \dot{h} \right|$. It is easy to see that $\sigma \sim \rho u_{th} h \frac{|\dot{h}|}{h} \sim \rho u_{th} h \frac{du}{dz}$, where $\frac{du}{dz}$ is the velocity gradient. This result can be interpreted as the appearance of an effective viscosity, $\mu_{eff} \approx \rho u_{th} h$, due to an effective mean free path, $\lambda_{eff} \approx h$. Substituting μ_{eff} into the hydrodynamic solution simply results in $\frac{1}{Q_h} \sim \frac{\rho u_{th} R^2}{m\omega}$, consistent with Eq. (4.9). Thus, in principle, one may justify an attempt to reach the kinetic regime by using the Navier-Stokes equations, but combined with effective (and sometimes frequency-dependent) viscosities, slip lengths and so on.

In this chapter, we have presented experimental data on confined nanoflows covering a broad range of flow parameters. Our simple scaling theory describes experiments in the entire parameter range — without explicitly employing an effective viscosity and/or slip length. In all cases the Weissenberg numbers remain small, $\mathrm{Wi} = \omega\tau \ll 1$. Since the appearance of frequency in effective viscosity essentially leads to a modification of the equations of motion (Karabacak et al., 2007; Ekinci et al., 2008; Ekinci et al., 2010; Yakhot and Colosqui, 2007), generalization of confined nanoflows to the interval $\mathrm{Wi} \gg 1$ will require further experimental and theoretical work.

Chapter 5

Nanomechanical Motion of ***Escherichia coli*** Adhered to a Surface

In this chapter we turn to an experimental study of a biologically driven flow. We study the nanomechanical motion of bacteria adhered to a chemically functionalized silicon microcantilever by conducting measurements of the cantilever's fluctuations. A non-specific binding agent is used to attach *Escherichia coli* (*E. coli*) to the surface of the microcantilever. The microcantilever is kept in a liquid medium, and its nanomechanical fluctuations are monitored using an optical displacement transducer. The motion of the bacteria couples efficiently to the microcantilever well below its resonance frequency, causing a measurable increase in the microcantilever fluctuations. In the time domain, the fluctuations exhibit large-amplitude low-frequency oscillations. In corresponding frequency-domain measurements, it is observed that the mechanical energy is focused at low frequencies with a $1/f^{\alpha}$-type power law. A basic physical model is used to explain the observed spectral distribution of the mechanical energy. These results lay the groundwork for understanding the motion of microorganisms adhered to surfaces and for developing micromechanical sensors for bacteria. The results presented here were published in *Applied Physics Letters* (Lissandrello et al., 2014).

5.1 Background and Motivation

Antimicrobial resistance (AMR) has become an increasingly serious threat to global public health. Resistant strains of microbes, including bacteria and viruses, develop naturally when resistant traits randomly evolve. In the case of bacterial resistance to antibiotics, this evolution has been shown to predate the selective pressure of modern-day antibiotic use (D'Costa et al., 2011). Despite this, the overuse and misuse of antimicrobial drugs has exacerbated the problem by creating an environment which is very conducive for the reproduction of these resistant microbes. Their pervasiveness has reduced the effectiveness of treatment resulting in prolonged illness, higher health care expenditures, and a greater risk of death (World Health Organization, 2014). The World Health Organization estimates that the annual economic effect of AMR on the US health system could be as large as $34 billion. There is thus a need for rapid and accurate methods for bacterial detection and identification. Conventional techniques, such as polymerase chain reaction or agar plate culture, require complex steps, expensive infrastructure, and skilled technicians, which make their implementation in primary care settings challenging. Furthermore, these assays are time-consuming (e.g., 48-72 hours for agar plate culture) and rely on multiple sample processing steps. Here, we propose a new approach which exploits the motile nature of some bacteria in order to rapidly detect their presence and to perform subsequent tests of antibiotic efficacy.

Biological function in motile microorganisms is intimately coupled to mechanical motion (Pelling et al., 2004; Arnoldi et al., 2000; Zhang et al., 2001; Jiang et al., 2003), which is generated and sustained by a vast array of forces. Conversely, motile microorganisms exert forces on their surroundings as a result of their incessant motion and metabolism (Bao and Suresh, 2003). A deeper physical understanding of biological processes in terms of these nanomechanical forces and motions is of value

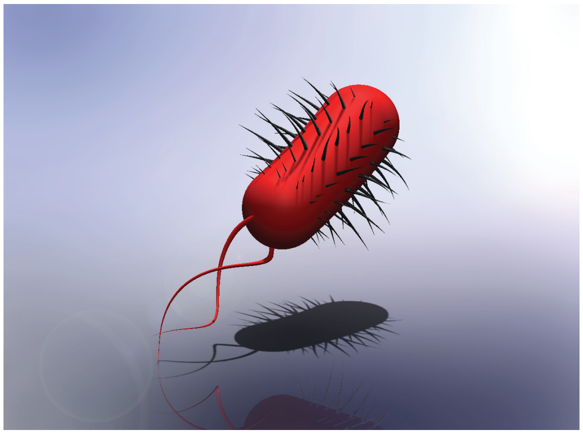

Figure 5·1: Illustration of a motile *E. coli* bacterium. The bacterium is approximately 2 μm long with a rod-shaped body, many cilia, and a few flagella which are used for propulsion.

for both fundamental science and clinical medicine (Frauenfelder et al., 1999). For instance, bacterial communication through motion is believed to be an important factor for infections and for bacterial resistance to antibiotics (Visick and Fuqua, 2005; Callegan et al., 2005; Wang et al., 2013). Consequently, the development of sensitive force and motion probes (Moffitt et al., 2008), which can match the time and length scales of microorganisms, has been an important element in the study of motile microorganisms.

The microcantilever has been one of the mainstays for probing the forces and motions of biological entities (Lavrik et al., 2004; Ekinci and Roukes, 2005). Early microcantilever-based experiments were extensions of AFM. For instance, the AFM tip scanned over biomolecules adsorbed on a surface provided information on the conformational changes of the biomolecules (Radmacher et al., 1994; Thomson et al., 1996). Similarly, nanomechanical motion and forces of microorganisms, such as *Saccharomyces cerevisiae* (Pelling et al., 2004) and bacteria, were investigated using contact-mode or dynamic-mode AFM under a number of different biological conditions. More recently, biological entities have been attached to bio-chemically function-

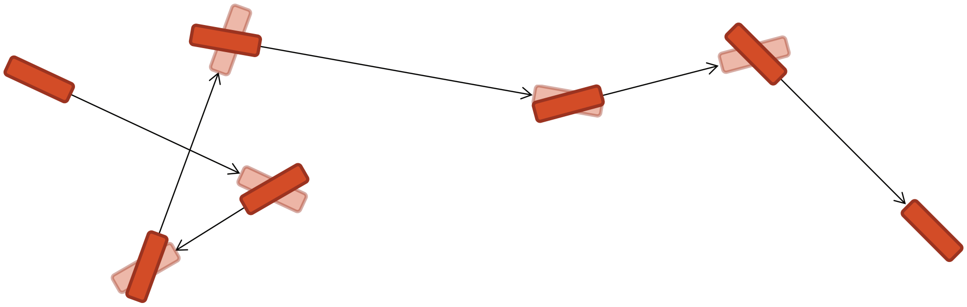

Figure 5·2: An *E. coli* bacterium propels itself by rotating its flagella. The locomotion follows a running and tumbling pattern with periods during which the bacterium “swims” in a straight line and periods during which it rotates in place.

alized microcantilevers in an effort to develop novel sensors. These micromechanical biosensors, which are typically integrated with microfluidics, utilize both the static deflection and the resonance frequency shift of the cantilever (Ramos et al., 2006; Burg et al., 2007). In static and resonant sensing modalities, microcantilevers have allowed for the sensing of diverse biological entities, ranging from DNA to proteins to microorganisms (Arlett et al., 2011; Wu et al., 2001; Gfeller et al., 2005) (e.g., viruses and bacteria). In more recent work, Longo and co-workers (Kasas et al., 2015; Longo and Kasas, 2014; Longo et al., 2013) adhered bacteria to a microcantilever, and measured the nanomechanical fluctuations of the cantilever before and after adhesion. With the bacteria present on the cantilever, the fluctuations increased significantly. Based on these results, a rapid detection scheme for bacterial antibiotic resistance was proposed.

The above-mentioned studies clearly demonstrate that small mechanical devices are capable of measuring signals from biological entities, given the attainable force sensitivities and response times. In this chapter, we apply the microcantilever-based technique developed by Longo et al. (Kasas et al., 2015; Longo and Kasas, 2014; Longo et al., 2013) to measurements of the nature (e.g., time scales and amplitudes) of the forces that bacteria exert on the microcantilever. In our measurements we use a motile type of *E. coli* bacteria (illustration in Figure 5·1) which have rod-shaped bodies approximately 2 μm in length, many cilia, and a small cluster of flagella at one end which are used for propulsion. The bacteria are not swimming freely but are loosely connected to the surface of the cantilever. Still, it is instructive to understand their propulsion mechanisms. Scientists have observed that the motion of these bacteria tend to follow a "run-and-tumble" pattern (Lauga and Powers, 2009) as illustrated in Figure 5·2. During the "run" period a bacterium will propel itself in a straight line for a short time by bundling its flagellar filaments tightly. Eventually, one flagellar motor reverses, causing the filaments to unwind, and the bacterium rotates in place (or "tumbles"). When the motor reverses direction again the bundle reforms and the "run" resumes in a new direction.

In our study we start with time-domain measurements, in which we observe an increase in the variance of the microcantilever fluctuations due to bacterial motion. In complementary frequency-domain measurements, we elucidate the spectral properties of the microcantilever fluctuations. The power of the fluctuations scale with frequency as $1/f^{\alpha}$ as well as with the surface density of the bacteria. We provide a basic physical model for the observed spectral distribution of the mechanical energy, and discuss implications of these results on biology and biosensor development.

5.2 Experimental Setup

We perform all experiments presented here in a custom liquid chamber (Fig. 5·3). The chamber is formed by gluing a rubber o-ring to a clean glass slide with aquarium epoxy. Biologically compatible adhesive is used to mount the cantilever in the center of the chamber. Liquid transfer into and out of the apparatus is achieved by manual micropipetting. We seal the chamber with a glass cover slip to allow for optical access to the microcantilever. The optical beam deflection technique (Meyer and Amer,

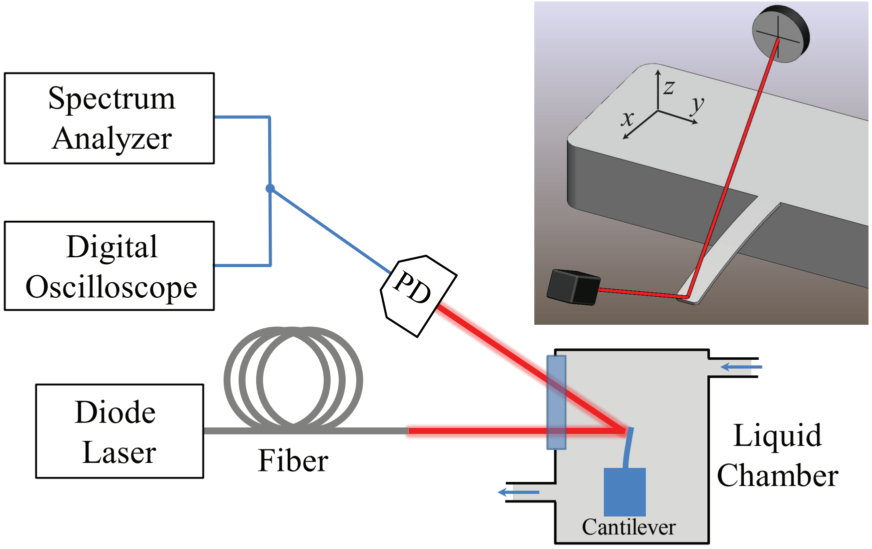

Figure 5·3: Schematic of the experimental setup. The cantilever is housed in a liquid chamber; its motion is probed using an optical technique. PD: photodetector. The inset shows the cantilever, the optical beam, and the split photodetector.

1988; Azak et al., 2007) is used to measure the fluctuations of the microcantilever, which has linear dimensions $l \times w \times t = 350 \times 32.5 \times 1\ \mu\text{m}^3$. Briefly, the optical beam reflecting from the tip of the microcantilever falls upon a split photodetector, which provides a voltage signal proportional to the tip displacement (inset of Fig. 5·3(a)). The displacement sensitivity of the technique is $\sim 10^{-12}$ m/Hz$^{1/2}$ in the frequency range 100 Hz $< f <$ 10 kHz. For $f \leq 100$ Hz, $1/f$-noise limits the displacement sensitivity to lower values (see Fig. 5·7). The voltage signal from the photodetector is converted to displacement units by using the thermal calibration technique (Butt and Jaschke, 1995) (see thermal spectrum inset of Fig. 5·7(a)). The microcantilever fluctuations are measured in the time domain with a digital storage oscilloscope and in the frequency domain with a FFT spectrum analyzer.

5.2.1 Sample Preparation

In the experiments, we used a genetically modified strain of *E. coli* (BL21 Star). The bacteria were transfected with pRSET-EmGFP plasmid consisting of ampicillin resistance and green fluorescence protein by incubating at 41° C for 30 seconds and transferred onto ice, as suggested by the manufacturer. The genetically modified strain was then incubated at 37° C on a shaking incubator at 250 RPM for an hour in lysogeny broth (LB) Broth (Lennox) containing catabolite repression medium. Next, the strain was plated onto LB agar containing 100 mg/mL of ampicillin, followed by a 16-hour incubation at 37° C. An individual *E. coli* colony was selected to inoculate in 5 mL of LB medium containing 100 mg/mL of ampicillin for 16 hours at 37° C on a shaking incubator at 250 RPM. To quantify the culture, the stock solution was diluted in phosphate-buffered saline (PBS) and spread onto LB-ampicillin plates, followed by an overnight incubation at 37° C. The individual colonies were then counted, and the stock solution was found to have a bacterial density of 10^9 colony forming units per milliliter (CFU/mL). We serially diluted the solution to create solutions of concentrations $C = 10^6$, 10^7, and 10^8 CFU/mL in PBS. To prepare the microcantilever surface for adhesion of bacteria, we first cleaned it with acetone, methanol, and isopropanol and dried in nitrogen gas. The cantilever was then submerged in a reservoir containing 1% (3-aminopropyl)triethoxysilane (APTES) dissolved in molecular biology grade water for 15 minutes, and was rinsed with water afterward. The APTES provided functional amine groups for bacterial attachment. Next, the cantilever was submerged in the *E. coli* solutions of various concentrations and incubated for 15 minutes at room temperature. During incubation, the bacteria adhered to the cantilever surface.

We confirmed bacterial adhesion by immediately imaging the cantilever surface with a microscope in fluorescence and in bright-field modes (Fig. 5·4). To quantify

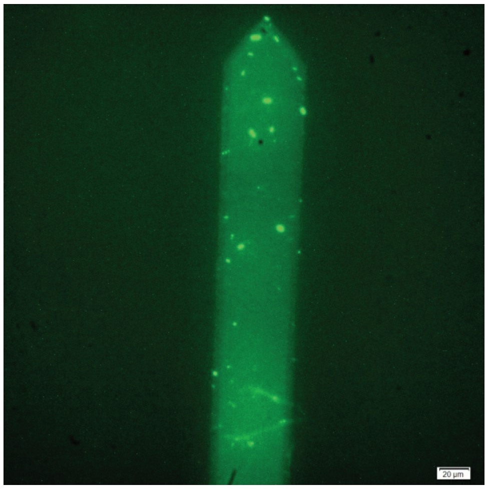

Figure 5·4: Fluorescence image of the cantilever after bacterial adhesion. Both single bacterium and clumps of bacteria are visible. Scale bar is 20 μm.

the number of bacteria adhered onto the surface, we performed a separate study, in which we adhered bacteria to large pieces of silicon using the above-described steps and imaged in bright-field. We subsequently used these images to obtain the average surface density of bacteria for all bacterial concentrations tested. We plot the surface density of the bacteria as a function of the bacterial concentration in solution in Figure 5·5. The error bars are due to the finite number of images analyzed (5 images of 300 × 300 μm^2 for each concentration), clumping of bacteria, and the occasional non-uniformities in coverage. To confirm statistical significance of the data we performed a one-way analysis of variance (ANOVA) with Tukey's posthoc test followed by Bonferroni's Multiple Comparison test for equal variances, and the statistical significance threshold was set to 0.05 ($p < 0.05$). We observed a statistically significant increase in bacteria count on the surface in the 10^8 CFU/mL case compared to the 10^6 and 10^7 CFU/mL cases ($n = 5$, $p < 0.05$).

A typical experiment began by measuring the fluctuations of the cantilever in PBS before bacterial adhesion. This determined the *baseline* for the fluctuations of the cantilever. After the collection of the baseline data, we proceeded with the bac-

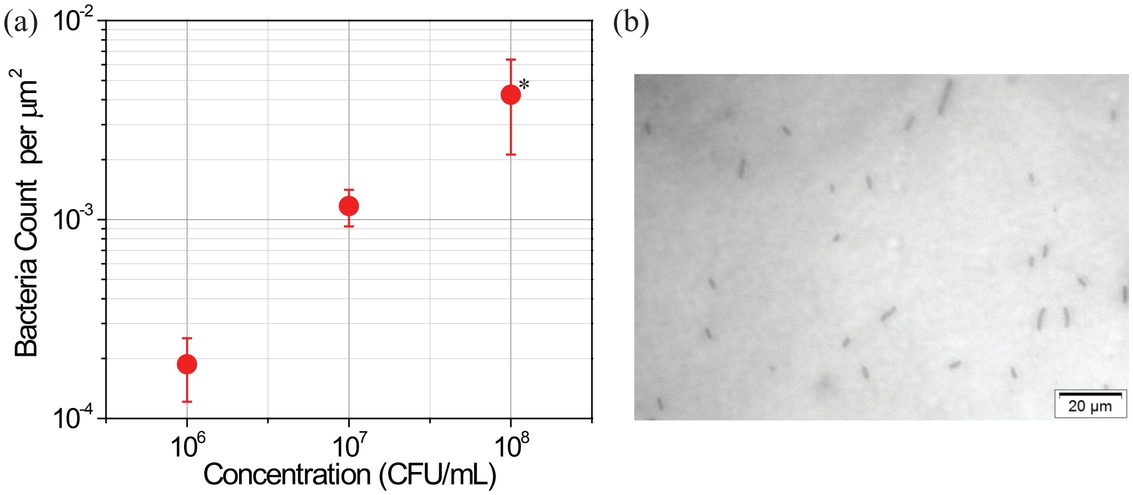

Figure 5·5: (a) Surface density of bacteria adhered to a silicon surface for three different bacterial concentrations. Data are indicated as averages ± standard deviations. * represents statistical significance of this data point. (b) Bright-field image of bacteria adhered to a silicon surface. Scale bar is 20 μm. Images like this were used to computer the densities in (b).

terial adhesion process, allowed time for incubation, and flushed the liquid chamber with PBS. We then repeated our measurement. Finally, we introduced to the liquid chamber a 1 mg/mL solution of streptomycin dissolved in water, allowed time for incubation, flushed the chamber with PBS, and repeated the measurement once more.

5.3 Results and Discussion

5.3.1 Time-Domain Measurements

All the time traces were collected for continuous periods of 40 s by sampling the signal at every $\tau = 0.32$ ms (i.e., at a sampling rate of 3.125 kSa/s) with a total of 1.25×10^5 data points. The signal was DC-coupled to an oscilloscope without any filters present. (The DC component of the signal was nulled by small adjustments to the optical beam with respect to the split photodetector.) We assume that the length

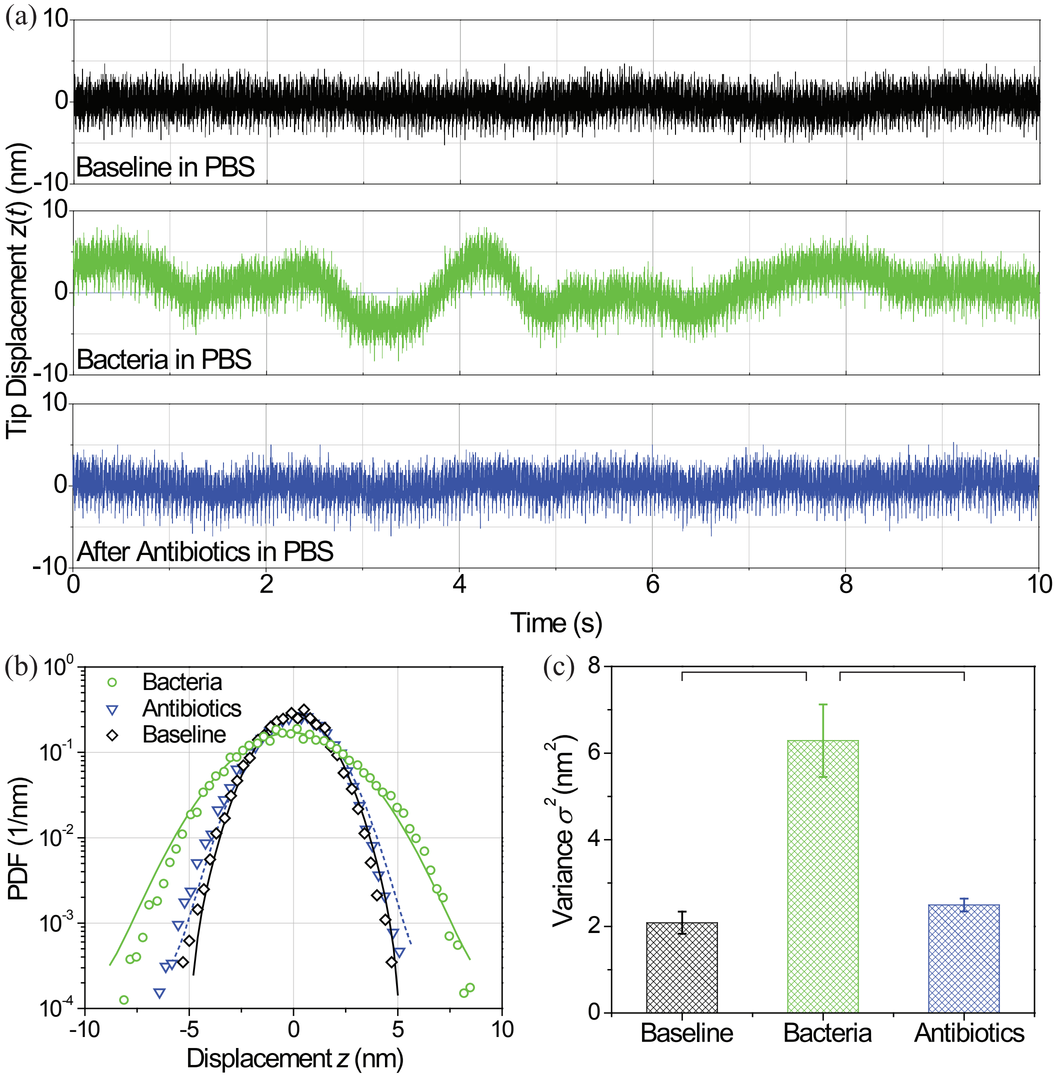

Figure 5·6: (a) Time-domain measurement of the microcantilever fluctuations. The top (black) trace is the baseline cantilever fluctuations with no bacteria present in PBS. The middle (green) trace is the same measurement after bacteria have adhered to the cantilever surface in a 10^8 CFU/mL solution. The data in Fig. 5·5 and the cantilever area suggest that the signal comes from $\sim 10^2$ bacteria on the microcantilever. The bottom (blue) trace is after the bacteria are killed in an antibiotic solution. (b) PDFs of the three time signals shown in (a) with Gaussian fits. (c) Variance of the microcantilever fluctuations measured from the three data traces in (a). Data are indicated as averages ± standard deviations. Brackets represent groups which were compared by statistical analysis.

C (CFU/mL)	N	${\sigma_0}^2$ (nm^2)	${\sigma_1}^2$ (nm^2)	${\sigma_1}^2 - {\sigma_0}^2$ (nm^2)
10^6	4	3.59	4.02	0.43
10^7	27	2.01	3.39	1.38
10^8	96	2.08	6.29	4.21

Table 5.1: Variance of displacement fluctuations. The number of bacteria N on the microcantilever was estimated from the concentration C using the data in Fig. 5·3(b). The variances for the baseline and bacteria experiments are ${\sigma_0}^2$ and ${\sigma_1}^2$, respectively; ${\sigma_1}^2 - {\sigma_0}^2$ quantifies the additional cantilever fluctuations induced by the bacterial motion.

of the time trace sets the lowest measurement frequency to ~ 0.025 Hz. Figure 5·6(a) depicts a typical time-domain measurement of the mechanical fluctuations of the tip of the microcantilever, $z(t)$, under different conditions. The top (black) trace shows the fluctuations measured in PBS before bacterial adhesion. The middle (green) trace shows the fluctuations after bacteria have been adhered to the cantilever as described above. Finally, the bottom (blue) trace shows the fluctuations after administration of the antibiotic streptomycin. The probability density function (PDF) of the three time signals is shown in Fig. 5·6(b) to demonstrate the Gaussian nature of the fluctuations. For these particular measurements a concentration of $C = 10^8$ CFU/mL of bacteria was used, and we estimate, using the data in Fig. 5·5(b), that there were $N \sim 10^2$ bacteria on the microcantilever. Qualitatively, there are differences between the middle trace with bacteria and the other two traces; the data taken after bacterial adhesion exhibit large-amplitude low-frequency fluctuations, which are not present in the no-bacteria case. The different characteristic frequencies in these data traces provided the motivation for measuring the spectrum of the fluctuations.

For each experiment, we repeated these measurements three times, waiting for $\sim 1/2$ hour between measurements, and computed the variance of the fluctuating time signal as

$$\sigma^2 = \frac{1}{N}\sum_{k=1}^{N}[z(k\tau) - \bar{z}]^2, \tag{5.1}$$

where $\bar{z}$ is the mean (typically $\bar{z} = 0$ m). In Table 5.1, we present these average variances from the cantilevers that were incubated in bacteria solutions with concentrations $C = 10^6$, $C = 10^7$, and $C = 10^8$ CFU/mL, corresponding to $N \sim 4$, $N \sim 30$ and $N \sim 10^2$ bacteria, respectively. The sample prepared using the lowest bacteria concentration ($C = 10^6$ CFU/mL) with $N \sim 4$ was below the uncertainty of the experimental measurement. In Table 5.1, ${\sigma_0}^2$ and ${\sigma_1}^2$ correspond to the variances for the baseline and bacteria experiments, respectively. We also subtracted ${\sigma_0}^2$ from ${\sigma_1}^2$ to obtain a quantitative measure of the additional cantilever fluctuations induced by the bacterial motion. The higher bacterial concentration case exhibits a larger increase in variance than the lower concentration case. The average variances for the $C = 10^8$ CFU/mL experiment are also depicted graphically in Fig. 5·6(c). These values match those found from the Gaussian fits of the PDFs in Fig. 5·6(b). To confirm statistical significance of the data, we performed a statistical analysis on the variance measurements. We observed that the variance of the fluctuations after bacteria adhesion was significantly greater than the other two cases (baseline and antibiotics) ($n = 3$, $p < 0.05$). Further, after the application of antibiotics to the bacteria-adsorbed surfaces, the signal decreased to the baseline level. The statistical analysis demonstrated that the time domain data for baseline and antibiotics were not significantly different ($n = 3$, $p > 0.05$).

5.3.2 Frequency-Domain Measurements

All the PSD measurements were performed with a FFT spectrum analyzer using the following resolution bandwidths (RBW): RBW ≈ 0.25 Hz for $0.25 \text{ Hz} \leq f \leq 100$ Hz; RBW ≈ 1 Hz for $100 \text{ Hz} \leq f \leq 500$ Hz; and RBW ≈ 16 Hz for $f \geq 500$ Hz.

Figure 5·7(a) depicts the power spectral density (PSD) $S_z(f)$ of the fluctuations of the microcantilever tip in a double-logarithmic plot under three different conditions: the black trace (lower, solid) $S_z^0(f)$ is obtained in PBS before bacterial adhesion; the green trace (upper, solid) $S_z^1(f)$ is obtained after the adhesion of bacteria in the $C = 10^8$ CFU/mL bacteria solution; the blue line (lower, dashed) is obtained after administration of streptomycin. The PSD increases after bacterial adhesion, but only in the frequency range $f \lesssim 100$ Hz. After incubation in antibiotics, we observe that the PSD returns to the baseline (no bacteria) level to within experimental error.

The presented data were averaged at two different time scales: to suppress the random noise, 1000 traces were averaged during collection; to assess longer-term drifts, the measurement was repeated three times with $\sim 1/2$ hour temporal separation. The standard deviation between the measurements obtained at different times is shown as the shaded regions of uncertainty in Fig. 5·7. (The error bars are shown only in the relevant frequency region.)

The calibration of the displacements was based on the thermal resonance peak visible around $f_R \approx 2.5$ kHz using standard AFM calibration practices. The inset shows the thermal peak in a linear plot. The (red) line is a fit to the damped harmonic oscillator model driven by the fluctuations in a liquid (Paul et al., 2006) with the addition of white noise. The PSD has a resonance frequency $f_R \approx 2.5$ kHz and quality factor $Q \approx 1.5$. The cantilever is assumed to be at room temperature, composed of silicon, and has a spring constant of $K \approx 0.03$ N/m.

5.3.3 Physical Model

Returning to Fig. 5·7(a), we notice that, at the low frequency region, the noise data can be approximated by $1/f^\alpha$ with $\alpha \approx 2$. This is the noise signature of our measurement setup, possibly the laser (Labuda et al., 2012). To find the power spectral density $S_z^B(f)$ of bacterial motion, we naïvely subtract the PSDs, $S_z^B(f) \approx S_z^1(f) - S_z^0(f)$,

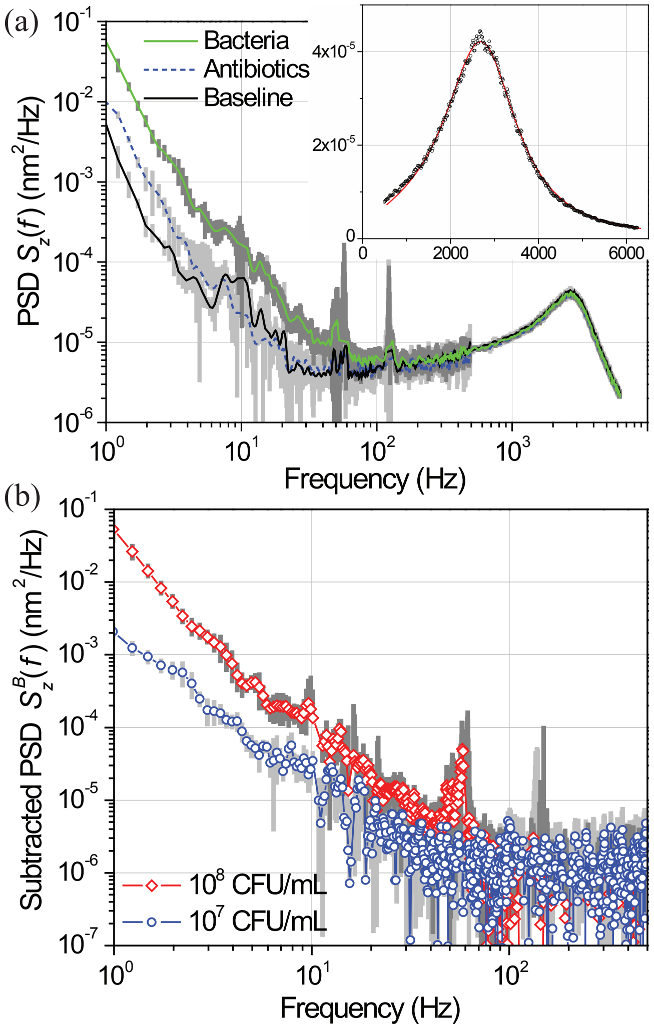

Figure 5·7: (a) PSD of microcantilever fluctuations as a function of frequency in a *double-logarithmic* plot. Single standard deviations are shown in gray behind the data traces. The cantilever thermal resonance is at $f_R \approx 2.5$ kHz with $Q \approx 1.5$. The inset shows this thermal peak in PBS in a *linear* plot. The data are fitted to a damped harmonic oscillator model driven by fluid fluctuations. (b) Subtracted PSD of the microcantilever fluctuations as a function of frequency. The PSD of the baseline is subtracted from that measured after bacterial adhesion.

i.e., we subtract the black curve from the green curve. The subtracted PSDs are shown in Fig. 5·7(b). The extra noise power due to the bacteria is not appreciable for $f \gtrsim 80$ Hz. It appears that the majority of the noise power stays at low frequencies; $S_z^B(f) \propto 1/f^\alpha$ for 1 Hz $\lesssim f \lesssim 80$ Hz.

Although it is typically difficult to untangle $1/f$ noise sources (Dutta and Horn, 1981), several features in the data suggest that subtraction of the PSDs as described above effectively removes the experimental $1/f$ noise. First, in Fig. 5·7(a), the PSD of cantilever fluctuations with adsorbed bacteria is almost an order of magnitude above the baseline. Second, in Fig. 5·7(b), the additional noise power coming from the bacteria, i.e., $S_z^B(f)$, grows with the number of bacteria on the microcantilever. Convinced that the observed $1/f$-like behavior is indeed due to the bacteria, we turn to a discussion of possible explanations. Many diverse biological processes fluctuate with PSDs $S(f) \sim 1/f^\alpha$. While the ubiquity of this $1/f$ behavior is intriguing, it may only be a reflection of the simple fact that the measured signal combines many processes that act on different time scales (Hausdorff and Peng, 1996). Here, each bacterium exhibits motions with different characteristic time scales τ_i and amplitudes A_i. For instance, τ_i can pertain to the motion of the cilia; the motion of the flagella; and even the slow diffusive motion of the entire bacterium on the surface due to the breaking and re-forming of chemical bonds. The spectral density of the motion of a single bacterium can thus be considered to be a sum of these different spectral densities, $\sum\limits_i \frac{{A_i}^2\tau_i}{1+(2\pi f\tau_i)^2}$. This argument suggests that the noise power spectral density of a single bacterium should be $\sim 1/f^\alpha$ with α determined by the interplay between the numerous time scales τ_i present in the problem. While this simple explanation may be satisfactory for a first-pass analysis, a comprehensive model should take into account further complexities due to the fact that the cantilever responds to input from many bacteria. For instance, bacteria will have a distribution of sizes and thus time scales; bacteria are positioned randomly on the cantilever; the coupling strength of the motion of each bacterium to the cantilever will be different; and so on.

5.4 Conclusions and Outlook

Regarding sensor applications, we emphasize that conventional methods for studying bacterial behavior and detecting bacteria are time consuming and require expensive infrastructure. Recent biosensing approaches developed on microfluidic platforms based on electrical and optical sensing are not able to monitor bacterial motion and antibiotic resistance in real-time (Wang et al., 2012a; Wang et al., 2012b; Inci et al., 2013; Tokel et al., 2014; Mani et al., 2014; Shafiee et al., 2013); similarly, micromechanical detection based on frequency shifts of a microcantilever resonator does not provide enough sensitivity in viscous liquids (Ekinci et al., 2010). For instance, there was no noticeable frequency shift in our experiments due to the mass of the bacteria, while fluctuations due to the bacteria were detectable. The theoretical limit for the minimum detectable mass based on frequency shift is of order $M_c/Q \sim 2 \times 10^{-11}$ kg (Ekinci et al., 2004), where M_c is the cantilever mass. Given that the mass of a single *E. coli* is $\sim 1 \times 10^{-15}$ kg, $\sim 10^4$ bacteria are needed for a detectable frequency-shift based signal. All these suggest that, by monitoring the fluctuations of a cantilever, one can develop functional and versatile sensors. It may be possible to enhance the fluctuation signal by lowering the spring constant of the microcantilever; this may reduce the resonance frequency and make the resonator overdamped in liquid. Careful modeling is required for finding the optimal design parameters for next generation sensors.

In this chapter, we measured the nanomechanical spectrum of the forces that bacteria exert on a microcantilever from the fluctuations of the microcantilever. We observed that the amplitude of the fluctuations scales with frequency as $1/f^{\alpha}$ $(2 \leq$

$\alpha \leq 3$) as well as the surface density of the bacteria. Our physical model suggests that each bacterium provides fluctuations with multiple time scales and amplitudes, resulting in a collective $1/f$-like spectrum.

Chapter 6

Noisy Transition to Turbulence in Microchannels

In this chapter, we present an experimental study of a noisy transitional flow in a microchannel. We use a microcantilever sensor embedded in the microchannel wall and perform two sets of experiments in the same microchannel: first, we study transition triggered by the natural imperfections of the walls; subsequently, we study transition under artificially added inlet noise. The two experiments result in random flows in which high-order moments of near-wall fluctuations differ by orders of magnitude. Surprisingly however, the lowest order statistics in both cases appear qualitatively similar and can be described by a proposed noisy Landau equation for a slow mode. The noise, regardless of its origin, regularizes the Landau singularity of the relaxation time and makes transitions driven by different noise sources appear similar.

6.1 Introduction

More than a century ago, Osborne Reynolds investigated the transition to turbulence in glass pipes in a series of experiments in which he injected a filament of dye at the pipe inlet (Reynolds, 1883). Reynolds noticed that the characteristics of the dye filament and hence the entire flow field depended on the dimensionless flow rate or the Reynolds number, $\mathrm{Re} = UD/\nu$ (here, U is the mean flow velocity, D the pipe diameter, and ν the kinematic viscosity of the fluid). Below a critical value $\mathrm{Re} \ll \mathrm{Re}_{\mathrm{cr}}$, the dye propagated downstream as a thin filament without breaking up, indicating a laminar flow in the pipe. At $\mathrm{Re} \geq \mathrm{Re}_{\mathrm{cr}}$, this pattern changed dramatically: waves appeared in the vicinity of the inlet, sometimes leading to substantial flow randomization downstream. With increasing Re, the fraction of the tube length occupied by these waves increased, and at $\mathrm{Re} \gg \mathrm{Re}_{\mathrm{cr}}$, the entire flow became turbulent.

Reynolds, however, was unable to determine a *unique* value for $\mathrm{Re}_{\mathrm{cr}}$. He noticed that the value of $\mathrm{Re}_{\mathrm{cr}}$ was sensitive to various imperfections, most notably the geometry of the inlet. If the inlet was sharp, inlet perturbations appeared in the form of shedded vortices that caused transition to turbulence at large Reynolds numbers. These perturbations, however, rapidly decayed downstream, if Reynolds number was not too large. By carefully eliminating these, Reynolds was able to delay the transition up to $\mathrm{Re} \approx 12,800$ (Reynolds, 1883). Others following Reynolds were able to sustain laminar flows in pipes even for Reynolds numbers as high as $100,000$ (Pfenninger, 1961). Relatively recently, the effect of initial (inlet) perturbations on $\mathrm{Re}_{\mathrm{cr}}$ were quantified by introducing well-controlled disturbances (called turbulent "puffs" or "slugs"), which filled the entire pipe cross-section and were able to travel along the length of the pipe, in a laminar flow (Darbyshire and Mullin, 1995). Consistent with Reynolds' observations, the flow became turbulent at smaller and smaller Reynolds numbers as the ratio of the disturbance velocity to the mean flow velocity was increased. (For a comprehensive review, see (Yaglom, 2012).)

The above-described "decay or amplification" of waves (or perturbations) forms the basis of Landau's phenomenological theory of transition (Landau and Lifshitz, 1987). Landau's theory, though insightful, is better applicable to wakes in flows past bluff bodies (Sreenivasan et al., 1987) and in convection, i.e., in situations where wall effects and viscosity do not dominate. It is well-justified in pipe flows when the characteristic size of a perturbation is $\mathcal{O}(D)$ and wall effects are unimportant, e.g., in the case of puffs or slugs. Efforts to describe transition in pipes using the Landau theory, most notably by Stuart and others (Stuart, 1971), focused on obtaining the magnitudes of the coefficients γ_1 and α (as will be described below) and testing their possible universality. This universality remains elusive, suggesting that wall effects must be important in transition. Numerical simulations and experimental data show that, at least in the range $2300 \leq \mathrm{Re} \leq 10^5$, powerful bursts generated by unstable boundary layers are mainly responsible for turbulence production in the bulk.

The majority of researchers studying transition to turbulence in pipes have been interested in the flow response to perturbations at the inlet in an otherwise perfect pipe (Yaglom, 2012). This interest can partially be explained by the mathematical well-posedness of the problem and by the emergence of numerical methods combined with powerful computers. Conversely, the "fuzzy" problem involving inlet disturbances, pipe imperfections, and pipe roughness has not attracted as much attention (Pausch and Eckhardt, 2015). In this chapter, we focus, both experimentally and theoretically, on transition to turbulence triggered by noise in an imperfect microchannel. Experimentally, we show that adding inlet disturbances, while keeping everything else the same, strongly influences the transition process. Our measurements of the frequency spectra and the probability distributions of near-wall fluctuations provide insights into transition to turbulence in a noisy flow. To describe our experimental observations, we propose a modified Landau theory in which all imperfection-induced flow disturbances are treated as added high-frequency noise. This theory agrees well with our experimental observations. An important consequence of this theory is that noise regularizes the Landau singularity of the relaxation time.

6.2 Theory

6.2.1 Landau's Stability Analysis

The stability of a laminar flow in Landau's interpretation is formulated as follows. Consider an infinitesimally small perturbation $\mathbf{v}$ to the laminar (transitional) velocity field $\bar{\mathbf{u}}$, so that the total velocity is $\mathbf{u} = \bar{\mathbf{u}} + \mathbf{v}$ and the total pressure is $p = p_0 + p_1$. Then, the Navier-Stokes equations

$$\frac{\partial \mathbf{u}}{\partial t} + \mathbf{u} \cdot \nabla \mathbf{u} = -\frac{\nabla p}{\rho} + \nu \nabla^2 \mathbf{u}; \qquad \nabla \cdot \mathbf{u} = 0 \tag{6.1}$$

can be written as:

$$\bar{\mathbf{u}} \cdot \nabla \bar{\mathbf{u}} = -\frac{\nabla p_0}{\rho} + \nu \nabla^2 \bar{\mathbf{u}}; \qquad \nabla \cdot \bar{\mathbf{u}} = 0 \tag{6.2}$$

and

$$\frac{\partial \mathbf{v}}{\partial t} + \bar{\mathbf{u}} \cdot \nabla \mathbf{v} + \mathbf{v} \cdot \nabla \bar{\mathbf{u}} + \mathbf{v} \cdot \nabla \mathbf{v} = -\frac{\nabla p_1}{\rho} + \nu \nabla^2 \mathbf{v}; \;\; \nabla \cdot \mathbf{v} = 0 \tag{6.3}$$

subject to the boundary condition that $\bar{\mathbf{u}}$ and $\mathbf{v}$ both vanish on the solid walls. Neglecting the $\mathcal{O}(v^2)$ contribution to Eq. (6.3) results in linearized Navier-Stokes equations to be used for investigating instabilities in fluid flows.

Now, the task is to find a solution to Eqs. (6.2-6.3) describing the time evolution of an initially ($t = 0$) infinitesimally small perturbation $\mathbf{v}$. In this case, the $\mathcal{O}(v^2)$ contribution to Eq. (6.3) is neglected. For the perturbation, Landau assumed the form $\mathbf{v}(\mathbf{r}, t) = A(t)\mathbf{f}(\mathbf{r})$, where $A(t) = \text{constant} \times e^{-i\Omega t}$ is the slowly-varying amplitude with a complex eigenfrequency, $\Omega = \omega_1 + i\gamma_1$, and $\mathbf{f}(\mathbf{r})$ describes the spatial dependence. We find $A(t) = \text{constant} \times e^{\gamma_1 t - i\omega_1 t}$ so that waves will decay if $\gamma_1 < 0$ and grow if $\gamma_1 > 0$. From the form of $A(t)$ we see that it must satisfy the equation

$$\frac{d|A|^2}{dt} = 2\gamma_1 |A|^2, \tag{6.4}$$

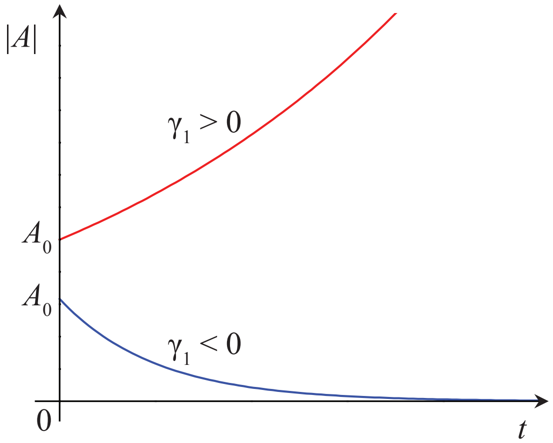

Figure 6·1: Time evolution of the disturbance amplitude $|A(t)|$ considering only second-order terms in A (as in Eq. (6.4)) for positive (red line) and negative (blue line) values of γ_1.

where $\gamma_1 \propto (\mathrm{Re} - \mathrm{Re}_{\mathrm{cr}})$. The time evolution of the disturbance amplitude $|A(t)|$ is shown in Figure 6·1 for positive (red line) and negative (blue line) values of γ_1.

This description, however, is only valid if the Re of the flow is not too large (small γ_1) and the initial disturbance amplitude $A(0)$ is small. We quickly realize that we must consider higher order terms to develop a more complete theory. The third order terms in A and the complex conjugate A^* (such as terms proportional to AA^{*2} and A^2A^*) will oscillate with frequency ω_1. These periodic oscillations are rapid in comparison with the rate of change of $A(t)$ ($|\omega_1| \gg |\gamma_1|$). If we average over a time scale that is large compared to $2\pi/|\omega_1|$ but small compared to $1/|\gamma_1|$, these third-order terms will disappear. The next higher order terms will be proportional to $|A|^4$ and we write

$$\frac{d|A|^2}{dt} = 2\gamma_1|A|^2 - \alpha|A|^4. \tag{6.5}$$

The fourth-order terms do not oscillate at frequency ω_1 and they survive the averaging process. Equation (6.5) is known as the *Landau equation* and its general solution can

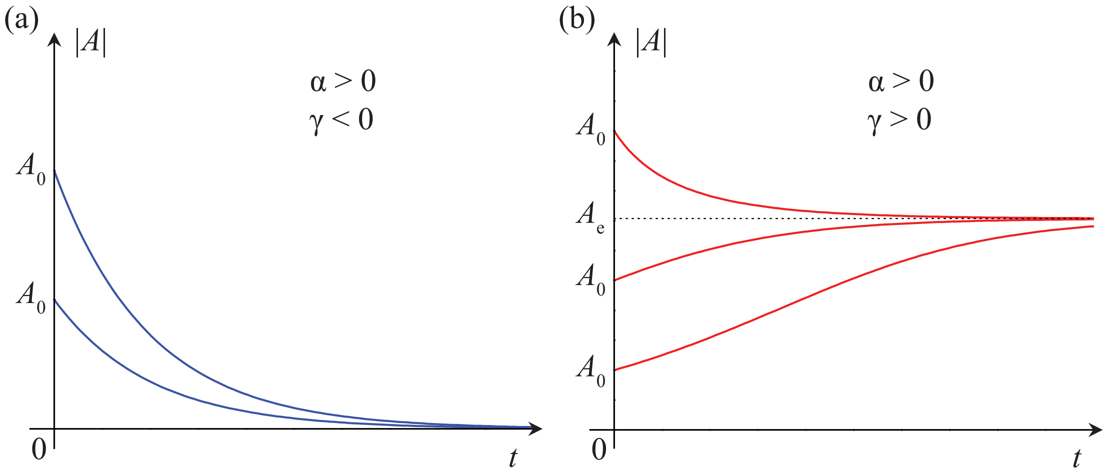

Figure 6·2: Time evolution of the disturbance amplitude $|A(t)|$ considering up to fourth-order terms in A (as in Eq. (6.5)) for different initial disturbance amplitudes A_0 with (a) $\alpha > 0$ and $\gamma_1 < 0$ and (b) $\alpha > 0$ and $\gamma_1 > 0$. The asymptotic value A_{e} is also shown as a dotted line in (b).

be found as

$$\frac{|A(t)|^2}{|A_0|^2} = \frac{e^{2\gamma_1 t}}{1 + |A_0|^2 \frac{\alpha}{2\gamma_1}(e^{2\gamma_1 t} - 1)}, \tag{6.6}$$

where $A(0) = A_0$ is the initial perturbation amplitude.

The sign of the parameter α in Eq. (6.5) determines whether nonlinear effects will work to stabilize ($\alpha > 0$) or destabilize ($\alpha < 0$) the disturbance. First, we consider the case of positive values of α. Here, setting $\gamma = c(\mathrm{Re} - \mathrm{Re}_{\mathrm{cr}})$, one can reproduce the observed "decay or amplification" of perturbations. We plot the time evolution of the disturbance amplitude in Figure 6·2 for $\gamma_1 < 0$ and $\gamma_1 > 0$ in (a) and (b), respectively. When $\mathrm{Re} - \mathrm{Re}_{\mathrm{cr}} < 0$ ($\gamma_1 < 0$), all perturbations decay ($A(t) \to 0$) in the limit $t \to \infty$ ($t \gg 1/\gamma_1$). When $\mathrm{Re} - \mathrm{Re}_{\mathrm{cr}} > 0$ ($\gamma_1 > 0$), the amplitude grows, saturating at $|A(\infty)| = A_{\mathrm{e}} = (2\gamma_1/\alpha)^{1/2}$ and we note that this asymptote is proportional to $(\mathrm{Re} - \mathrm{Re}_{\mathrm{cr}})^{1/2}$. This asymptote is shown as a dotted line in Figure 6·2(b). In the case of $\gamma_1 > 0$ it is apparent that disturbances with initial amplitudes smaller than the equilibrium value ($A_0 < A_{\mathrm{e}}$) will be amplified and will saturate at A_{e}. Disturbances

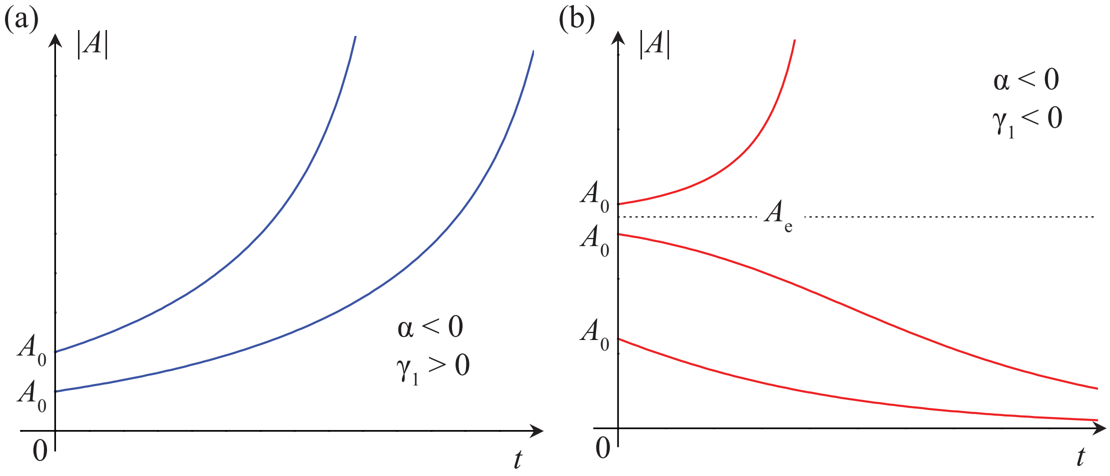

Figure 6·3: Time evolution of the disturbance amplitude $|A(t)|$ considering up to fourth-order terms in A (as in Eq. (6.5)) for different initial disturbance amplitudes A_0 with (a) $\alpha < 0$ and $\gamma_1 > 0$ and (b) $\alpha < 0$ and $\gamma_1 < 0$. The asymptotic value A_e is also shown as a dotted line in (b).

with initial amplitudes larger than the equilibrium value ($A_0 > A_\mathrm{e}$) will decay to A_e over time.

We now consider the case of negative values of α where the fourth-order term in Eq. (6.5) serves to destabilize the disturbance to the flow. We plot the time evolution of the disturbance amplitude in Figure 6·3 for $\gamma_1 > 0$ and $\gamma_1 < 0$ in (a) and (b), respectively. When $\gamma_1 < 0$, all perturbations with initial amplitude less than the asymptotic value ($A_0 < A_\mathrm{e}$) will decay ($A(t) \to 0$) in the limit $t \to \infty$. If, however, $A_0 > A_\mathrm{e}$, the perturbation will be amplified. In the case of $\gamma_1 > 0$, the amplitude grows indefinitely regardless of the initial perturbation amplitude.

We see that in these cases, where $A(t) \to \infty$, Eq. (6.5) is not sufficient to describe the system and we must consider even higher-order terms. We neglect the fifth-order terms which average to zero (as in the case of the third-order terms) and we add a term of sixth-order in $|A|$, $-\beta|A|^6$ with $\beta > 0$. We write

$$\frac{d|A|^2}{dt} = 2\gamma_1|A|^2 + |\alpha||A|^4 - \beta|A|^6. \tag{6.7}$$

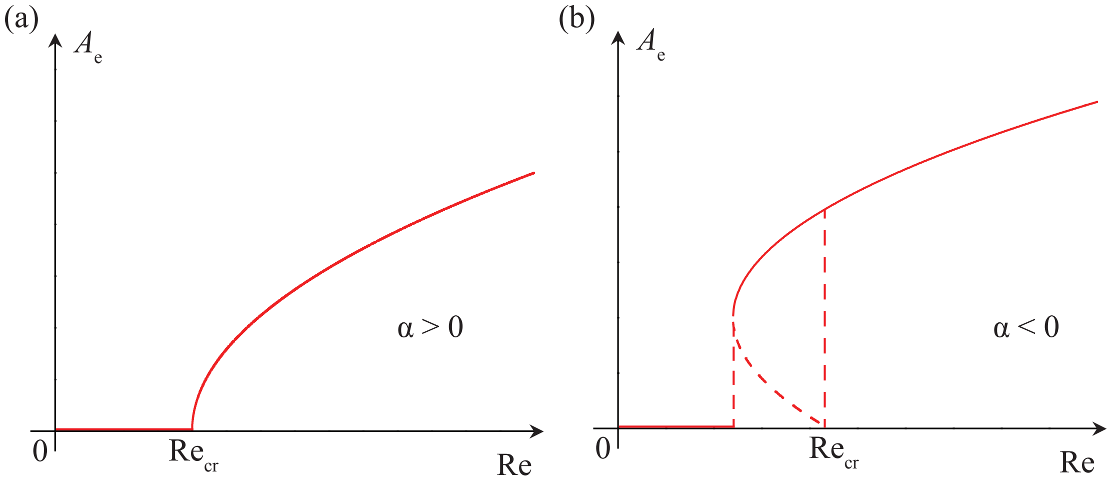

Figure 6·4: The long-time limit of the disturbance amplitude (A_e) versus Re for $\alpha > 0$ (a) and $\alpha < 0$ (b).

In the long time limit, this gives us

$$|A(\infty)|^2 = \frac{|\alpha|}{2\beta} \pm \sqrt{\frac{|\alpha|^2}{4\beta^2} + \frac{2\gamma_1}{\beta}}. \tag{6.8}$$

The long time limit of the disturbance amplitude $A_e = |A(\infty)|$ is shown versus the Reynolds number in Figure 6·4 for $\alpha > 0$ and $\alpha < 0$ in (a) and (b), respectively. In the case of $\alpha > 0$, Eq. (6.5) is sufficient to describe the flow and we simply have $A_e = (2\gamma_1/\alpha)^{1/2}$. If $\alpha < 0$ the system has a range of Re for which it can be considered to be *metastable*, that is, perturbations of large enough amplitude will be amplified while smaller perturbations will decay. The unstable region is represented by dashed lines in the figure.

The above theory, particularly Eq. (6.4), suggests that information about the initial conditions of the flow disappears on a time scale $\tau = \frac{1}{2|\gamma_1|} \propto \frac{1}{|\mathrm{Re}-\mathrm{Re}_{cr}|}$. This behavior is similar to the "critical slowing down" in the proximity of a critical point in phase transitions (Procaccia and Gitterman, 1981). In pipe flows, it has important and interesting consequences. A perturbation occurring at position l and being advected by a mean flow of velocity U stays in the pipe for a time interval $t_0 \approx (L - l)/U$, where

L is the pipe length. Therefore, to observe the decay of a perturbation generated in the *bulk* or its growth toward a final turbulent state, one needs $t_0 \gg \tau$, requiring unreasonably long pipes around $\mathrm{Re}_{\mathrm{cr}}$. The divergent relaxation time $\tau \propto |\mathrm{Re} - \mathrm{R}_{\mathrm{cr}}|^{-\zeta}$ with $\zeta \approx 0.56$ was also recently obtained in numerical simulations of transition in force-driven Navier-Stokes equations by McComb et al. (McComb et al., 2014).

6.2.2 Landau's Stability Analysis with Noise

In this section we consider the non-idealities in our experimental system which may trigger perturbations in the flow. We incorporate this experimental noise into the Landau theory by considering a general additive noise term $\phi(t)$. We assume that a high-frequency random Gaussian force $\phi(t)$ defined by the correlation function $\overline{\phi(t)\phi(t')} = 2\overline{\phi^2}\delta(t-t')$ stirs the fluid. Then, Eq. (6.3) is modified as

$$\frac{\partial \mathbf{v}}{\partial t} + \bar{\mathbf{u}} \cdot \nabla \mathbf{v} + \mathbf{v} \cdot \nabla \bar{\mathbf{u}} + \mathbf{v} \cdot \nabla \mathbf{v} = -\frac{\nabla p_1}{\rho} + \nu \nabla^2 \mathbf{v} + \phi(t). \tag{6.9}$$

Repeating Landau's arguments leading to Eq. (6.5), we write

$$\frac{\partial A}{\partial t} = \gamma_1 A - \frac{\alpha}{2} A^3 + \phi(t) \tag{6.10}$$

Averaging over high-frequency fluctuations gives a modified Landau equation for the slow mode:

$$\frac{d|A|^2}{dt} = 2\gamma_1 |A|^2 - \alpha |A|^4 + \overline{\phi^2}. \tag{6.11}$$

In a force-driven flow with initial condition $A_0 = 0$, the solution to Eq. (6.11) is

$$|A(t)|^2 = \frac{\gamma_1}{\alpha} + \frac{\beta_- - \beta_+ e^{-\frac{t}{\tau}}}{\beta_- + \beta_+ e^{-\frac{t}{\tau}}} \left(\beta_+ - \frac{\gamma_1}{\alpha} \right). \tag{6.12}$$

where

$$\beta_\pm = \pm \frac{\gamma_1}{\alpha} + \sqrt{\frac{{\gamma_1}^2}{\alpha^2} + \frac{\overline{\phi^2}}{\alpha}} > 0 \tag{6.13}$$

and the relaxation time is

$$\tau = \frac{1}{2\sqrt{\gamma_1^2 + \overline{\phi^2}\alpha}}. \tag{6.14}$$

This gives in the long-time limit:

$$|A(\infty)|^2 = \beta_+ = \frac{\gamma_1}{\alpha} + \sqrt{\frac{{\gamma_1}^2}{\alpha^2} + \frac{\overline{\phi^2}}{\alpha}}. \tag{6.15}$$

Remembering that in Landau theory $\gamma_1 = c(\mathrm{Re} - \mathrm{Re}_{\mathrm{cr}})$, we notice an important consequence of noise: the relaxation time τ remains finite in the limit $\mathrm{Re} \to \mathrm{Re}_{\mathrm{cr}}$, in contrast to the "critical slowing down" discussed above. Thus, the external noise source regularizes the dynamics around the transition point. In addition, Eq. (6.10) indicates that, when A is small in the low Re limit so that the $\mathcal{O}(A^3)$ contributions can be neglected, A obeys Gaussian statistics.

6.3 Experiment

To test these ideas, we have designed an experiment in a rectangular micro-channel in which the inlet condition can be modified to create artificial perturbations. The rectangular micro-channel has linear dimensions $L \times W \times H = 35 \times 8 \times 0.9$ mm^3 with hydraulic diameter $D \approx 1.6$ mm. The circular inlet and outlet tubes have diameters of ≈ 8 mm. A pressurized air source is used to establish air flow in the channel. The flow rate is monitored using a rotameter, and the pressure drop between the inlet and outlet is measured using a differential pressure gauge. Two different inlet conditions were investigated as illustrated in Figure 6·5(a): (i) the inlet was unblocked; (ii) the inlet was partially blocked by a mesh made up of a relatively loose plug of steel wool with 25 μm fiber thickness. The near-wall flow in the microchannel is probed by a rectangular microcantilever with linear dimensions $l \times w \times h = 225 \times 27.5 \times 3.0$ μm^3. The chip carrying the microcantilever is embedded in the bottom wall of the micro-

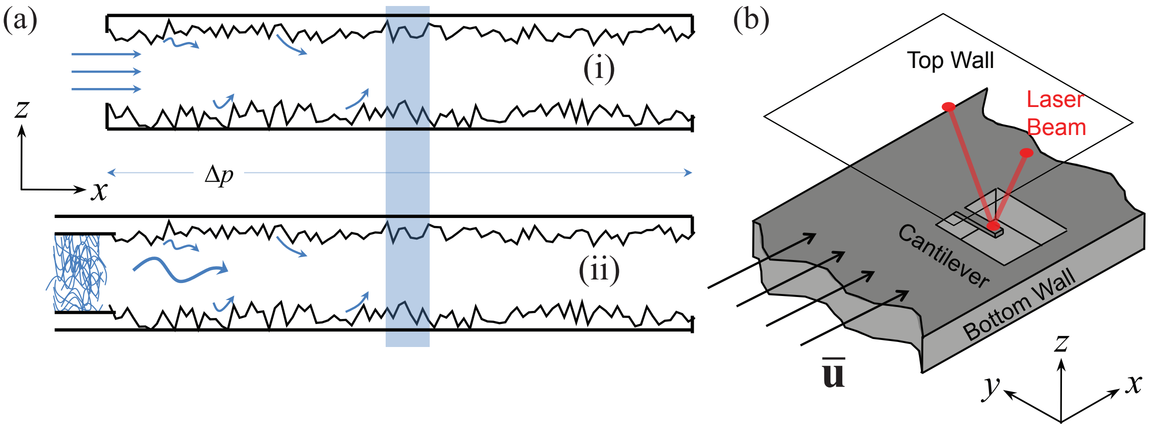

Figure 6·5: (a) Rectangular micro-channel with linear dimensions $L \times W \times H = 35 \times 8 \times 0.9$ mm^3 shown in cases (i) and (ii). The hydraulic diameter is $D \approx 1.6$ mm. The test section is highlighted in blue. (b) The microcantilever chip is integrated to the middle of the bottom wall seamlessly.

channel by a surrounding aluminium structure (Figure 6·5(b)). The test section is approximately 17 mm ($\approx 11D$) from the inlet (highlighted in blue in the figure). The channel has a transparent top wall, and the motion of the tip of the microcantilever is read out using the optical beam deflection technique (Meyer and Amer, 1988) as discussed in Chapter 2.

We conduct scanning white light interferometry measurements to determine the surface roughness of the channel walls and the cantilever surface. We find the silicon surface of the cantilever to have an RMS roughness of ~ 30 nm over an area of 0.71×0.53 mm. The upper channel wall is made from machined polycarbonate and has an RMS roughness of ~ 270 nm over the same area. The aluminum structure surrounding the cantilever chip (made from aluminum shim stock) has a local roughness of ~ 290 nm but wide-field images covering the entire length of the channel show a variation as large as ± 100 μm. One full-field white light interferometer image of the type used to estimate roughness is shown in Figure 6·6(a). The image covers the entire length of the channel and is constructed by stitching together many measure-

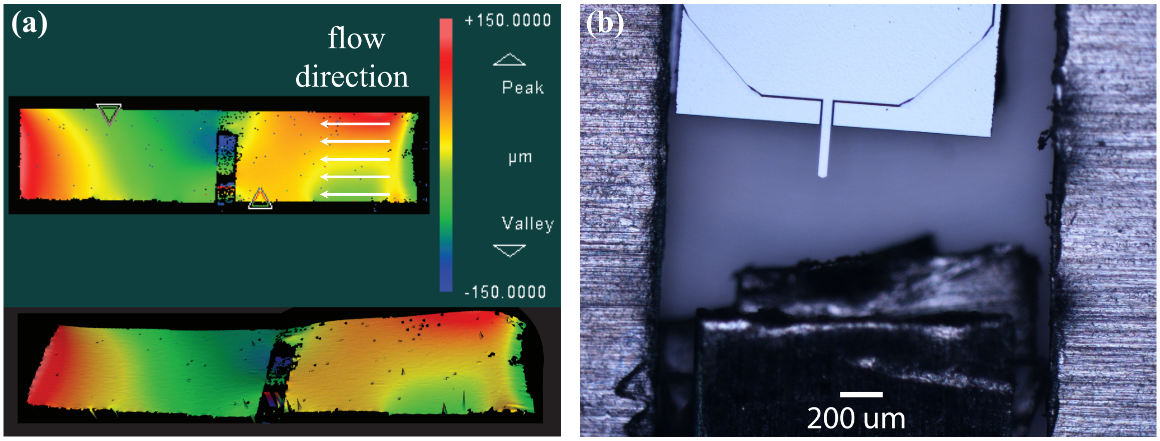

Figure 6·6: (a) White light interferometer image of the microchannel (b) Optical image of the microcantilever and the surrounding aluminum structure. Scale bar is 200 μm.

ments of smaller areas. We also show an optical image of the cantilever mounted in the channel in Figure 6·6(b). The cantilever, cantilever chip, and surrounding aluminum shim stock are visible in the image. We see that there is a gap of $\sim 200\ \mu$m between the left and right sides of the chip and the aluminum shim stock. The gap between the cantilever tip and the nearest aluminum is $\sim 500\ \mu$m. Reducing the gap between the cantilever and the surrounding structure is difficult in practice but future experiments can incorporate a hole in the wall of the channel so that the cantilever can be embedded more carefully.

Our flow sensor, the microcantilever, responds to pressures acting on its top and bottom surfaces, and moves primarily in the z direction. We model the cantilever as a one-dimensional damped harmonic oscillator with a complex linear response function $G(\omega) = \frac{1}{m({\omega_0}^2 - \omega^2 + i\omega\omega_0/Q)}$. Here, m is the mass and Q is the quality factor of the mode (the fundamental mode). The square root of the power spectrum of the system response under no flow is shown in Figure 6·7. The fundamental resonance of the cantilever is clearly visible at $f_0 \approx 80$ kHz with a quality factor $Q \approx 190$. These thermally-excited resonant oscillations appear above our noise floor because of the

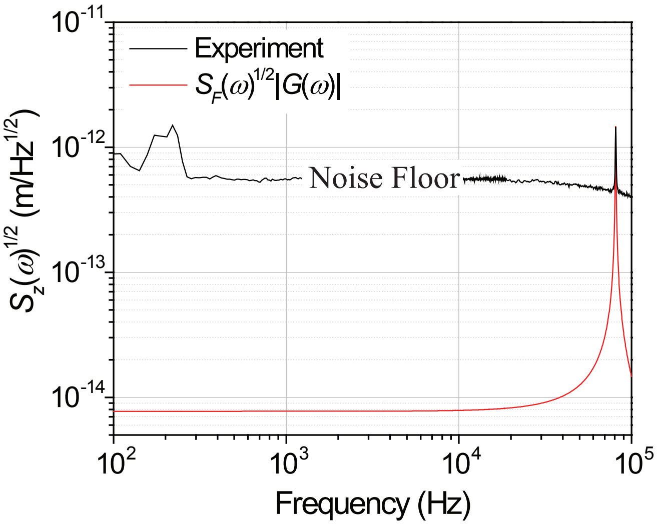

Figure 6·7: Square root of the power spectral density of the noise in the system. The peak at 80 kHz is due to the thermal oscillations of the cantilever. The cantilever motion is obscured below the resonance due to technical noise. The red curve is the calculated thermal response of the cantilever.

high Q of the cantilever. The high Q ensures that almost all of the thermal noise is accounted for in the resonant motion (Saulson, 1990), allowing calibration using the equipartition theorem (Butt and Jaschke, 1995).

After extracting the cantilever parameters from its resonance and determining the calibration factors, we can compute the thermal response of the microcantilever over the entire frequency range. This is the lower curve shown in Fig. 6·7. While we can detect resonant thermal motion with high fidelity, the detection noise ($\sim 5 \times 10^{-13}$ m/$\sqrt{\text{Hz}}$) obscures the off-resonance thermal fluctuations. At the opposite end of its dynamic range, our displacement read-out stays linear up to a RMS tip amplitude of 250 nm. We confirm that our optical transducer remains linear in the explored parameter space. The saturation of the optical read-out is shown in Figure 6·8, where the cantilever is resonantly driven to a known amplitude using a calibrated piezo-shaker.

We emphasize that we are not concerned with the particulars of the flow in this

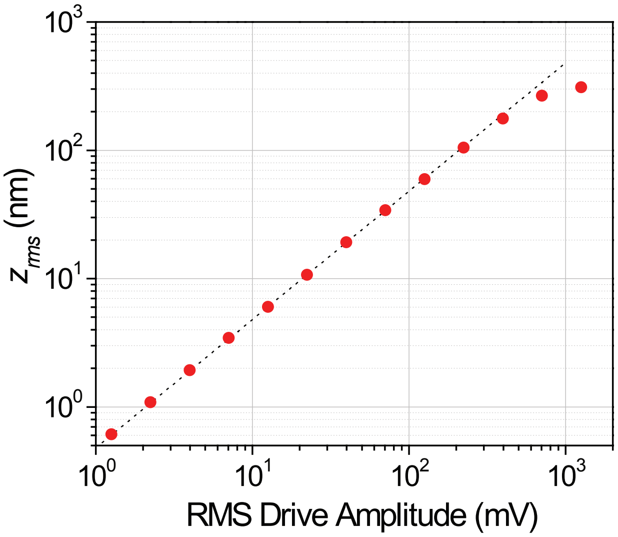

Figure 6·8: Calibrated RMS displacement of the cantilever tip under sinusoidal drive. The optical read-out remains linear up to displacements of $\sim$ 250 nm.

non-ideal channel. The non-idealities include significant surface roughness ($r/D \sim 0.001$ where r is the RMS roughness), wall asperities, and so on. The main comparison in this study comes from changing the inlet conditions while keeping everything else (including the non-idealities) the same, i.e., cases (i) and (ii).

6.3.1 Pressure Drop

The pressure drop Δp between the inlet and outlet of the micro-channel as a function of the Reynolds number is shown in Figure 6·9(a) on log-log axes. Figure 6·9(b) shows the same data on linear axes in a limited range near the origin. The pressure drop in case (ii) is systematically larger than that in case (i) at a given Re. The difference can be attributed to the pressure drop in the mesh. In the low Reynolds number range $0 \leq \mathrm{Re} \lesssim 10^3$, the pressure drop in case (i) can be fit to that in a Poiseuille flow using the nominal microchannel parameters with no free parameters (Bruus, 2008). This is the asympote (dashed line) in Figure 6·9. In the high Re regime, the data appears to converge to another asymptote (dotted line). This asymptote is based on the

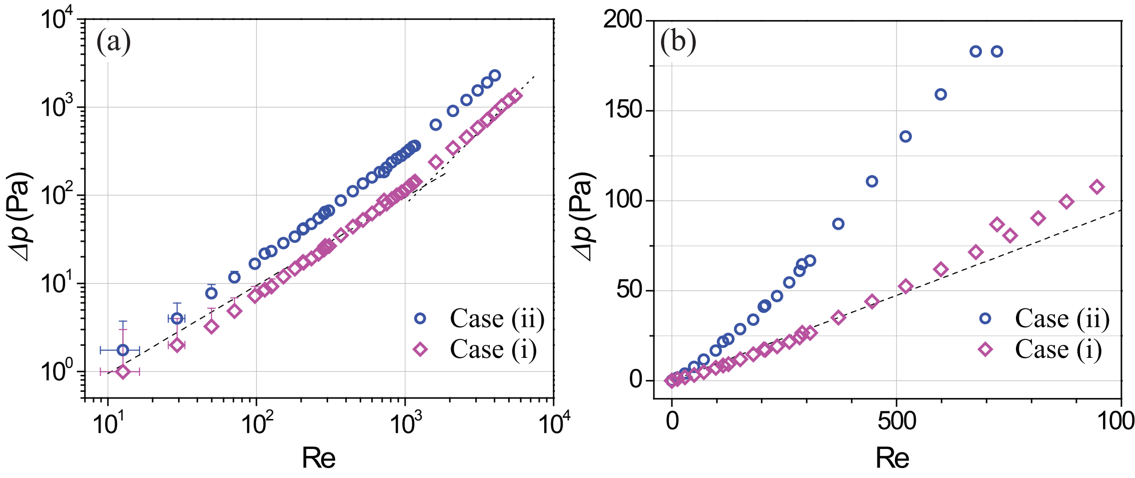

Figure 6·9: (a) Double logarithmic plot of pressure drop Δp as a function of Reynolds number in the channel. Lines are fits to laminar (dashed) and Blasius (dotted) flow models with the transition around 2×10^3. (b) The low-Reynolds-number region of the same data plotted on linear axes.

pressure drop calculated from the Colebrook equation in a rectangular duct (Jones, 1976), again using only the experimentally available parameters. Below, we describe these fits in more detail. We note that in both cases (i) and (ii), we do not notice abrupt signatures of transition to turbulence.

The pressure drop in a laminar flow through a channel of rectangular cross-section is approximated in the limit $\frac{H}{W} \to 0$ as

$$\Delta p \approx \frac{12\mu L Q}{H^3 W \left[1 - 0.63\frac{H}{W}\right]}, \text{ for } H < W. \tag{6.16}$$

Here, $Q = UHW$ is the volumetric flow rate. We define $\mathrm{Re} = \frac{UD}{\nu}$ where $D = \frac{2HW}{H+W}$ is the hydraulic diameter and find the pressure drop through the channel in terms of Re as

$$\Delta p \approx \mathrm{Re}\frac{6\mu\nu L}{H^3 W}\frac{H+W}{\left[1 - 0.63\frac{H}{W}\right]}. \tag{6.17}$$

We fit our pressure drop data in Fig. 6·9 for Re $<$ 1000 (dashed line) using this equation and the parameters of our system.

At higher flow rates, when the flow has entered the transition regime, the pressure drop exhibits a different dependence on Re. Here, we calculate the Darcy friction factor f in the channel using an approximation to the Colebrook equation (Jones, 1976);

$$\frac{1}{\sqrt{f}} = 2.0\log_{10}(\mathrm{Re}^*)\sqrt{f} - 0.8, \tag{6.18}$$

where $\mathrm{Re}^* = \mathrm{Re}\phi^*$ is the modified Re for rectangular ducts and $\phi^*\left(\frac{W}{H}\right) = 0.764$ for our channel dimensions. The Darcy friction factor is related to the pressure drop as

$$\Delta p = f\frac{L}{D}\frac{\rho U^2}{2}, \tag{6.19}$$

and reparameterizing,

$$\Delta p = f\nu^2\mathrm{Re}^2\frac{L}{D^3}\frac{\rho}{2}, \tag{6.20}$$

where ρ is the density of air. We plot this function in Fig. 6·9 for $\mathrm{Re} > 1000$ (dotted line).

6.4 Results

We first turn to the spectral properties of the near-wall fluctuations. Flow forces act on the microcantilever and give rise to mechanical fluctuations. The microcantilever has a sharply-peaked resonance at 100 kHz with a linewidth of 500 Hz. Its linear response function is frequency-independent in the frequency range $f < 80$ kHz and can be approximated as $|G(f)| \approx 1/\kappa$, with κ being the cantilever spring constant and $\kappa \approx 3$ N/m. Thus, the linear relation, $S_z(f) \approx S_F(f)/\kappa^2$, between the spectral densities of the force $S_F(f)$ and the cantilever displacement $S_z(f)$ remains valid below $f < 80$ kHz. At very low flow rates ($\mathrm{Re} \lesssim 800$), $S_z(f)$ becomes obscured by the measurement noise because the flow cannot generate detectable cantilever motion.

$S_z(f)$ obtained under the two inlet conditions is shown at different Reynolds num-

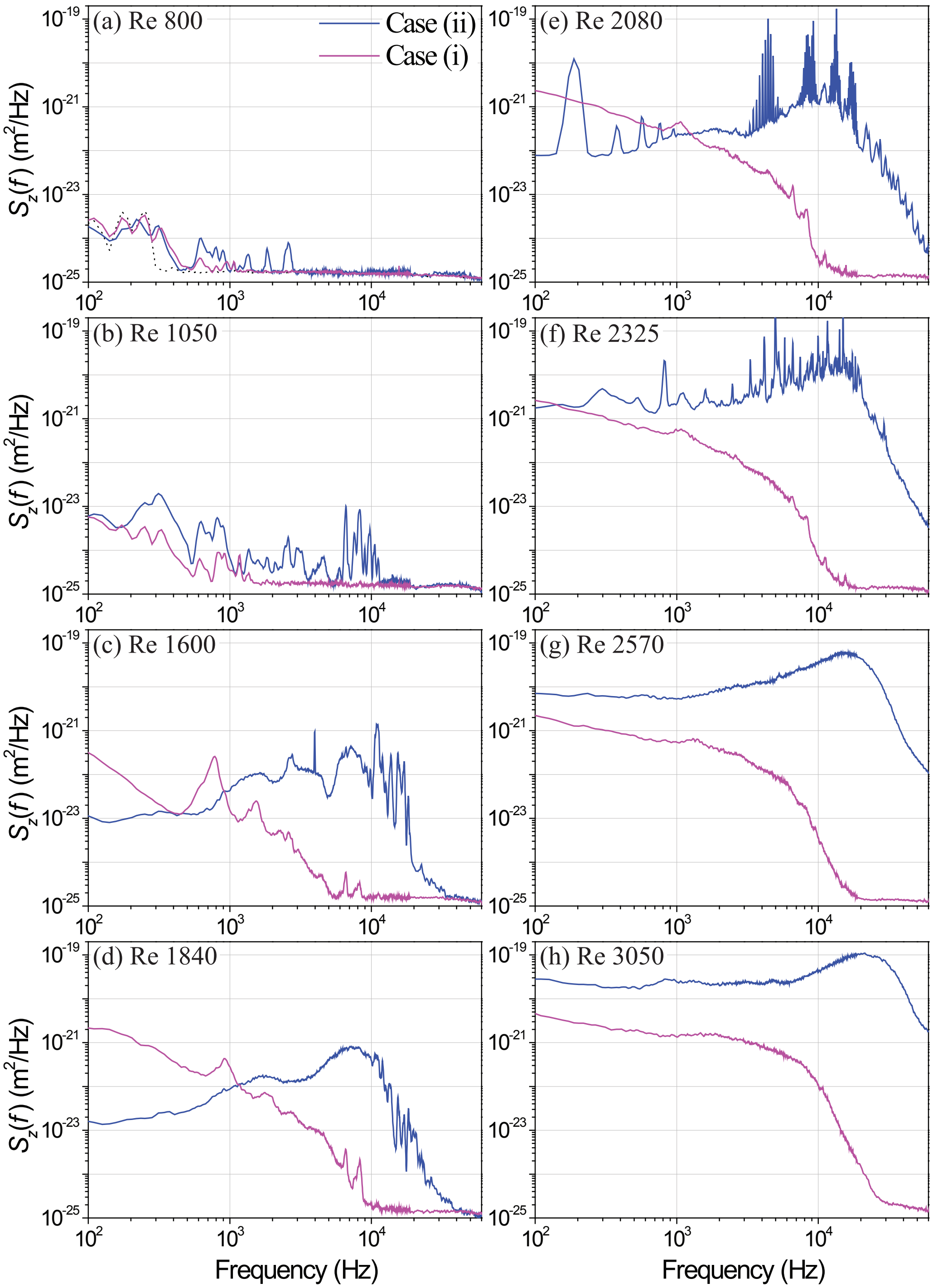

Figure 6·10: Power spectral density $S_z(f)$ of cantilever displacements for different Reynolds numbers for cases (i) and (ii). The dotted line in (a) shows the noise floor of the measurement; the noise floor remains flat for the frequency range $f \geq 300$ Hz.

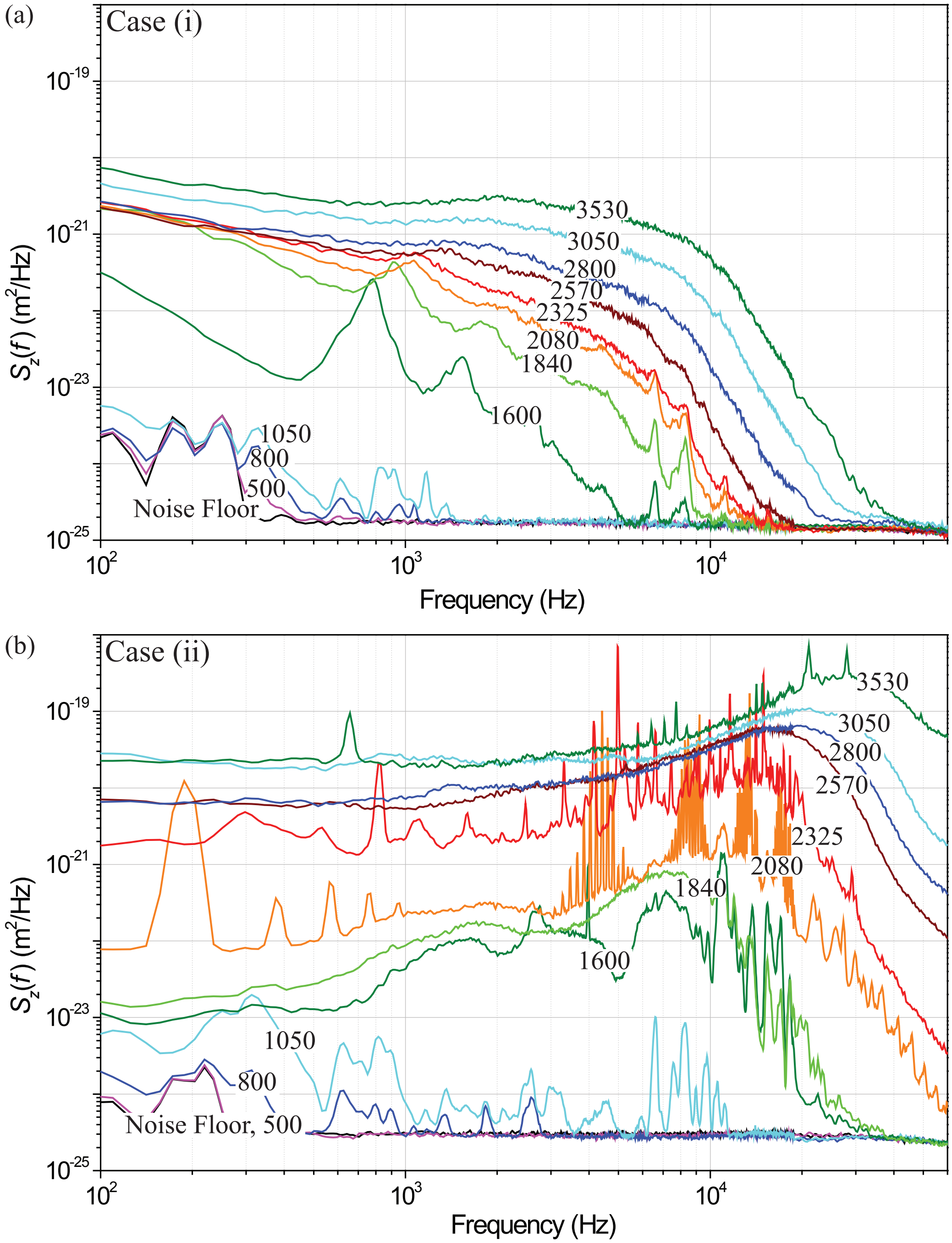

Figure 6·11: Power spectral density $S_z(f)$ of cantilever displacements for different Reynolds numbers for cases (i) (a) and (ii) (b).

bers in Figure 6·10. The same data is shown for all Reynolds numbers measured in this study on single plots for cases (i) and (ii) in Figure 6·11. At $\mathrm{Re} = 800$ (Fig. 6·10(a)), the spectra for both cases are barely above the noise floor (dotted black line) and appear similar for the most part. At $\mathrm{Re} = 1050$ (Fig. 6·10 (b)), one notices some high-frequency peaks in case (ii) around 10^4 Hz. For $\mathrm{Re} \geq 1600$ (Fig. 6·10(c)-(h)), there are dramatic differences between the two cases, especially in the frequency range $f \geq 10^3$ Hz. First, the intensity of the high-frequency fluctuations in case (ii) is larger than that in case (i) by a few orders of magnitude. Second, around the transition $1600 \lesssim \mathrm{Re} \lesssim 2100$, one sees distinct sharp peaks in case (ii) — absent in case (i). When $\mathrm{Re} \approx 2600$ is reached (Fig. 6·10(g)), these sharp peaks disappear and both data traces look smooth.

The sharp peaks observed in case (ii) must correspond to propagating modes triggered by the mesh at the inlet, because they are not present in case (i). Let us provide some estimates using Landau theory. Because of the geometry, we assume that the perturbation is of the form $\mathbf{v} = e^{i(kx-\Omega t)}\mathbf{f}(y,z)$ with $\Omega(k) = \omega(k) + i\gamma(k)$ around $\mathrm{Re}_{\mathrm{cr}}$. The first few unstable modes (traveling waves) satisfy $\partial_k \gamma \approx 0$, and their temporal frequency can be estimated as $\omega(k) \approx kU$, where the average velocity U is taken as the group velocity. Then, $f = \frac{\omega}{2\pi} \sim \frac{U}{H}$. This is because the channel height H is the only finite length scale in the problem, and the wavelength of the first unstable mode should be $\mathcal{O}(H)$. With $U \approx 10 - 20$ m/s in the range $1000 \lesssim \mathrm{Re} \lesssim 2100$, we expect $f \approx 10^4 - 2\times 10^4$ Hz with $H \approx 10^{-3}$ m. This estimate is in good agreement with the peaks observed in Fig. 6·10. The fact that the inlet perturbations can propagate so far downstream even in low-Reynolds-number flows is somewhat surprising and agrees with observations of long life-times of fluctuations (Hof et al., 2006).

Next, we turn to the statistical properties of near-wall fluctuations. We collect a long-time trace of the cantilever amplitude filtered in the frequency range 100 Hz <

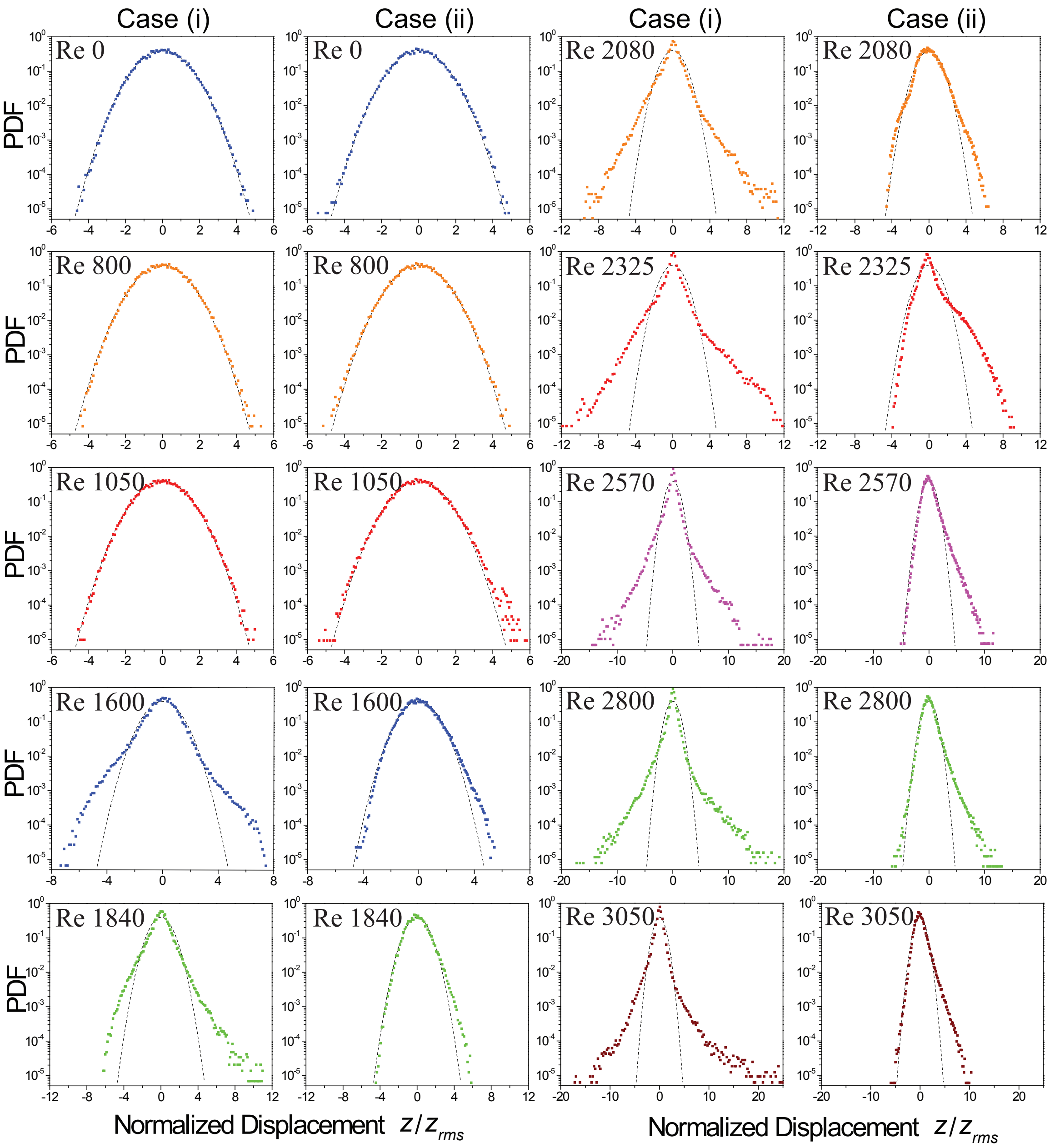

Figure 6·12: PDFs for different Reynolds numbers for cases (i) and (ii). Note that the x-axes are in normalized units of z_{rms}, which are different for each data set (see Table 6.1).

$f < 30$ kHz to remove the high-frequency resonant oscillations. We then sample the time data every 3 μs, obtaining $\sim 10^6$ data points. Because we are interested in a single-point probability density function (PDF), we do not worry about over-sampling in comparison to other relaxation times in the measurement, e.g., the ring-down time of the cantilever. The PDFs for different Reynolds numbers are plotted in Fig. 6·12, and the calculated moments are displayed in Table 6.1 for cases (i) and (ii). It is revealing to interpret the PDFs in Fig. 6·12 in light of the spectra already presented in Fig. 6·10. For $\mathrm{Re} \lesssim 800$, our measurement is dominated by technical noise, and the PDFs in both cases (i) and (ii) are perfectly Gaussian (dashed line in the figure). The PDFs for a slightly higher Reynolds number, $\mathrm{Re} = 1050 < \mathrm{Re}_{\mathrm{cr}}$ show no substantial modification in case (i), but a slight asymmetry and deviation from Gaussianity is noticeable in case (ii), consistent with the first appearance of the sharp peaks in the spectra in Fig. 6·10(b). In the range $1600 \lesssim \mathrm{Re} \lesssim 2300$, both PDFs go through dramatic changes. First, one notices a substantial broadening of the tails of the PDF in case (i), indicating the presence of strong wall velocity/pressure bursts, which may reach the bulk (Yakhot et al., 2010). Here, the PDFs in case (i) cannot be fit to a Gaussian, even at very small displacements; an exponential decay seems more appropriate. The PDFs observed in case (ii) for $1600 \lesssim \mathrm{Re} \lesssim 2300$ suggest that the broadband fluctuations coming from the inlet are somwehat homogenous, but wall bursts make the PDFs more asymmetric and intermittent. This trend continues with increasing Reynolds number. The observations from Figs. 6·10, 6·11, and 6·12 can be summarized as follows. The random flow in case (i) is more intermittent compared to case (ii); however, the intensity of fluctuations in case (ii) is much larger. This effect can also be clearly seen in the normalized moments listed in Table 6.1. Based upon these observations, it may not be incorrect to conclude that these are two very different random flows, generated by different mechanisms.

Re	$\langle z^2\rangle^{1/2}$ (nm) (i)	$\langle z^2\rangle^{1/2}$ (nm) (ii)	$\frac{\langle z^4\rangle}{\langle z^2\rangle^2}$ (i)	$\frac{\langle z^4\rangle}{\langle z^2\rangle^2}$ (ii)	$\frac{\langle z^6\rangle}{\langle z^2\rangle^3}$ (i)	$\frac{\langle z^6\rangle}{\langle z^2\rangle^3}$ (ii)	$\frac{\langle z^8\rangle}{\langle z^2\rangle^4}$ (i)	$\frac{\langle z^8\rangle}{\langle z^2\rangle^4}$ (ii)
0	0.07	0.07	2.99	3.07	14.9	16.1	104	118
800	0.07	0.07	2.99	3.08	15.0	16.1	106	118
1050	0.08	0.14	3.00	3.18	15.1	17.8	107	147
1600	0.25	1.68	5.61	3.35	81.5	20.8	1894	198
2080	0.97	8.36	8.75	3.89	261	32.8	15381	445
2325	1.13	23.0	13.7	9.08	654	192	60383	5926
2570	1.46	28.6	20.7	6.69	2842	158	1.0×10^6	7334
2800	1.79	31.4	31.2	7.09	5962	212	2.4×10^6	13960
3050	2.82	43.8	48.5	6.34	20084	133	1.4×10^7	5164

Table 6.1: Moments.

We now turn to the lowest order moment or the r.m.s displacement of the cantilever, $z_{rms} = \langle z^2\rangle^{1/2}$ (brackets indicate averaging), as a function of Reynolds number, shown in Fig. 6·13. The dashed lines are fits to our proposed equation, as discussed below. The z_{rms} values are obtained from measurements of the time traces of the cantilever tip position $z(t)$ filtered in the frequency range 100 Hz $\leq f \leq$ 30 kHz. There are three regions in the plot marked with different shadings. The first region, Re $\lesssim$ 800, is dominated by technical noise and does not provide any insight. In the second region (blue) where $1000 \lesssim \text{Re} \lesssim 1600$, the magnitude of the cantilever fluctuations are of the same order for both case (i) and (ii), $z_{rms} \sim 1$ nm. This suggests that perturbations at the inlet do not propagate efficiently near the wall and make it to the test section ($x \approx 11D$) — even though they may be convected in the bulk. In the third region (pink) where Re $\gtrsim$ 2000, the inlet perturbations reach efficiently to the wall. The observed RMS amplitude of near-wall fluctuations in case (ii) are significantly larger than those in case (i). It is surprising that near-wall fluctuations

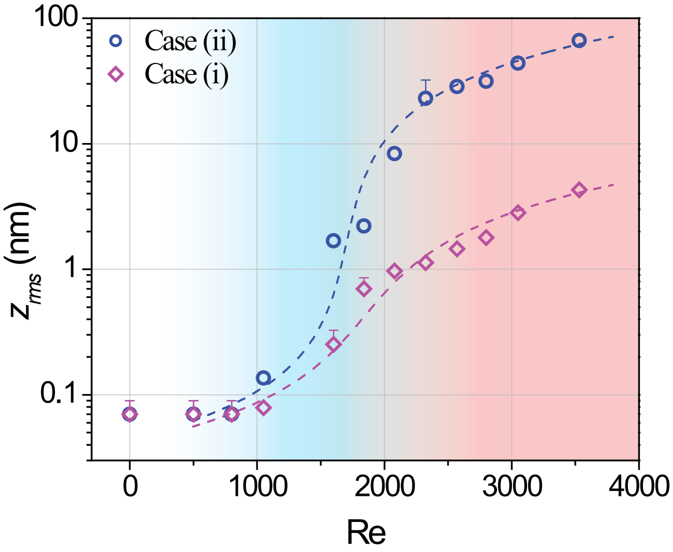

Figure 6·13: RMS displacement of the cantilever, z_{rms}, versus Re for cases (i) and (ii). Dashed lines are fits to the noisy Landau Equation, Eq. (6.15), with fit parameters in Table 6.2.

are strongly affected by the inlet conditions even in this relatively long channel. The slope changes for both data traces around Re $\approx$ 2000, suggesting the onset of more sustained perturbations. The data traces appear to increase parallel to each other for Re $\gtrsim$ 2000. The similarities in the two data traces in Fig. 6·13 suggest that there may be common underlying physics to both cases.

6.5 Discussion

The obtained results can be used to quantitatively explain the experimental data of Fig. 6·13. The time-dependent force acting on the cantilever is

$$\mathbf{F} = F\hat{\mathbf{z}} = -\int_S p_1 \cdot \mathbf{n} dS \approx \frac{\partial p_1}{\partial z} V \hat{\mathbf{z}}, \tag{6.21}$$

where $\hat{\mathbf{z}}$ is the unit vector, and V is the volume of the cantilever. We simplify the problem by approximating our microchannel as a long and wide rectangular (planar) duct and, neglecting noise, write the perturbation equation in the z direction from

Eq. (6.9) as

$$\frac{1}{\rho}\frac{\partial p_1}{\partial z} = -\frac{\partial v_z}{\partial t} - \frac{3}{2}U\left(1-\frac{4z^2}{H^2}\right)\frac{\partial v_z}{\partial x} + \nu\nabla^2 v_z + \mathcal{O}(\frac{\partial v^2}{\partial z}). \tag{6.22}$$

In close proximity to the wall, $z \approx H/2$, and the second term on the right hand side of Eq. (6.22) is small. Numerical simulations (Lee et al., 2004), in which statistics of acceleration in close proximity to a wall was studied, suggest that bursts are dominated by the z-component of the velocity ($v^2 = \mathcal{O}({v_z}^2)$) and the viscous term is unimportant. We therefore write

$$\frac{1}{\rho}\frac{\partial p_1}{\partial z} \approx -\frac{\partial v_z}{\partial t} + \mathcal{O}(\frac{\partial {v_z}^2}{\partial z}). \tag{6.23}$$

Here, $\partial_t v_z = \mathcal{O}(v_z U/H)$. To find an order of magnitude estimate for $\partial_z({v_z}^2)$, we extrapolate the results of (Yakhot et al., 2010), which shows that, for $\mathrm{Re} < 10^5$, the velocity of wall bursts are $v_z = \mathcal{O}(U/10)$. This means that the magnitude of the two terms on the right hand side of Eq. (6.23) are comparable and $\mathcal{O}({v_z}^2)$ must be accounted for. Thus, we deduce $\partial_z p_1 = \mathcal{O}({v_z}^2/H)$ and write

$$z_{rms} \sim \frac{\rho V {v_z}^2}{\kappa H} \propto |A(\infty)|^2, \tag{6.24}$$

where $|A(\infty)|^2 = {A_\mathrm{e}}^2$ as in Eq. (6.15). This exercise provides the fits (dashed lines) shown in Fig. 6·13 with the parameters in Table 6.2. The ultimate justification for the above arguments comes from the agreement between experiment and theory in Fig. 6·13. The following simple order of magnitude estimate further bolsters our confidence in our theory. Assuming that ${v_z}^2/U^2 \approx 0.008$ around Re_cr (Yakhot et al., 2010) and using the experimentally available parameters ($V \approx 2\times10^{-14}$ m^3, $H \approx 10^{-3}$ m, $\kappa \approx 3$ N/m), we find $z_{rms} \approx 10^{-10}$ m, close to the experimentally observed value.

Our results point to two very different paths to turbulence. In the the first, wall effects (wall roughness and channel imperfections) lead to an extremely intermittent

	$\mathrm{Re}_{\mathrm{cr}}$	γ_1/α ($\mathrm{m}^2/\mathrm{s}^2$)	$\overline{\phi^2}/\alpha$ ($\mathrm{m}^4/\mathrm{s}^4$)
Case (i)	1850	$0.14 \times (\mathrm{Re} - \mathrm{Re}_{\mathrm{cr}})$	2.37×10^3
Case (ii)	1700	$1.92 \times (\mathrm{Re} - \mathrm{Re}_{\mathrm{cr}})$	3.28×10^4

Table 6.2: Noisy Landau Fit Parameters.

transitional flow, probably dominated by a few unstable modes. The exponential PDF resembles the PDF observed in Bénard convection in the hard turbulence regime dominated by the plumes emitted from the unstable thermal boundary layer (Castaing et al., 1989). In the second, bursts coming from the wall are modulated by powerful broadband fluctuations originating at the inlet. The resulting flow is less intermittent and resembles homogeneous turbulence; the interaction between the wall and the inlet disturbances is quite strong. Remarkably, the lowest order statistics of the these two different flows with distinctly different noise sources are well-described by the noisy Landau equation. The applicability of the noisy Landau equation to both cases is due to the fact that the noise term is taken to be at high frequencies as compared to the slow mode in question. In other words, the noise can come from any natural or artificial source as long as the stirring of the fluid occurs at high frequencies. In typical experiments (including ours), this is an accurate statement. Microscopic surface asperities, for instance, are at high spatial frequency compared to any length scales of the flow. Similarly, perturbations from the inlet generate high-frequency waves, which can also be incorporated into the noise term, as shown here. Along the same lines, we believe that even thermal fluctuations in the fluid would likely result in a similar regularization of the Landau equation. The phenomena observed here may have important consequences for heat and mass transfer in wall-bounded flows.

Chapter 7

Conclusion

In this thesis study we have conducted nanomechanical measurements of fluctuations in biological, turbulent, and confined flows. We employed silicon cantilevers as sensitive transducers to probe these fluctuations and to uncover underlying physical phenomena. The results presented have implications for many physical systems. Here, we review our results and discuss opportunities for future work.

In Chapter 3 we presented multiple methods that can be used to estimate modal mass in resonant mechanical systems. In the thermal noise method, we measured the thermomechanical fluctuations of a cantilever and related its modal energy to its modal mass. In the gas damping method, we measured the quality factor of a cantilever's resonance at various pressures. We demonstrated how this measurement could be used to obtain an independent mass calibration. Our experiments showed that gas dissipation measurements provided accurate results and that they could serve as a suitable alternative to the more traditional thermal noise calibration method. In addition, these measurements were easier to perform because they relied on the driven system response rather than the thermomechanical motion.

In Chapter 4 we studied dissipation in a spatially confined oscillatory flow using a microcantilever positioned in the proximity of a wall. We presented experimental data that covered a broad range of flow parameters including the gas pressure, the device frequency, and the gap between the cantilever and the nearby wall. Using our experimental results and physical intuition, we developed a scaling function which was able to describe the flow in the entire parameter space without explicitly imposing an effective viscosity or a slip length at the wall. In all of the cases studied, the dimensionless Weissenberg number remained small, $\mathrm{Wi} = \omega\tau \ll 1$. Further experimental and theoretical work can be done to measure flows in the interval $\mathrm{Wi} \gg 1$ and to generalize our theory of confined nanoflows. In addition, it would be interesting to repeat the experiments using a different gas. This may shed light on how the interactions between the gas molecules and the surface of the cantilever change with the molecular mass and the thermal velocity in a confined system.

In Chapter 5 we studied fluctuations driven by the activity of motile bacteria. Once again, we used a microcantilever as our experimental probe. We observed an increase in the amplitude of the cantilever's fluctuations as we increased the concentration of bacteria adhered to the cantilever's surface. We also administered antibiotics to kill the bacteria and observed the cessation of these fluctuations. A spectral analysis of the fluctuations of *E. coli* bacteria showed that their collective motion on the cantilever was broad in spectrum and focused at low frequencies with a $1/f^{\alpha}$-type power law. We presented a simple model to explain these observations. Our results lay the foundation for further development of this technology as a diagnostic tool. Current biosensing approaches are not able to monitor bacterial motion and bacterial susceptibility to antibiotics in real-time. The cantilever-based approach presented here has the potential to serve as the central component of a robust, inexpensive, and real-time system for bacterial monitoring. If the optical measurements can be scaled down, it should be possible to construct a portable diagnostic tool.

In Chapter 6 we measured fluctuations in a transitional channel flow. In particular, we studied the transition to turbulence in two different cases in the same channel. In the first case, the transition was triggered by the natural imperfections of the channel walls. In the second case, the transition was triggered by a flexible wire mesh at the channel inlet. Each of the cases resulted in final turbulent states in which high-order moments of near-wall fluctuations differed by orders of magnitude. Despite this, the lowest order statistics were qualitatively similar between experiments and each could be described by a proposed noisy Landau equation. Our results here provide evidence of a finite turbulent relaxation time in transitional flows due to the persistent nature of noise in these systems. Many future studies can be devised to follow up on the results of this work. An ideal study would center around a microchannel with walls of roughness that can be carefully tuned. This would allow the experiment to be repeated and for the noisy Landau equation to be systematically tested for a larger variety of roughness-induced disturbances in the flow. Additionally, it would be interesting and physically important to understand the flow conditions necessary for perturbations originating at one channel wall to cross the channel, rather than to decay or remain near the wall. An experiment could be devised in which sensors are mounted on opposing channel walls and measurements of their fluctuations are cross-correlated. Our results also may have important consequences for heat and mass transfer in wall-bounded flows.

We see from the above studies that fluctuations in physical systems can reveal interesting information about the underlying physics governing these systems. Our hope is that through the experiments and theoretical analyses presented here, we have provided new insights into fluctuations in confined, turbulent, and biological flows and have opened new pathways for further studies.

References

Ahmed, N., Nino, D. F., and T., M. V. (2001). Measurement of solution viscosity by atomic force microscopy. *Review of Scientific Instruments*, 72(6):2731–2734.

Albrecht, T. R., Grütter, P., Horne, D., and Rugar, D. (1991). Frequency modulation detection using high-Q cantilevers for enhanced force microscope sensitivity. *Journal of Applied Physics*, 69(2):668–673.

Alexander, S., Hellemans, L., Marti, O., Schneir, J., Elings, V., Hansma, P. K., Longmire, M., and Gurley, J. (1989). An atomic-resolution atomic-force microscope implemented using an optical lever. *Journal of Applied Physics*, 65(1):164–167.

Arkilic, E. B., Breuer, K. S., and Schmidt, M. A. (2001). Mass flow and tangential momentum accommodation in silicon micromachined channels. *Journal of Fluid Mechanics*, 437:29–43.

Arlett, J. L., Myers, E. B., and Roukes, M. L. (2011). Comparative advantages of mechanical biosensors. *Nature Nanotechnology*, 6(4):203–215.

Arnoldi, M., Fritz, M., Bäuerlein, E., Radmacher, M., Sackmann, E., and Boulbitch, A. (2000). Bacterial turgor pressure can be measured by atomic force microscopy. *Physical Review E*, 62(1):1034–1044.

Azak, N. O., Shagam, M. Y., Karabacak, D. M., Ekinci, K. L., Kim, D. H., and Jang, D. Y. (2007). Nanomechanical displacement detection using fiber-optic interferometry. *Applied Physics Letters*, 91(9):093112.

Bao, G. and Suresh, S. (2003). Cell and molecular mechanics of biological materials. *Nature Materials*, 2:715–725.

Bao, M., Yang, H., Yin, H., and Sun, Y. (2002). Energy transfer model for squeeze-film air damping in low vacuum. *Journal of Micromechanics and Microengineering*, 12(3):341.

Bhiladvala, R. B. and Wang, Z. J. (2004). Effect of fluids on the Q factor and resonance frequency of oscillating micrometer and nanometer scale beams. *Physical Review E*, 69(3):036307.

Bowles, A. P. and Ducker, W. A. (2011). Gas flow near a smooth plate. *Physical Review E*, 83(5):056328.

Brenner, H. (1961). The slow motion of a sphere through a viscous fluid towards a plane surface. *Chemical Engineering Science*, 16(3):242–251.

Bruus, H. (2008). *Theoretical Microfluidics*. Oxford University Press, New York.

Burg, T. P., Godin, M., Knudsen, S. M., Shen, W., Carlson, G., Foster, J. S., Babcock, K., and Manalis, S. R. (2007). Weighing of biomolecules, single cells and single nanoparticles in fluid. *Nature*, 446:1066–1069.

Butt, H. J. and Jaschke, M. (1995). Calculation of thermal noise in atomic force microscopy. *Nanotechnology*, 6(1):1.

Callegan, M. C., Kane, S. T., Cochran, D. C., Novosad, B., Gilmore, M. S., Gominet, M., and Lereclus, D. (2005). *Bacillus* endophthalmitis: Roles of bacterial toxins and motility during infection. *Investigative Ophthalmology and Visual Science*, 46(9):3233–3238.

Callen, H. B. and Welton, T. A. (1951). Irreversibility and generalized noise. *Physical Review*, 83(1):34.

Castaing, B., Gunaratne, G., Heslot, F., Kadanoff, L., Libchaber, A., Thomae, S., Wu, X. Z., Zaleski, S., and Zanetti, G. (1989). Scaling of hard thermal turbulence in Rayleigh-Bénard convection. *Journal of Fluid Mechanics*, 204:1–30.

Chadwick, R. S. and Liao, Z. (2008). High-frequency oscillations of a sphere in a viscous fluid near a rigid plane. *SIAM Review*, 50(2):313–322.

Christian, R. G. (1966). The theory of oscillating-vane vacuum gauges. *Vacuum*, 16(4):175–178.

Cleland, A. N. (2003). *Foundations of Nanomechanics: From Solid-State Theory to Device Applications*. Springer-Verlag, Berlin.

Cleland, A. N. and Roukes, M. L. (1998). A nanometre-scale mechanical electrometer. *Nature*, 392:160–162.

Darbyshire, A. G. and Mullin, T. (1995). Transition to turbulence in constant-mass-flux pipe flow. *Journal of Fluid Mechanics*, 289:83–114.

D'Costa, V. M., King, C. E., Kalan, L., Morar, M., Sung, W. W. L., Schwarz, C., Froese, D., Zazula, G., Calmels, F., Debruyne, R., Golding, G. B., Poinar, H. N., and Wright, G. D. (2011). Antibiotic resistance is ancient. *Nature*, 477(7365):457–461.

Dutta, P. and Horn, P. M. (1981). Low-frequency fluctuations in solids: 1/f noise. *Reviews of Modern Physics*, 53(3):497.

Ekinci, K. L., Karabacak, D. M., and Yakhot, V. (2008). Universality in oscillating flows. *Physical Review Letters*, 101(26):264501.

Ekinci, K. L. and Roukes, M. L. (2005). Nanoelectromechanical systems. *Review of Scientific Instruments*, 76(6):061101.

Ekinci, K. L., Yakhot, V., Rajauria, S., Colosqui, C., and Karabacak, D. M. (2010). High-frequency nanofluidics: a universal formulation of the fluid dynamics of MEMS and NEMS. *Lab on a Chip*, 10(22):3013–3025.

Ekinci, K. L., Yang, Y. T., and Roukes, M. L. (2004). Ultimate limits to inertial mass sensing based upon nanoelectromechanical systems. *Journal of Applied Physics*, 95(5):2682–2689.

Fox, M. (2006). *Quantum Optics*. Oxford University Press, New York.

Frauenfelder, H., Wolynes, P. G., and Austin, R. H. (1999). Biological physics. *Reviews of Modern Physics*, 71:S419–S430.

Gfeller, K. Y., Nugaeva, N., and Hegner, M. (2005). Micromechanical oscillators as rapid biosensor for the detection of active growth of *Escherichia coli*. *Biosensors and Bioelectronics*, 21(3):528–533.

Hauer, B. D., Doolin, C., Beach, K. S. D., and Davis, J. P. (2013). A general procedure for thermomechanical calibration of nano/micro-mechanical resonators. *Annals of Physics*, 339:181–207.

Hausdorff, J. M. and Peng, C. K. (1996). Multiscaled randomness: A possible source of 1/f noise in biology. *Physical Review E*, 54(2):2154.

Hof, B., Westerweel, J., Schneider, T. M., and Eckhardt, B. (2006). Finite lifetime of turbulence in shear flows. *Nature*, 443(7107):59–62.

Honig, C. D., Sader, J. E., Mulvaney, P., and Ducker, W. A. (2010). Lubrication forces in air and accommodation coefficient measured by a thermal damping method using an atomic force microscope. *Physical Review E*, 81(5):056305.

Hosaka, H., Itao, K., and Kuroda, S. (1995). Damping characteristics of beam-shaped micro-oscillators. *Sensors and Actuators A: Physical*, 49:87– 95.

Inci, F., Tokel, O., Wang, S., Gurkan, U. A., Tasoglu, S., Kuritzkes, D. R., and Demirci, U. (2013). Nanoplasmonic quantitative detection of intact viruses from unprocessed whole blood. *ACS Nano*, 7(6):4733–4745.

Jiang, G., Giannone, G., Critchley, D. R., Fukumoto, E., and Sheetz, M. P. (2003). Two-piconewton slip bond between fibronectin and the cytoskeleton depends on talin. *Nature*, 424:334–337.

Jones, O. C. (1976). An improvement in the calculation of turbulent friction in rectangular ducts. *Journal of Fluids Engineering*, 98(2):173–180.

Karabacak, D., Kouh, T., Huang, C. C., and Ekinci, K. L. (2006). Optical knife-edge technique for nanomechanical displacement detection. *Applied Physics Letters*, 88(19):193122.

Karabacak, D. M. (2008). *Resonant Operation of Nanoelectromechanical Systems in Fluidic Environments*. PhD thesis, Boston University.

Karabacak, D. M., Yakhot, V., and Ekinci, K. L. (2007). High-frequency nanofluidics: An experimental study using nanomechanical resonators. *Physical Review Letters*, 98(25):254505.

Karniadakis, G., Beskok, A., and Aluru, N. (2005). *Microflows and Nanoflows: Fundamentals and Simulation*. Springer, New York.

Kasas, S., Ruggeri, F. S., Benadiba, C., Maillard, C., Stupar, P., Tournu, H., Dietler, G., and Longo, G. (2015). Detecting nanoscale vibrations as signature of life. *Proceedings of the National Academy of Sciences*, 112(2):378–381.

Khosrofian, J. M. and Garetz, B. A. (1983). Measurement of a Gaussian laser beam diameter through the direct inversion of knife-edge data. *Applied Optics*, 22(21):3406–3410.

Kim, S. and Karrila, S. J. (1991). *Microhydrodynamics: Principles and Selected Applications*. Butterworth-Heinemann, Boston.

Kouh, T., Kemiktarak, U., Basarir, O., Lissandrello, C., and Ekinci, K. L. (2014). Measuring gaussian noise using a lock-in amplifier. *American Journal of Physics*, 82(8):778–784.

Labuda, A., Bates, J. R., and Grütter, P. H. (2012). The noise of coated cantilevers. *Nanotechnology*, 23(2):025503.

Landau, L. D. and Lifshitz, E. M. (1987). *Fluid Mechanics*. Butterworth-Heinemann, Oxford.

Lauga, E. and Powers, T. R. (2009). The hydrodynamics of swimming microorganisms. *Reports on Progress in Physics*, 72(9):096601.

Laurent, J., Drezet, A., Sellier, H., Chevrier, J., and Huant, S. (2011). Large variation in the boundary-condition slippage for a rarefied gas flowing between two surfaces. *Physical Review Letters*, 107(16):164501.

Lavrik, N. V., Sepaniak, M. J., and Datskos, P. G. (2004). Cantilever transducers as a platform for chemical and biological sensors. *Review of Scientific Instruments*, 75(7):2229–2253.

Lawall, J. and Kessler, E. (2000). Michelson interferometry with 10 pm accuracy. *Review of Scientific Instruments*, 71(7):2669–2676.

Lawall, J., Pedulla, J. M., and Le Coq, Y. (2001). Ultrastable laser array at 633 nm for real-time dimensional metrology. *Review of Scientific Instruments*, 72(7):2879–2888.

Lee, C., Yeo, K., and Choi, J. I. (2004). Intermittent nature of acceleration in near wall turbulence. *Physical Review Letters*, 92(14):144502.

Lee, E. J., Kim, C. S., Park, Y. D., and Kouh, T. (2011). Pressure-dependent dissipation effect at multiple cantilever resonant modes. *Journal of Nanoscience and Nanotechnology*, 11(7):6599–6602.

Lee, E. J., Park, Y., Kim, C. S., and Kouh, T. (2010). Detection sensitivity of the optical beam deflection method characterized with the optical spot size on the detector. *Current Applied Physics*, 10(3):834–837.

Lifshitz, E. M. and Pitaevskii, L. P. (1981). *Physical Kinetics*. Butterworth-Heinemann, Oxford.

Lissandrello, C., Inci, F., Francom, M., Paul, M. R., Demirci, U., and Ekinci, K. L. (2014). Nanomechanical motion of *Escherichia coli* adhered to a surface. *Applied Physics Letters*, 105(11):113701.

Lissandrello, C., Yakhot, V., and Ekinci, K. L. (2012). Crossover from hydrodynamics to the kinetic regime in confined nanoflows. *Physical Review Letters*, 108(8):084501.

Longo, G., Alonso-Sarduy, L., Rio, L. M., Bizzini, A., Trampuz, A., Notz, J., Dietler, G., and Kasas, S. (2013). Rapid detection of bacterial resistance to antibiotics using AFM cantilevers as nanomechanical sensors. *Nature Nanotechnology*, 8(7):522–526.

Longo, G. and Kasas, S. (2014). Effects of antibacterial agents and drugs monitored by atomic force microscopy. *Wiley Interdisciplinary Reviews: Nanomedicine and Nanobiotechnology*, 6(3):230–244.

Maali, A. and Bhushan, B. (2008). Slip-length measurement of confined air flow using dynamic atomic force microscopy. *Physical Review E*, 78(2):027302.

Mani, V., Wang, S., Inci, F., De Libero, G., Singhal, A., and Demirci, U. (2014). Emerging technologies for monitoring drug-resistant tuberculosis at the point-of-care. *Advanced Drug Delivery Reviews*, 78:105–117.

McComb, W. D., Linkmann, M. F., Berera, A., Yoffe, S. R., and Jankauskas, B. (2014). Self-organization and transition to turbulence at low Reynolds numbers in randomly forced isotropic fluid motion. arXiv:1410.2987 [physics.flu-dyn].

Meyer, G. and Amer, N. M. (1988). Novel optical approach to atomic force microscopy. *Applied Physics Letters*, 53(12):1045–1047.

Meyer, G. and Amer, N. M. (1990). Simultaneous measurement of lateral and normal forces with an optical-beam-deflection atomic force microscope. *Applied Physics Letters*, 57(20):2089–2091.

Moffitt, J. R., Chemla, Y. R., Smith, S. B., and Bustamante, C. (2008). Recent advances in optical tweezers. *Annual Review of Biochemistry*, 77:205–228.

Ozsun, O. (2014). *Fundamentals and Applications of Fluid-Structure Interactions in Compliant Microchannels*. PhD thesis, Boston University.

Paul, M. R., Clark, M. T., and Cross, M. C. (2006). The stochastic dynamics of micron and nanoscale elastic cantilevers in fluid: fluctuations from dissipation. *Nanotechnology*, 17(17):4502.

Pausch, M. and Eckhardt, B. (2015). Direct and noisy transitions in a model shear flow. arXiv:1502.01897 [physics.flu-dyn].

Pelling, A. E., Sehati, S., Gralla, E. B., Valentine, J. S., and Gimzewski, J. K. (2004). Local nanomechanical motion of the cell wall of *Saccharomyces cerevisiae*. *Science*, 305(5687):1147–1150.

Pfenninger, W. (1961). Transition experiments in the inlet length of tubes at high Reynolds numbers. In Lachman, G. V., editor, *Boundary Layer and Flow Control*, volume 2. Oxford: Pergamon Press.

Procaccia, I. and Gitterman, M. (1981). Slowing down of chemical reactions near thermodynamic critical points. *Physical Review Letters*, 46(17):1163.

Putman, C. A. J., De Grooth, B. G., Van Hulst, N. F., and Greve, J. (1992). A detailed analysis of the optical beam deflection technique for use in atomic force microscopy. *Journal of Applied Physics*, 72(1):6–12.

Radmacher, M., Fritz, M., Hansma, H. G., and Hansma, P. K. (1994). Direct observation of enzyme activity with the atomic force microscope. *Science*, 265(5178):1577–1579.

Ramanathan, S., Koch, D. L., and Bhiladvala, R. B. (2010). Noncontinuum drag force on a nanowire vibrating normal to a wall: Simulations and theory. *Physics of Fluids*, 22(10):103101.

Ramos, D., Tamayo, J., Mertens, J., Calleja, M., and Zaballos, A. (2006). Origin of the response of nanomechanical resonators to bacteria adsorption. *Journal of Applied Physics*, 100(10):106105.

Reynolds, O. (1883). An experimental investigation of the circumstances which determine whether the motion of water shall be direct or sinuous, and of the law of resistance in parallel channels. *Proceedings of the Royal Society of London*, 35(224-226):84–99.

Reynolds, O. (1886). On the theory of lubrication and its application to Mr. Beauchamp Tower's experiments, including an experimental determination of the viscosity of olive oil. *Proceedings of the Royal Society of London*, 40(242-245):191–203.

Sader, J. E., Chon, J. W. M., and Mulvaney, P. (1999). Calibration of rectangular atomic force microscope cantilevers. *Review of Scientific Instruments*, 70(10):3967–3969.

Saleh, B. E. A. and Teich, M. C. (2007). *Fundamentals of Photonics*. John Wiley & Sons, Hoboken.

Saulson, P. R. (1990). Thermal noise in mechanical experiments. *Physical Review D*, 42(8):2437.

Shafiee, H., Jahangir, M., Inci, F., Wang, S., Willenbrecht, R., Giguel, F. F., Tsibris, A., Kuritzkes, D. R., and Demirci, U. (2013). Acute on-chip HIV detection through label-free electrical sensing of viral nano-lysate. *Small*, 9(15):2553–2563.

Shusteff, M., Burg, T. P., and Manalis, S. R. (2006). Measuring Boltzmanns constant with a low-cost atomic force microscope: An undergraduate experiment. *American Journal of Physics*, 74(10):873–879.

Sreenivasan, K. R., Strykowski, P. J., and Olinger, D. J. (1987). Hopf bifurcation, Landau equation, and vortex shedding behind circular cylinders. In Ghia, K. N., editor, *Forum on Unsteady Flow Separation*, volume 52, pages 1–13. American Society of Mechanical Engineers, Fluids Engineering Division.

Stuart, J. T. (1971). Nonlinear stability theory. *Annual Review of Fluid Mechanics*, 3:347–370.

Svitelskiy, O., Sauer, V., Liu, N., Cheng, K. M., Finley, E., Freeman, M. R., and Hiebert, W. K. (2009). Pressurized fluid damping of nanoelectromechanical systems. *Physical Review Letters*, 103(24):244501.

Svitelskiy, O., Sauer, V., Vick, D., Cheng, K. M., Liu, N., Freeman, M. R., and Hiebert, W. K. (2012). Nanoelectromechanical devices in a fluidic environment. *Physical Review E*, 85(5):056313.

Tabeling, P. (2005). *Introduction to Microfluidics*. Oxford University Press, New York.

Thomson, N. H., Fritz, M., Radmacher, M., Cleveland, J. P., Schmidt, C. F., and Hansma, P. K. (1996). Protein tracking and detection of protein motion using atomic force microscopy. *Biophysical Journal*, 70(5):2421–2431.

Timoshenko, S., Young, D. H., and Weaver, W. (1974). *Vibration Problems in Engineering*. John Wiley & Sons, New York.

Tokel, O., Inci, F., and Demirci, U. (2014). Advances in plasmonic technologies for point of care applications. *Chemical Reviews*, 114(11):5728–5752.

Trott, W. M., Castañeda, J. N., Torczynski, J. R., Gallis, M. A., and Rader, D. J. (2011). An experimental assembly for precise measurement of thermal accommodation coefficients. *Review of Scientific Instruments*, 82(3):035120.

Veijola, T., Kuisma, H., and Lahdenperä, J. (1998). The influence of gas-surface interaction on gas-film damping in a silicon accelerometer. *Sensors and Actuators A: Physical*, 66(1):83–92.

Vinogradova, O. I. (1995). Drainage of a thin liquid film confined between hydrophobic surfaces. *Langmuir*, 11(6):2213–2220.

Visick, K. L. and Fuqua, C. (2005). Decoding microbial chatter: Cell-cell communication in bacteria. *Journal of Bacteriology*, 187(16):5507–5519.

Waggoner, P. S. and Craighead, H. G. (2007). Micro-and nanomechanical sensors for environmental, chemical, and biological detection. *Lab on a Chip*, 7(10):1238–1255.

Wagner, J. W. (1990). Optical detection of ultrasound. *Physical Acoustics*, 19:201–266.

Wang, S., Esfahani, M., Gurkan, U. A., Inci, F., Kuritzkes, D. R., and Demirci, U. (2012a). Efficient on-chip isolation of HIV subtypes. *Lab on a Chip*, 12(8):1508–1515.

Wang, S., Inci, F., Chaunzwa, T. L., Ramanujam, A., Vasudevan, A., Subramanian, S., Ip, A. C. F., Sridharan, B., Gurkan, U. A., and Demirci, U. (2012b). Portable microfluidic chip for detection of *Escherichia coli* in produce and blood. *International Journal of Nanomedicine*, 7:2591–2600.

Wang, S., Inci, F., De Libero, G., Singhal, A., and Demirci, U. (2013). Point-of-care assays for tuberculosis: Role of nanotechnology/microfluidics. *Biotechnology Advances*, 31(4):438–449.

Wee, K. W., Kang, G. Y., Park, J., Kang, J. Y., Yoon, D. S., Park, J. H., and Kim, T. S. (2005). Novel electrical detection of label-free disease marker proteins using piezoresistive self-sensing micro-cantilevers. *Biosensors and Bioelectronics*, 20(10):1932–1938.

World Health Organization (2014). *Antimicrobial Resistance: Global Report on Surveillance 2014*. WHO, Geneva, Switzerland.

Wu, C. M., Lawall, J., and Deslattes, R. D. (1999). Heterodyne interferometer with subatomic periodic nonlinearity. *Applied Optics*, 38(19):4089–4094.

Wu, G., Datar, R. H., Hansen, K. M., Thundat, T., Cote, R. J., and Majumdar, A. (2001). Bioassay of prostate-specific antigen (PSA) using microcantilevers. *Nature Biotechnology*, 19(9):856–860.

Yaglom, A. M. (2012). *Hydrodynamic Instability and Transition to Turbulence*. Springer, New York.

Yakhot, V., Bailey, S. C. C., and Smits, A. J. (2010). Scaling of global properties of turbulence and skin friction in pipe and channel flows. *Journal of Fluid Mechanics*, 652:65–73.

Yakhot, V. and Colosqui, C. (2007). Stokes' second flow problem in a high-frequency limit: application to nanomechanical resonators. *Journal of Fluid Mechanics*, 586:249–258.

Yang, Y. T., Callegari, C., Feng, X. L., Ekinci, K. L., and Roukes, M. L. (2006). Zeptogram-scale nanomechanical mass sensing. *Nano Letters*, 6(4):583–586.

Zhang, P. C., Keleshian, A. M., and Sachs, F. (2001). Voltage-induced membrane movement. *Nature*, 413:428–432.

Zhang, X. C., Myers, E. B., Sader, J. E., and Roukes, M. L. (2013). Nanomechanical torsional resonators for frequency-shift infrared thermal sensing. *Nano Letters*, 13(4):1528–1534.

CURRICULUM VITAE

Charles A. Lissandrello

24 Ransom Rd., Apt. 7 Brighton, MA 02135 USA
Phone: (516) 946-6304, E-mail: chanli44@bu.edu

Education

Boston University, College of Engineering Boston, MA
Ph.D., Mechanical Engineering *09/2009 – 05/2015*
Advisor: Prof. Kamil L. Ekinci
Dissertation: *Nanomechanical Measurements of Fluctuations in Biological, Turbulent, and Confined Flows*

Boston University, Boston, MA, USA *09/2009 – 01/2012*
M.S., Mechanical Engineering (GPA: 3.91/4.00)
Advisor: Prof. Kamil L. Ekinci

Boston University, Boston, MA, USA *09/2005 – 05/2009*
B.S., Mechanical Engineering (GPA: 3.67/4.00)
Dean's List: All Semesters

Awards, Fellowships & Honors

National Science Foundation Graduate Research Fellowship	*2009 – 2014*
Dean's Graduate Research Fellowship, Boston University	*2009 – 2010*
FIRST Robotics Engineering Scholar, Boston University	*2005 – 2009*
Summer Term Alumni Research Scholar, Boston University	*2006, 2008*

Research and Teaching Experience

Graduate Research Assistant Boston University
Nanometer Scale Engineering Laboratory *09/2009 – 05/2015*
Advisor: Prof. Kamil L. Ekinci

Graduate Teaching Fellow Boston University
Department of Mechanical Engineering *01/2015 – 05/2015*

Foundations of Aerodynamics (ME 421)

Undergraduate Research Assistant Boston University
Nanometer Scale Engineering Laboratory *05/2006 – 09/2009*
Advisor: Prof. Kamil L. Ekinci

Journal Publications

C. Lissandrello, K. L. Ekinci, and V. Yakhot, "Noisy Transition to Turbulence in Microchannels," Manuscript submitted for publication (2015).

C. Lissandrello, F. Inci, M. Francom, M. R. Paul, U. Demirci, and K. L. Ekinci, "Nanomechanical Motion of *Escherichia coli* Adhered to a Surface," *Applied Physics Letters* **105**, 113701 (2014).

T. Kouh, U. Kemiktarak, O. Basarir, C. Lissandrello, and K. L. Ekinci , "Measuring Gaussian Noise using a Lock-In Amplifier," *American Journal of Physics* **82**, 778 (2014).

C. Lissandrello, V. Yakhot, and K. L. Ekinci, "Crossover from Hydrodynamics to the Kinetic Regime in Confined Nanoflows," *Physical Review Letters* **108**, 084501 (2012).

Conference Presentations

C. Lissandrello, F. Inci, U. Demirci, and K. L. Ekinci, "Nanomechanical Measurement of the Frequency Spectrum of Bacterial Fluctuations on a Surface," **Boston University Scholars' Day**, Boston, MA, Apr. 15, 2104 *(Poster)*.

C. Lissandrello and K. L. Ekinci, "Calibration of the Modal Parameters of a Microcantilever from Gas Dissipation," **66th Annual Meeting of the APS Division of Fluid Dynamics**, Pittsburgh, PA, Nov. 24 – 26, 2013.

C. Lissandrello, V. Yakhot, and K. L. Ekinci, "Fluid-Induced Nanomechanical Fluctuations of an Elastic Membrane," **65th Annual Meeting of the APS Division of Fluid Dynamics**, San Diego, CA, Nov. 18 – 20, 2012.

C. Lissandrello, V. Yakhot, and K. L. Ekinci, "Crossover from the Hydrodynamic to the Kinetic Regime in Confined Nanoflows," **APS March Meeting 2012**, Boston, MA, Feb. 27 – Mar. 2, 2012.

C. Lissandrello, V. Yakhot, and K. L. Ekinci, “Confinement Effects in Oscillating Nanoscale Flows,” **64th Annual Meeting of the APS Division of Fluid Dynamics**, Baltimore, MD, Nov. 20 – 22, 2011.

C. Lissandrello and K. L. Ekinci, “Physical Science with Nanomechanical Resonators,” **Boston University School of Public Health, Global Health & Engineering Meetup**, Boston, MA, Nov. 18, 2011.

C. Lissandrello and K. L. Ekinci, “A Cantilever-Based Study of Oscillating Nanoscale Flows,” **8th International Workshop on Nanomechanical Sensing**, Dublin, Ireland, May 11 – 13, 2011.